# Development of Photocatalytic Titanium Dioxide Shell on Titanium Powder for Cold Gas Dynamic Spray

---

**ALEXANNA HAWKINS**

Thesis submitted to the University of Ottawa
in partial fulfillment of the requirements for the degree of

**MASTER OF APPLIED SCIENCE**

Faculty of Engineering
Department of Mechanical Engineering
University of Ottawa

Originally Submitted: October 22, 2025
Revised: January 29, 2026

# ABSTRACT

The objective of the thesis was to produce a titanium dioxide shell on spherical pure titanium powder that had heterojunctions of anatase and rutile nanostructures with photocatalytic properties for cold gas dynamic spray applications. This would be the first step in the global project of sprayable titanium dioxide coatings for self-sanitizing surfaces. A heterogeneous structure would provide the stability and closer band gap to the visible light spectrum from rutile and the high photocatalytic reactivity from anatase. The presence of heterojunctions could increase the photo-reactivity by promoting charge separations and promote reactions under visible light with a smaller band gap. Cold gas dynamic spray would provide the mechanism to consolidate this material without unwanted phase transformations from anatase to rutile at higher temperatures. As the temperatures are below the metals melting point, a combination of ceramic titanium dioxide and ductile titanium would assist in successful deposition via cold gas dynamic spray.

Preliminary experiments were completed on readily available titanium plates to observe potential growths and compare the results to reference literature. The final powder production procedure included a hydrogen peroxide, melamine, and nitric acid chemical bath at 80 ℃ for twelve hours followed by calcination for one hour at 450 ℃. This experimental procedure yielded the growth of spiked nanorods with nanoflower aggregates seen through scanning electron imaging. X-ray diffraction verified the presence of anatase and rutile structures, and Raman spectroscopy verified the titanium dioxide shell was predominantly anatase near the titanium core, with anatase and rutile heterojunctions at the outer part of the titanium dioxide shell. Photocatalytic testing was completed by subjecting the titanium dioxide in deionized water to methylene blue, an organic dye commonly used as an indicator for evaluating photocatalytic performance, and an ultraviolet light source to produce reactive oxidizing species that accelerate the decomposition of methylene blue. The experimental powders photocatalytic reactivity was compared to that of two commercial powders, Altair and Neoxid. Methylene blue adsorption and subsequent decomposition by the powders was characterized through microplate light absorbancy readings. The experimentally produced powder performed comparable to the commercial powders, verifying its photocatalytic properties under ultraviolet light. Dynamic vapour sorption was completed on all three powders to characterize the surface areas and adsorption properties of the experimental and commercial powders to provide

further understanding of photocatalytic results. The commercial powders had different particle size, specific surface areas, and dynamics of adsorption when compared to the experimental powder, which would impact photocatalytic behaviour.

Although the experimental powder did not have superior photocatalytic reactivity to those of the commercial powders, the motivation is the presence of a ductile titanium core would plastically deform below its melting temperature to promote deposition efficiency in cold gas dynamic spray applications and produce a successful photocatalytic titanium dioxide coating. Solely ceramic titanium dioxide powders, like Altair and Neoxid, experience brittle impingement and poor deposition from lack of plastic deformation and metallurgical bonding. Overall, successful growth of heterogeneous titanium dioxide shells was grown on titanium powder that possessed photocatalytic properties comparable to commercially available powders to be applied in cold gas dynamic spray applications. The work completed created a strong foundation for project development and expansion.

# ACKNOWLEDGEMENTS

I would like to start by extending my gratitude to my thesis supervisor, Dr. Bertrand Jodoin, for his support, patience, and providing the opportunity to work in some uncharted territory for the University of Ottawa Cold Spray Lab. I would also like to thank Dr. Deliang (Leon) Guo for being my mentor throughout countless experiments, methodology discussions and adjustments, and long hours in the lab. To Dr. Daniel MacDonald for his guidance, expertise, and support to the finish line.

Thank you to those in the University of Ottawa Cold Spray Lab for creating a lovely community to be a part of and Paul in the machine shop for discussions of machining processes and sample preparation. A big thank you to all the individuals and teams that shared their knowledge and resources; Dr. Jin-Ming Wu of the Zhejiang University for his knowledge in developing titanium dioxide, Dr. Fabio Variola and Alexander Steeves for Raman spectroscopy, Dr. Marianne Fenech for permitting me to use her lab space for photocatalytic testing, Dr. Jean-Philippe St-Pierre and Siestke Barnes for plate reading, Dr. Jeffrey Ovens for x-ray diffraction, and Zygmunt Jakubek at the National Research Council for dynamic vapour sorption. This was an endeavour with various components, thank you for the pieces to complete my puzzle.

Thank you to my family and friends for their encouragement throughout this long journey, it was not without its tumultuous moments these past few years. You have helped me overcome what at times I doubted I could. Merci beaucoup Olivier pour ton encouragement. Je n'aurais pas pu y arriver sans toi (et Biscuit), bisous.

Lastly, to myself, for being tenacious. I finished it.

# TABLE OF CONTENTS

# LIST OF TABLES

# LIST OF FIGURES

# ACRONYMS

| | |
|---|---|
| BET | Brunauer-Emmett-Teller |
| BSE | Back Scattered Electron |
| CB | Conduction Band |
| CGDS | Cold Gas Dynamic Spray |
| CP | Commercially Pure |
| DR | Distal Region |
| DVS | Dynamic Vapour Sorption |
| LHT | Laboratory High Temperature |
| MB | Methylene Blue |
| NRC | National Research Council |
| PR | Proximal Region |
| RH | Relative Humidity |
| ROS | Reactive Oxidizing Species |
| SEM | Scanning Electron Microscope |
| SSA | Specific Surface Area |
| TEM | Transmission Scanning Electron |
| UV | Ultraviolet |
| VB | Valence Band |
| XRD | X-ray Diffraction |

# CHEMISTRY

| | |
|---|---|
| $[Ti-O]^-$ | Titanium oxide anion |
| $C_3N_3(NH_2)_3$ | Melamine |
| $H_2$ | Hydrogen |
| $H_2O_2$ | Hydrogen peroxide |
| $H_2O$ | Water |
| $H_3O^+$ | Hydronium ion |
| $H^+_{aq}$ | Hydrated hydrogen ion |
| $HNO_3$ | Nitric acid |
| $HTiO_3^- nH_2O$ | Hydrated titanate ion |
| N | Nitrogen |
| $O_2$ | Oxygen |
| $O_2^-$ | Oxygen radical |
| $OH^-$ | Hydroxyl ion |
| $Ti(OH)_4$ | Titanium tetra oxide |
| $TiO_2$ | Titanium dioxide |
| $TiO_2 nH_2O$ | Hydrated titanium |
| $\cdot OH$ | Hydroxyl radical |
| $\cdot OOH$ | Hydroperoxyl radical |
| HMT | Hexamethylenetetramine |
| Ti | Titanium |
| $Ti-OH$ | Titanium hydroxide |

# NOMENCLATURE

| | |
|---|---|
| A | Absorbance |
| $E_g$ | Band gap |
| $S_{BET}$ | Brunauer-Emmett-Teller (BET) specific surface area |
| d | Distance between crystalline lattice planes |
| e | Electron |
| $I_0$ | Incident light intensity |
| k | Kinetic constant |
| $T_{oct}$ | Octane sorption temperature |
| OD | Optical Density |
| P | Partial vapour pressure |
| hν | Photon energy |
| n | Positive integer |
| $M_{ref}$ | Reference mass |
| $P_0$ | Saturation vapour pressure |
| I | Transmitted light intensity |
| V | Voltage |

# 1 INTRODUCTION

## 1.1 Background

Titanium dioxide ($TiO_2$) is widely used in industrial applications, including wastewater treatments, air purifying, and outdoor and glass coatings, due to its photocatalytic properties, chemical resistance, stability, and cost efficiency. It holds high appeal as a coating material because of self-cleaning properties when exposed to organic pollutants via accelerated decomposition [1]–[15]. As an effect of the coronavirus pandemic, research into efficient photocatalytic $TiO_2$ coatings have become of great interest in the field of self-disinfecting surfaces [13], [15]–[24]. $TiO_2$ is a pre-existing pigment additive to white paint to increase its brightness and opacity, but further research is being completed to utilize its photocatalytic reactivity as a disinfectant within a painted wall [10], [23]–[32]. $TiO_2$ coatings are also promising in dental and medical metallic implants and prosthesis as $TiO_2$ is antimicrobial and biocompatible [33]–[36]. Commercial disinfectants that require persons for application cannot maintain constant sanitization of surfaces, whereas self-cleaning surfaces hold the potential for assisting in limiting infection in both public, such as medical and high traffic areas, and private environments, such as in the home or body.

In crystallography, when a solid chemical compound contains more than one crystalline form it is referred to as polymorphism. $TiO_2$ has three primary natural polymorphic structures: brookite, anatase, and rutile (Figure 1.1). Brookite possesses a rhombohedral crystal structure and is difficult to obtain in its pure phase, making it unstable and difficult to work within laboratory settings [9], [37]–[41]. Anatase and rutile are primarily used because they possess tetragonal crystal structures that provide stability necessary for easy and safe industrial applications.

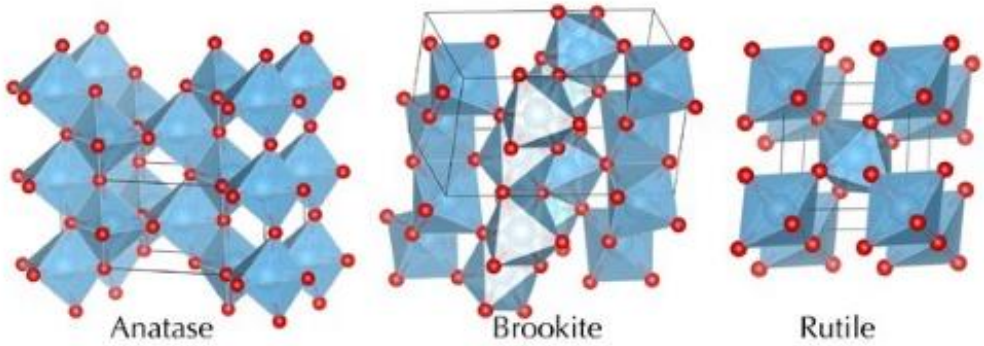


**Figure 1.1: Anatase, brookite, and rutile crystal structures** [23]**.**

Rutile is the most thermodynamically stable $TiO_2$ polymorph and, with a band gap of about 3.0 eV, absorbs photons at slightly longer wavelengths than anatase, closer to the visible region. In pure form, however, rutile generally exhibits lower photocatalytic activity due to faster charge recombination, so strong surface redox reactions are more effectively achieved when rutile is combined with anatase in a heterojunction structure. Rutile is used for applications that prioritize material stability, durability, and opacity. It reflects more light than other forms of $TiO_2$ because of its high refractive index. Its opacity makes it the choice for paint pigments to lower necessary coatings and its refractive index preserves colour under sun exposure, as well as offering other sun protection in additional applications such as sunscreens and other optical coatings like lenses. Its high temperature tolerance and semi-conductivity also make it the selection in electronics for metal dielectric barriers, a layer of metal insulator separating conductive metals [23], [24], [42], [43]. Anatase is metastable and more reactive under ultraviolet (UV) light than rutile due to its more open crystal structure, slower charge recombination, and larger band gap (3.2 eV) that allows for strong UV light absorption. Anatase is primarily seen in applications for its photocatalytic properties like air and water purifying, self-cleaning surfaces, and antimicrobial coatings. Anatase is also generally cheaper than rutile, making it a cost-effective option [9], [15], [23], [24], [32], [40], [41], [43]–[46].

$TiO_2$ begins to undergo an irreversible phase change from anatase to rutile when temperatures surpass 610 to 915 ℃ because anatases instability causes its particles to adhere and become larger particles which become the interfaces for rutile phase nucleation. The phase change temperature threshold varies due to initial $TiO_2$ preparation conditions [38], [40], [47], [48]. Calcination is a thermal treatment applied to materials to alter their composite properties and improve thermal stability, often by increasing crystallinity and inducing phase changes. While it can help maintain certain morphological features, it may also cause particle growth or densification depending on temperature and duration. For anatase, calcination at around 450 ℃ can strengthen weak amorphous anatase structures by decomposing hydrogen titanate structures and improve crystallinity [38], [40], [49]–[56].

Studies have shown higher reactivity in anatase-rutile mixtures because of the presence of heterogeneous interphase junctions. As a result of the differences in lattice structure,

heterojunctions create localized disorder between anatase and rutile that contain different energy band structures. The combination of both structures enhance the redox reaction properties, decrease bulk recombination, and lead to an increase in carrier separation efficiency at the interface, thus allowing for overall higher reactivity in the junction than either single phase material [10], [11], [32], [39]–[41], [44], [57]–[62]. Research has also shown promise in heterojunction presence assisting in photocatalytic activity in the visible light range, utilizing rutile's higher response closer to the visible light range, and the higher reactivity of anatase. Historical methods of increasing $TiO_2$ reactivity under visible light require additives such as metal and non-metal doping or co-doping, coupling with a narrow band gap semiconductor, surface sensitizations, and depositing noble metals [40], [45], [56], [58], [60], [62]–[67].

This thesis work is the production of heterogenous photocatalytic $TiO_2$ powder, as the first step in the global project of the development of heterogenous photocatalytic coatings for self-sanitizing surfaces on pre-existing structures. This holds appeal in public spaces like transit, hospitals, playgrounds, and other high traffic patron areas that are prone to the transfer and spread of germs and bacteria. Utilizing and enhancing the natural properties of $TiO_2$ can eventually assist in facilitating safe and clean public environments. Reactive coatings under visible light would be applicable in areas with artificial indoor lighting and areas that receive bright natural light. These surfaces would not need designated exposure but would be able to self-sanitize consistently under visible light. UV reactive $TiO_2$ coatings are attractive in the medical field and other controlled environments, where UV exposure can be integrated into sanitizing procedures to enhance surface disinfection within monitored settings. Additionally, successful development of self-sanitizing surfaces through natural enhancement reduces the use of artificial cleaning agents which can be potentially harmful to both patrons and the environment.

There are currently many application techniques for $TiO_2$ coatings that include physical/chemical vapour deposition and sol-gel techniques [32], [41], [68]. Thermal spray processes have been used due to their fast deposition rates, flexibility on powder and substrate selection, and capability of coating large surfaces. A large challenge in thermal spray deposition of $TiO_2$ coatings is maintaining the nano-structured heterojunctions because high process temperatures lead to grain growth and anatase-to-rutile phase transitions [32], [41], [68].

Cold gas dynamic spray (CGDS) operates within a temperature range that preserves powder mechanical properties and morphology, preventing anatase-to-rutile phase transformations. $TiO_2$, as a ceramic, exhibits low deposition efficiency in CGDS because it cannot convert kinetic energy into plastic deformation, resulting in brittle impingement, poor adhesion, and uneven coatings. In contrast, titanium (Ti) powder is highly sprayable by CGDS due to its ductility below the melting point, enabling the necessary plastic deformation and strain for successful deposition. The objective of this work is to produce a $TiO_2$ shell on commercially pure titanium (CP-Ti) powder. Through heat treatment chemical bath and calcination anatase-rutile nanostructures can be grown and on CP-Ti powder. The presence of nanostructures increases the specific surface area (SSA) and heterojunctions create lattice disorder, which both encourage charge separation and subsequent photocatalytic activity when $TiO_2$ is exposed to a UV light source. Additionally, the development of highly reactive heterogeneous $TiO_2$ with a narrower band gap could lead to reactivity in the visible light field [60]. The combination of having good deposition efficiency from the ductile CP-Ti powder and maintaining the photocatalytic heterojunctions in $TiO_2$ nanostructure is the initiative behind producing powder using this methodology [69].

## 1.2 Research Objectives

The motivation of the research presented in the thesis is a project undertaken by the University of Ottawa Cold Spray Research Laboratory surrounding the production of a $TiO_2$ shell on a CP-Ti spherical powder as a critical first step to the global project of self-sanitizing coatings. The objective is to successfully produce anatase-rutile heterojunctions within the $TiO_2$ shell that possess comparable photocatalytic properties as commercially available $TiO_2$ powders. The goal of producing this powder is to allow for the deposition by CGDS like CP-Ti while maintaining the reactivity of $TiO_2$. The following steps were completed to fulfill this objective:

1. Preliminary development of methodology to grow heterogenous $TiO_2$ shell on CP-Ti plates. Analysis of $TiO_2$ growth through Scanning Electron Microscope (SEM) characterization.
2. Development of powder methodology to grow heterogenous $TiO_2$ shell on CP-Ti powder. Analysis of $TiO_2$ growth through Scanning Electron Microscope (SEM) characterization.

3. Verification of heterogenous nanostructures on powder through X-Ray Diffraction (XRD) and Raman spectroscopy.
4. Development of photocatalytic testing methodology and photocatalytic characterization of experimental and two commercial powders, Altair and Neoxid. Characterization of experimental and commercial powders through dynamic vapour sorption (DVS) to connect surface features to photocatalytic properties.

## 1.3 Thesis Outline

The thesis is composed of seven chapters. The chapters and their contents are outlined in this section.

Chapter 1 includes an introduction of background information, motivations, and the objectives of the research.

Chapter 2 is composed of the literature review, containing relevant information on the topics covered within the research. It begins by covering $TiO_2$ photocatalytic properties, previous studies of $TiO_2$ growth on Ti, and cold gas dynamic spray application.

Chapter 3 explains the overviews of equipment, their theories and processes, used to analyze and verify results.

Chapter 4 presents the preliminary research detailing the evolution of the chemical bath procedure used to grow the $TiO_2$ shell on Ti plates and the SEM results.

Chapter 5.1 explains the methodologies of the experimental procedures to develop CP-Ti powder with $TiO_2$ shells. Chapter 5.2 contains the experimental procedure and SEM characterization observations. Chapter 5.3 and 5.4 outline how the growth of $TiO_2$ shells and the desired heterojunctions were verified through XRD and Raman spectroscopy. Chapter 5.5 includes the procedures and results of photocatalytic testing, including the comparison with commercial powders. Chapter 5.6 includes the results of DVS. Surface area properties are discussed and the potential relations to photocatalytic activity.

Chapter 6, the conclusion of the thesis, summarizes the experimental procedures and results.

Chapter 7 discusses future work, as there are various avenues that this research can be altered and/or expanded on. This chapter was included as the research is novel for both the University of Ottawa and the University of Ottawa Cold Spray Research Laboratory. This final chapter is followed by the references.

# 2 LITERATURE REVIEW

This section outlines the foundational knowledge of $TiO_2$ necessary to achieve the experimental objectives. This includes the chemistry of the photocatalytic reaction, experimental procedures of developing $TiO_2$ onto Ti, and the CGDS process and parameters, along with literature of $TiO_2$ deposition via CGDS.

## 2.1 Photocatalytic Mechanism of Titanium Dioxide

The term 'photocatalysis' originates from the words light and catalysis and can be defined as a chemical reaction that is induced by the photo-absorption on a semiconductor. The semiconductor is referred to as the photocatalyst, and the reaction happens along the surface which remains unchanged during and after the reaction [70]. A photocatalyst utilizes the energy brought by light and can promote reactions that are unfavourable under thermodynamic laws, such as splitting water into hydrogen and oxygen [70], [71]. $TiO_2$ is a heterogenous photocatalyst because the semiconductor (solid) and reactant (fluid) are in different phases [72]–[74].

Photocatalysis occurs in the following stages [70]–[72]:

1. Diffusion within a fluid phase to the surface of the photocatalyst.
2. Adsorption of reactants along the surface of the photocatalyst.
3. Redox reaction between the absorbed reactants and photocatalyst.
4. Desorption of the products from the surface of the photocatalyst.

The above process can occur in liquid or gas phases and in stage three the chemical reaction allows for the degradation of pollutants. A redox reaction occurs when a chemical reaction facilitates the exchange of electrons between atoms or molecules. Gaining electrons is reduction, and giving electrons is oxidation. For a redox reaction to occur, there needs to be redox potential differences between the chemical species [11], [71], [72], [74].

The energy difference between the valence band (VB) and conduction band (CB) is referred to as the band gap ($E_g$) and measured in electron-volts (eV). Materials are classified into three categories based on their $E_g$ [39], [41], [71], [72], [74]–[76]:

- Metal / Conductor

- Possess no $E_g$ because the VB and CB overlap.
- Are highly conductive as electrons are continuously available to move.

- Semiconductor
  - Possess small $E_g$.
  - Are conductive as electrons can jump from the VB to CB.
- Insulator
  - Possess a large $E_g$.
  - Are low in conductivity as electrons are unable to jump from the VB to CB.

The photocatalytic mechanism of $TiO_2$ works by the absorption of a photon with enough energy ($h\nu$) to produce movement of electrons from the VB to the CB in the lattice structure, forming conduction band electrons ($e^-$) and valence band holes ($h^+$), electron-hole pairs, upon UV photoexcitation (Equation 2.1) [9]–[14], [41], [71], [72], [74], [75], [77], [78].

$$TiO_2 + h\nu \rightarrow e^-(TiO_2) + h^+(TiO_2) \qquad \textbf{2.1}$$

$TiO_2$ has a band gap of 3.0 – 3.2 eV depending on its nanostructure composition. Both $e^-$ and $h^+$ contribute to electrical conductivity and although holes may give the appearance of moving, they are freed space, and a neighbouring electron will move to fill the space which can give the illusion of positively charged movement (Figure 2.1) [75].

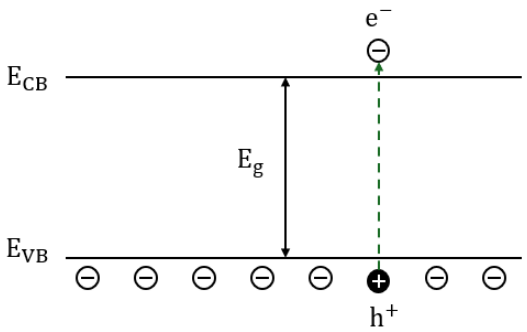


**Figure 2.1: Photogenerated electron-hole pair.**

$TiO_2$ is a semiconductor ceramic that when irradiated with an energy source above 3.0 - 3.2 eV, like ultraviolet light, produces electron-hole pairs that react with light and oxygen. The photogenerated electron-hole pair will either produce a non-productive reaction, like charge recombination, or successfully migrate to the $TiO_2$ surface. At the surface, the pair will react with

oxygen ($O_2$) and water ($H_2O$) in the environment to form reactive oxidizing species (ROS). [10], [11], [13], [14], [71], [74], [77]–[82].

ROS are naturally occurring oxidizing agents that when exposed to a catalyst can accelerate the breakdown of organic matter through increased redox reactions. Increased redox reactions on biological systems lead to oxidative stress by producing more ROS than the organic matter can combat. The application of increasing ROS on systems to combat pollutants, like bacteria and viruses, could be used as a form of natural sanitization [83]–[85].

Utilizing the $TiO_2$ surface as the photocatalyst and subjecting it to UV light, $H_2O$ reacts with $h^+$ to produce ROS called hydroxyl radicals ($\cdot OH$) (Equation 2.2). This reaction also produces hydrogen molecules ($H^+_{aq}$) [11].

$$\mathbf{h^+ + H_2O \rightarrow \cdot OH + H^+_{aq}} \qquad \mathbf{2.2}$$

Simultaneously, $O_2$ reacts with $e^-$ at the $TiO_2$ surface to produce further ROS as oxygen radicals / superoxide anions ($O_2^-$) (Equation 2.3) [11].

$$\mathbf{O_2 + e^- \rightarrow O_2^-} \qquad \mathbf{2.3}$$

Figure 2.2 shows the photocatalytic reaction process that results in successful movement of the electron-hole pair to the surface of the $TiO_2$ and produce ROS which then react with organic compounds and produce organic pollutant end products [11].

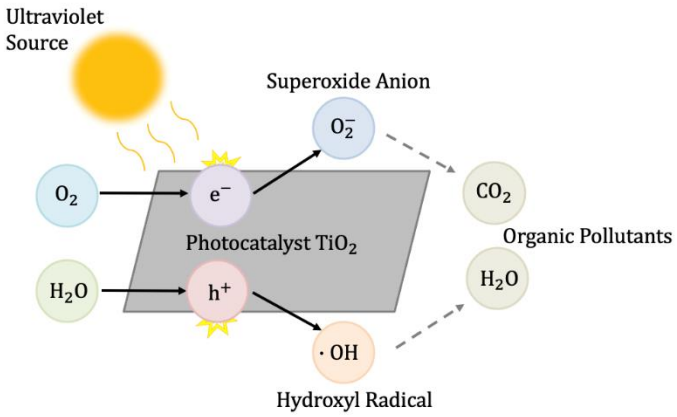


**Figure 2.2: Titanium dioxide photocatalytic mechanism.**

The production of $O_2^-$ and $\cdot OH$ generate additional ROS by producing hydrogen peroxide ($H_2O_2$) (Equation 2.4 and 2.5) ultimately leading to more hydroxyl radicals ($\cdot OH$) and hydroxyl ions ($OH^-$) (Equation 2.6). Additionally, $O_2^-$ can react with $H_{aq}^+$ and produce hydroperoxyl radicals ($\cdot OOH$) ( Equation 2.7) [10], [11], [13], [14], [71], [74], [77], [79]–[81], [86].

$$\cdot OH + \cdot OH \rightarrow H_2O_2 \quad \textbf{2.4}$$

$$\mathbf{2O_2^- + 2H_{aq}^+ \rightarrow H_2O_2 + O_2} \quad \textbf{2.5}$$

$$O_2^- + H_2O_2 \rightarrow \cdot OH + OH^- + O_2 \quad \textbf{2.6}$$

$$O_2^- + H_{aq}^+ \rightarrow \cdot OOH \quad \textbf{2.7}$$

ROS can be broken down into two categories of radical (highly reactive) or non-radical (less reactive). Radical ROS are free radicals with unpaired electrons and operate by one-electron oxidation resulting in lower activation barriers and quick electron exchange. A result of having higher redox potential is stronger oxidation and diffusion rates when in contact with organic matter. $O_2^-$, $\cdot OH$, and $\cdot OOH$ are all highly reactive radical ROS and are the predominant contributors to the accelerated decomposition of organic matter. Figure 2.3 shows the chemical structures of the radical ROS where $\cdot$ denotes unpaired electrons [79].

**Figure 2.3: Chemical structures of oxygen, hydroxyl, and hydroperoxyl radicals.**

$H_2O_2$ and $OH^-$ are non-radical ROS because they do not possess unpaired electrons, as seen in Figure 2.4 and are stable molecules that operate by two-electron oxidation. Non-radical ROS do not strongly contribute to accelerated breakdown of organic matter because they lack unpaired electrons for strong redox reactions. They are still derived from $O_2$ and $H_2O$ and their cellular processes can result in oxidative stress, which can contribute to minor organic matter breakdown. [10], [11], [14], [77].

**Figure 2.4: Chemical structures of hydrogen peroxide and hydroxyl ions.**

ROS continue to create redox reactions while exposed to a catalyst through the continued transfer of electrons. This is seen in the cyclical production of $H_2O_2$ and $\cdot OH$ in Equations 2.4 and 2.6. An additional example would be the production of $OH^-$ could lead to additional $\cdot OH$ by interacting with the VB band energy level $h^+$charge carriers (Equation 2.8) [10], [11], [14], [77].

$$h^+ + OH^- \rightarrow \cdot OH \qquad \textbf{2.8}$$

$TiO_2$ photocatalytic reactivity can be measured by creating an aqueous solution with an organic dye, adding $TiO_2$ and subjecting it to a UV light source. The organic dyes decomposition is accelerated by ROS and reactivity is quantified by measuring the light absorbance of the aqueous solution with the dye over time. Organic dyes used include methylene blue (MB) and rhodamine B [44], [70], [78], [87]–[90].

## 2.2 Titanium Dioxide Development on Titanium

Studies have shown successful $TiO_2$ growth on Ti plates using $H_2O_2$ [78], [91]–[100]. Proposed explanations for the chemical reactions are attributed to the oxidizing properties of $H_2O_2$ which react with Ti to form $TiO_2$ (Equation 2.9). At temperatures around 80 ℃, the presence of hot water and $H_2O_2$ can hydrolyze $TiO_2$ resulting in titanium tetra hydroxide ($Ti(OH)_4$) (Equation 2.10 and 2.11) and hydrated titanium ($TiO_2nH_2O$, where *n* is a positive integer) (Equation 2.12). Hydrolyzed and hydrated titanium generate a slightly negatively charged surface (Equation 2.13 and 2.14) which contribute to the formation of surface nanostructures, like anatase and rutile [91], [94].

$$Ti + H_2O_2 \rightarrow TiO_2 + H_2 \qquad \textbf{2.9}$$

$$2H_2O_2 \rightarrow 2H_2O + O_2 \qquad \textbf{2.10}$$

$$TiO_2 + 2H_2O \rightarrow Ti(OH)_4 \qquad \textbf{2.11}$$

$$TiO_2 + nH_2O \rightarrow TiO_2nH_2O \quad \textbf{2.12}$$

$$(Ti - OH) + H_2O \rightarrow [Ti - O]^- + H_3O^+ \quad \textbf{2.13}$$

$$TiO_2nH_2O + OH^- \rightarrow HTiO_3^-nH_2O \quad \textbf{2.14}$$

Sisman et al. applied Ti films (100 nm and 1 μm) to alumina by sputtering and soaked samples in diluted $H_2O_2$ (15 and 2 weight percentage (wt %)) at 80 ℃ for 20 hours. The samples were annealed at 450 ℃ for 4 hours. SEM images showed micro cracks in samples with thicker films and higher $H_2O_2$ concentrations (Figure 2.5). XRD peaks indicated rutile nanostructures [91]. A similar study by Sun et al. used Ti plates soaked in 30 wt % $H_2O_2$ at 80 ℃ for 24 hours, then water at 80 ℃ for 72 hours. SEM images showed micro cracks and XRD confirmed the presence of crystalline anatase nanostructures [94].

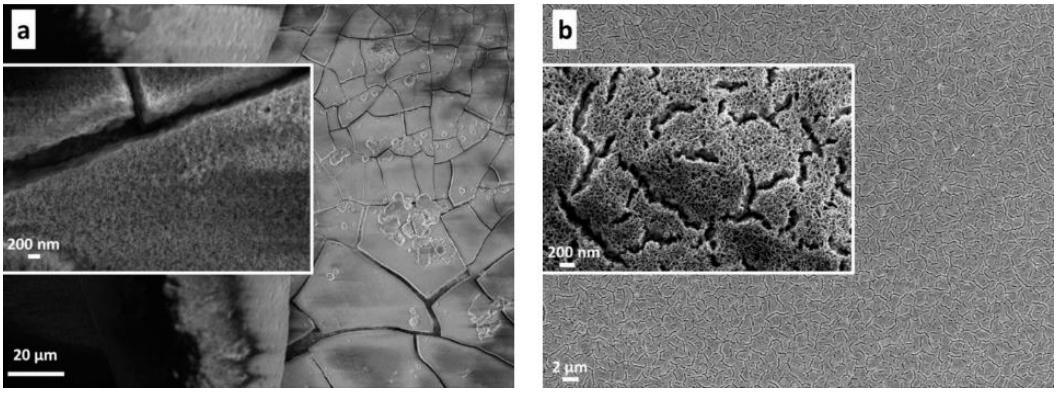


**Figure 2.5**: **SEM images of $TiO_2$ surface (a) 1 μm Ti film in 15 % $H_2O_2$ and (b) 100 nm Ti film in 2 % $H_2O_2$** [91].

Wu et al. subjected Ti plates to 30 wt % $H_2O_2$ at 80 ℃ for 5 hours and then distilled water at 80 ℃ for 72 hours. XRD patterns confirmed poorly crystallized anatase nanostructures in the plates prior to the hot water soak and well crystallized anatase afterwards. The samples photodegraded rhodamine B directly to end products [78]. They also took Ti plates in 30 wt % $H_2O_2$ at 80 ℃ for 72 hours and placed in an oven at 450 ℃ for 1 hour noted the thermal treatment kept the ordered nanostructure and improved crystallinity [98]. Another experiment they completed placed ultrasonically rinsed Ti plates into 15 wt % $H_2O_2$ at 80 ℃ for 1 hour, followed by calcination at 300 ℃ for 1 hour. Successful growth of anatase microstructures was verified through XRD [93].

Calcination is the process of heating a material at a regulated temperature in a controlled environment to induce morphological and functional changes to the material [49], [54], [101]–[103]. Calcination is a post-treatment to chemical baths where $TiO_2$ is subjected to higher temperatures to induce crystallinity, control phases, alter surface area, and remove impurities. Experiments have noted that calcination temperatures ranging from 300 to 700 ℃ for durations within 1 to 4 hours have increased the photocatalytic properties of $TiO_2$ due to heterojunctions with a high anatase to rutile ratio that produces smaller particle sizes, faster charge separations, higher crystallinity, and narrowing of the band gap. As calcination temperatures increase above 300 ℃ crystallite size, crystallinity, and particle size also increase as amorphous or weaker crystalline $TiO_2$ transitions to anatase. Anatase's larger band gap, oxygen vacancies, and open crystal structure provides superior oxidizing capabilities, charge separation, and active sites for ROS generation to rutile. Anatase begins transitioning to thermally stable rutile around temperatures exceeding 600 ℃ as anatase's instability causes particles to stick together and create interfaces for rutile phase nucleation. Temperatures exceeding 700 ℃ demonstrate lower photocatalytic reactivity from high rutile presence creating larger crystallite sizes, and smaller SSA and pore volume from aggregation and agglomeration resulting in decreased available surface area for reaction sites and increased charge recombination [6], [10], [11], [40], [48], [62], [104]–[109]. Phromma et al. noted that at calcination temperatures of 800 ℃ the $TiO_2$ particle size had exponentially increased compared to lower calcination temperatures due to large rutile crystallites and particle agglomeration. The band gap decreased as the temperature and rutile structures increased, but the photocatalytic activity overall decreased as anatase decreased. The strongest photocatalytic activity was seen in powder with the highest anatase to rutile ratio that possessed the largest kinetic constant (k) [106]. Li et al. stated that calcination of nitrogen doped $TiO_2$ at 450 ℃ for 2 hours produced heterogeneous powder with superior photocatalytic behaviour in MB degradation than powders calcinated at other temperatures and longer durations [107].

Successful charge separation of photogenerated electron-hole pairs to the surface of $TiO_2$ for ROS generation is required for photocatalytic reactivity. Higher SSA provides more pathways for charge separation and active ROS sites along $TiO_2$ allowing more organic pollutants to be adsorbed along the surface and broken down under photoexcitation. Increased porosity in the structural framework also increases SSA and can reduce the distances required for the electron-hole pairs to

travel to the surface for ROS generation [11], [40], [56], [58], [109]–[111]. Qin et al. remarked that decreased SSA with decreased $TiO_2$ crystallinity and increased amorphous components exhibited higher rates of charge recombination and lower photocatalytic activity [111]. Zhao et al. grew nanowires grown on $TiO_2$ and concluded the powder with the highest SSA, pore volume, and highest k exhibited the highest pollutant degradation [56]. Zhu et al. found that tin doping $TiO_2$ increased its SSA, decreased charge recombination, and improved visible-light adsorption [61]. Grover et al. grew elongated porous $TiO_2$ nanowires seen through SEM and transmission electron scanning microscope (TEM) (Figure 2.6) that exhibited high SSA with improved charge separation and accelerated organic pollutant decomposition [58].

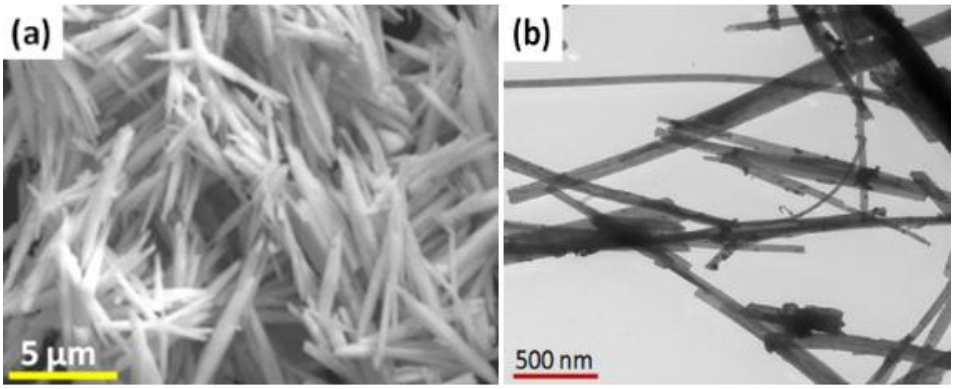


**Figure 2.6: Grover et al. a) SEM and b) TEM images of $TiO_2$ nanowires** [58]**.**

Nanostructures like nanowires, nanorods, nanotubes, nanoflowers, and nanosheets can increase SSA that promote fast charge transfer rates and low bulk recombination, promoting photocatalytic activity. Single one-dimensional forms of $TiO_2$ have higher rates of bulk recombination, which result in less electron-hole pairs reaching the surface to form ROS. Heterostructure junctions push the separation of the electron-hole pairs because of the anatase-rutile dislocations of the CB and VB positions in the lattice structure, this suppresses bulk recombination and favours the migration of charges to the surface for redox reactions [10], [11], [40], [41], [56], [58]–[61], [99], [112].

Wu et al. placed Ti plates in 50 mL 30 wt % $H_2O_2$ at 80 ℃ for 72 hours. It was rinsed with deionized water and air dried. Additionally, 20, 50, and 100 mg of CP-Ti powder was placed into 100 mL 30 wt % $H_2O_2$ at 80 ℃ for 72 hours. Both the plates and powder had anatase and rutile nanostructures verified through SEM (Figure 2.7). Further experiments were done with chemical additives to the $H_2O_2$ and concluded the additions of fluorine ions and sulfate ions helped anatase formations [92].

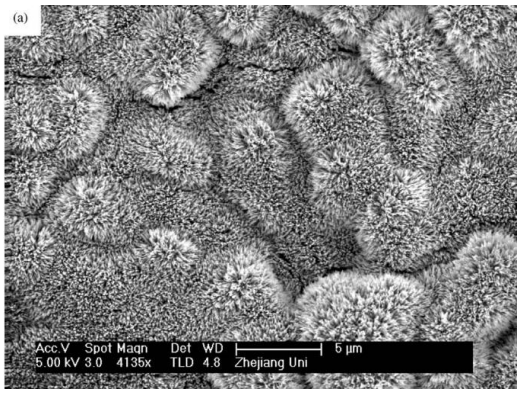


**Figure 2.7: Wu et al. SEM image of Ti plate after soaking in 30 wt % $H_2O_2$ at 80 ℃ for 72 hours** [92].

Introducing additives can alter the pH of $H_2O_2$ baths and subsequently alter nanostructures shape and compositions of rutile and anatase. Wu et al. added nitric acid ($HNO_3$) and hexamethylenetetramine (HMT) to $H_2O_2$ noted that the rise in ammonia from HMT correlated to decreasing acidity and the formation of anatase nanoflowers, and that increasing $HNO_3$ increased acidity and promoted anatase and rutile growth [99]. Similar results were seen when adding $HNO_3$ and melamine ($C_3N_3(NH_2)_3$) as the hydrolysis of $C_3N_3(NH_2)_3$ releases ammonia resulting in a similar effect as HMT on the system. After calcination at 450 ℃ for 1 hour nanowire formations of rutile and anatase with nanoflower aggregates were seen by SEM (Figure 2.8) and presented photocatalytic properties comparable to commercial powder [100].

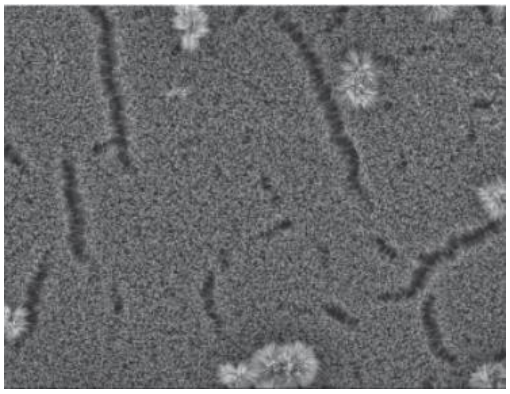

**Figure 2.8: Wu et al. SEM morphology of nanowire and nanoflower aggregates following $H_2O_2$, $HNO_3$ and $C_3N_3(NH_2)_3$ chemical bath and calcination at 450 ℃ for 1 hour [100]**.

The chemical bath pH also affects the rate of Ti oxidation and morphology synthesized $TiO_2$. Acidic conditions (pH ~1- 4) facilitate slower reactions and more uniform $TiO_2$ formations, with neutral conditions (pH ~6-7) providing safer handling environments and moderate reactions, and alkaline conditions (pH ~8-12) facilitating faster reactions that could

potentially produce nanostructures with more SSA. Rutile development is favoured in acidic conditions and anatase development is favoured in alkaline conditions. A chemical bath of a pH too high or too low can produce single phase nanostructures. [96], [99], [100], [113]–[116].

Qin et al. developed anatase-rutile heterojunctions on layered titanium carbide calcinated from 300 to 700 ℃ for one hour and evaluated for photocatalytic activity and hydrogen evolution under visible light. The most successful visible light photodegradation was achieved on the sample calcinated at 500 ℃. There was increased photocatalytic reactivity at the heterojunction interfaces from overlapping band structures that lead to increased charge separations. Strong electron transfer from rutile to anatase created a positive charge region at the rutile heterojunction interface, and a negative charge region at the anatase heterojunction interface. The result was an electric potential difference that increased separation charges and directed the movement of electrons [60]. Zhao et al. enhanced pre-established anatase-rutile heterojunctions in $TiO_2$ powder through a chemical bath of $H_2O_2$, $HNO_3$, and $C_3N_3(NH_2)_3$, and then calcinating at 450 ℃ for 1 hour for reactivity in visible light [56]. Etacheri et al. developed oxygen-rich anatase $TiO_2$ that reacted under visible light through in-situ generation of $O_2$ through thermal decomposition of peroxo-titania complexes [117]. Kusumawardani et al. observed that the ideal calcination temperature for nitrogen doped $TiO_2$to be 450 ℃, as temperatures above 450 ℃ decreased the nitrogen content. The presence of nitrogen narrowed the band gap and increased reactivity closer to the visible light range [118]. Other studies have introduced metals, non-metals, and semiconductors with narrow band gaps to assist in bringing the photo reactivity of $TiO_2$ into the visible region [40], [45], [58].

There is also the possibility to develop nanomaterials that have multi-structural dimensions to increase variation in surface ratios, surface defects, and exposed crystal facets to increase reactivity. Zero-dimensional structures include nanoparticles and quantum dots; one-dimensional includes nanotubes, nanowires, nanorods, and nanofibers; two-dimensional includes nanosheets; and three-dimensional includes spherical, porous framework. Varying crystal planes of the same polymorph have different levels of reactivity from exposure, surface ion bonding, and surface energy. For example, anatases crystal plane (001) tends to collect $h^+$ making is a better reductant and $e^-$ tend to flow to (101) having better oxidative activity [112]. Preferred growth is

predominantly seen along the stable crystal planes of (101) in anatase and (110) in rutile [11], [38], [47], [60], [61], [112].

Overall, literature has stated that $H_2O_2$ could successfully assist in developing both rutile and anatase nanostructures on Ti surfaces. Heterogeneous nanostructures promote photocatalytic activity by increasing charge transfers and inhibiting bulk recombination [10], [11], [40], [41], [56], [58], [59], [99], [112]. Adding additional chemicals has the potential to alter the nanostructural geometry by pH to promote anatase-rutile growth [92], [95]–[97], [99], [100]. Subsequent thermal treatments at high temperatures remove the amorphous structures and strengthen the crystallinity of the anatase formations [78], [91], [93], [94], [97]–[100].

## 2.3 Titanium Dioxide and Cold Gas Dynamic Spray

$TiO_2$ is wildly used in numerous industries, including the medical field, due to its mechanical stability, corrosion resistance, hard tissue compatibility, and biocompatibility. There is appeal in coatings for medical settings surfaces, surgical implants, and prosthesis [33]. There is also a large interest in environmental studies for purification, filtration, and sterilization [119]. Successful and effective deposition via CGDS holds appeal in industrial, environmental, and medical coatings [33], [119], [120].

CGDS is a technique that produces coatings from powder particle impingement upon a solid substrate at temperatures below the powder materials melting point. Particle sizes typically range from 5 to 100 μm and are accelerated to high speeds by injection into a supersonic stream of pressurized inert gas within a converging-diverging de Laval nozzle (Figure 2.9). The gas within the main line is heated up to 1000 ℃ to create high velocity flow that converts thermal energy to kinetic, resulting in gas velocities ranging from 300 to 1200 m/s. The powder particles having more inertia than the gas will gain speed as they travel but will move at velocities lower than the gas stream. The powder particles are fed from the powder feeder and pre-mixed with gas in a separate line before injecting into the main preheated gas line, either before or after the throat of the nozzle and deposition occurs when the particle impact velocity exceed the required critical velocity. Upon impact, the powder particles undergo inelastic collisions, resulting in plastic deformation, high strains, and heat, causing localized deformation and adherence to the substrate or previously deposited particles [15], [33], [69], [119]–[127].

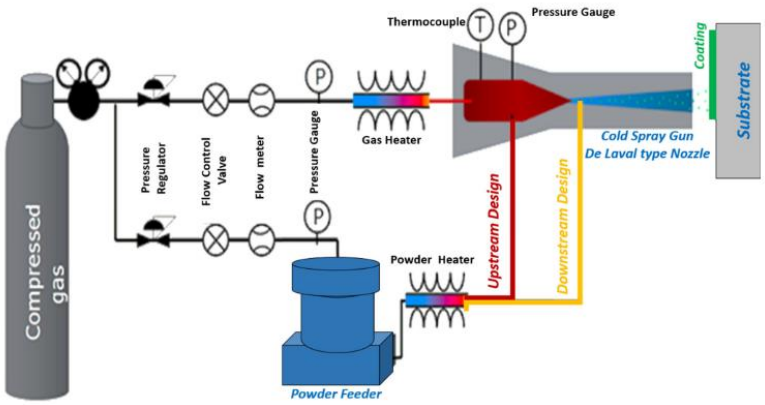


**Figure 2.9: Cold gas dynamic spray set up** [128].

Factors that contribute to a powders efficient deposition include the powder material properties (size, distribution, temperature, geometry, composition), process gas parameters (molecular weight, temperature, pressure), powder feed rate, nozzle parameters (dimensions, angle of injection, distance to substrate), substrate material properties (composition, hardness, surface preparation), and the particle impact velocity and temperature [122], [123], [125].

As the powder particles remain below their melting points in CGDS, the solid-state depositions have low degrees of residual stress and preserve the material properties. Original grain structures are maintained but can potentially deform upon impact. In multi-layered coatings the initial layers will show higher levels of deformation than the subsequent layers because of powder compaction [15], [69], [122], [123], [125], [126].

The yield strength of the powder and/or the substrate must be exceeded upon impact to promote the necessary kinetic energy transformation to plastic deformation. As a result, powder and substrate materials are typically selected that possess relatively high plasticity. High strength materials, like ceramics, are considered difficult to spray and struggle produce buildable layers as deposition is typically due to embedment into the substrate and less commonly particle-particle. Successful deposition of mixed ceramic and metal powders has been achieved where the ceramic powder did not plastically deform but was enveloped within the malleable metal powder upon the substrate. Introducing a ductile metal into the system provided the plastic deformation required for more efficient deposition [123].

The ceramic nature and properties of $TiO_2$ restricts adequate adhesion of the powder particles to a substrate because of the lack of plastic deformation. High spray temperatures can also lead to anatase to rutile phase transformations within the $TiO_2$ particles. The outcome of undesired phase changes would alter the photocatalytic properties of the powder and consequently the coated surface. CGDS operates at lower temperatures than other spray coating techniques, typically 300 ℃ to 1000 ℃, which allows for temperature variations that can prevent unwanted phase changes [15], [32], [33], [69], [119]–[121], [123], [129]–[131].

Successful CGDS deposition of $TiO_2$ with the intent of preserving its photocatalytic properties has been achieved on various substrates by applying high particle velocities to promote impingement through the native oxide layer on the substrate and particle-particle embedment, and with low process gas temperatures to avoid phase transformations. Although, deposited ceramic layers were thin which lack durability and scratch resistance for adequate coatings [15], [33], [69], [119]–[121], [129]–[131].

Herrmann-Geppert et al. deposited heterogeneous $TiO_2$ powder composed initially of 10% rutile and 90% anatase using nitrogen, helium, and argon at various temperatures up to 800 ℃ and then calcinated at 450 ℃ for 30 minutes. XRD on the deposited powders showed similar diffractograms of the nitrogen and argon samples to the original powder, whereas the helium sample exhibited a ratio of 30% rutile and 70% anatase. When tested for photoelectrochemical reactivity, the nitrogen sample demonstrated the highest reactivity, with the helium sample having the lowest. The deposited powders had good or only moderate adhesion to the substrate, which is a common result from the brittle nature of ceramic $TiO_2$ in CGDS [130]. Yamada et al. deposited anatase $TiO_2$ powder was at temperatures up to 400 ℃ by nitrogen and helium. XRD results of the deposited powder showed the presence of anatase structures in both samples. Although, the anatase peaks had shifted with the increased temperature potentially indicating the presence of residual stresses. Photocatalytic testing using a pollutant and simulated sunlight showed photocatalytic properties in both samples. It was noted that higher gas temperatures correlated to thicker coatings, which is commonly seen in metallic CGDS applications as higher temperature impacts the gas and particle velocity and softens the material to improve deposition [129]. Some studies noted that ductile substrates were able to plastically deform and allow shear instabilities upon ceramic $TiO_2$ powder

impact to promote deposition. One study selected substrates with materials of varying ductility's [131]. Another study annealed austenitic stainless steel, SUS 304, for a softer substrate that possessed a thicker oxide layer and demonstrated stronger adhesion [121].

CP-Ti powder demonstrates increased deposition efficiency in CGDS applications. The particle ductility promotes the successful conversion of kinetic energy to plastic deformation, strain, and heat upon impact to a substrate resulting in stronger, thicker, and more even coatings [132]–[135]. Deposition by CGDS also prevents a phase change from CP-Ti to $TiO_2$ as it readily reacts with $O_2$ at high temperatures which can negatively impacts its adhesion to the substrate [134], [136]. CP-Ti deposited well using both nitrogen and helium gas at temperatures ranging from 350 ℃ to 800 ℃ [124], [129]–[132], [135], [136]. A study also concluded that high particle velocities of 1140 m/s and preheating a Ti substrate to 400 ℃ resulted in higher substrate deformation and increased adhesion [124].

Developing a $TiO_2$ shell on CP-Ti could achieve a combination of desired photocatalytic properties from $TiO_2$ and efficient spray deposition from ductile CP-Ti as both powders have shown successful deposition following similar spray parameters. The low temperatures of CGDS would prevent element transformation from CP-Ti to $TiO_2$, which would affect the deposition efficiency, and anatase to rutile phase change in $TiO_2$, which would affect the photocatalytic properties. The ductility of the CP-Ti powders could provide the necessary inelastic collisions required for plastic deformation and strain to successfully deposit photocatalytic $TiO_2$ coatings.

# 3 ASPECTS OF EXPERIMENTATION

This section outlines the equipment used in the preparation, development, and analysis of $TiO_2$ growth on Ti plates and CP-Ti powder. The application of this equipment regarding the thesis are explained under Chapters 4 and 5 in the experimental procedures.

## 3.1 Titanium Dioxide Preparation

The following section contains the equipment used in sample preparations and heating sources for the chemical baths and calcinations required to grow $TiO_2$ on Ti.

### *3.1.1 Grinding and Polishing Machine*

Experiments with Ti plates, 9 mm diameter and 4 mm height, were given a rough or polished surface finish by using a Struers TegraForce-5 machine (Figure 3.1) (Mississauga, CAN). Powder preparation for Raman spectroscopy also included polishing following powder being secured into epoxy.


**Figure 3.1: Struers TegraForce-5 used for ground and mirror polish finish on plates.**

### *3.1.2 Water Bath*

The Cole-Parmer RH-400 Standard Heated Circulating Bath, Standard Housing, 7 L; 120 V (Figure 3.2) (Quebec City, CAN) provided a closed system, fluid circulation, and constant temperature control. The water bath was set to the desired experimental temperature and then glass flasks containing the chemicals and Ti plates or powders were placed within to develop $TiO_2$ growth.


**Figure 3.2: Cole-Parmer RH-400 Standard Heated Circulating Bath [137].**

### *3.1.3 Oven*

A Carbolite Laboratory High Temperature (LHT) oven (Derbeyshire, GBR) was also used for chemical experiments to determine if the form of heating affected $TiO_2$ development. The oven was ultimately used to scale up powder production as the ovens larger size allowed for larger beakers than the water bath (Figure 3.3).

**Figure 3.3: Carbolite LHT oven.**

The oven used for experimentation had a thermocouple to verify the temperature. It was seen that when the temperature was set to 88 ℃ the internal temperature maintained 80 ℃ (Figure 3.4).

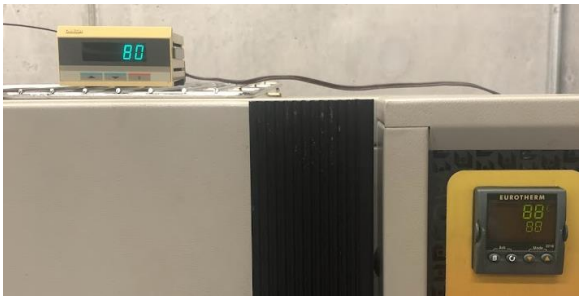


**Figure 3.4: Oven maintained at 80℃ when set to 88℃.**

## 3.2 Titanium Dioxide Characterization

The following sections outline the equipment used for the verification of heterogeneous $TiO_2$ growth on Ti by high magnification images, and phase composition and chemical structure analysis.

### *3.2.1 Scanning Electron Microscopy*

An SEM was used to produce high magnification images of plates and powder for visual characterization of growths before further verification methods. It operates by subjecting the sample to a high energy electron beam and uses detectors to catalogue the interactions and provide information on chemical composition, structure, and shape in a vacuum sealed chamber [138]–[141]. SEM is widely used for its high magnification, large depth of focus, adequate resolution, and ease of use [139]–[144]. The primary electrons of the beam penetrate the surface of the sample to a depth of a few microns and produce secondary electrons, backscattered electrons, and characteristic x-rays (photons). Primary electrons that travel through the sample with either no or minor interactions are catalogued as transmitted electrons and occur if the sample is thin enough for them to pass through [138]–[141], [143]–[145].

Secondary electrons are a low energy result of inelastic collisions and characterize the topography and morphology of the sample up to the first few nanometers. They assist in providing a high-resolution image because they are in a highly localized region around the electron beam source. The presence of secondary electrons can be promoted on the surface by coating the sample with a conductive material [139]–[142], [145].

Backscattered electrons (BSE) result when elastic collisions occur with the primary electrons and sample. As there is no energy loss, further information of the sample structure can be obtained.

BSE signals are well correlated with element atomic numbers which can be used for topography, structure, and element distribution [139]–[142], [145]. X-rays are emitted when electrons are dislodged from precise atom orbits in the sample. The emitted X-rays have the energy characteristics of the atom in which it originated and can therefore provide elemental information [139], [140], [145].

SEM is composed of the following (Figure 3.5) [138]–[141], [144], [145]:

- An electron source (gun).
- Series of electron lenses, including an objective lens, to direct the electron beam.
- Scanning coils that deflect the beam for raster scanning.
- Secondary, backscattered, and x-ray detectors.
- Sample stage.
- Infrastructure requirements:
    - Power supply.
    - Vacuum system.
    - Cooling system.
    - Vibration-free floor.
    - Absence of ambient magnetic and electric fields in environment.

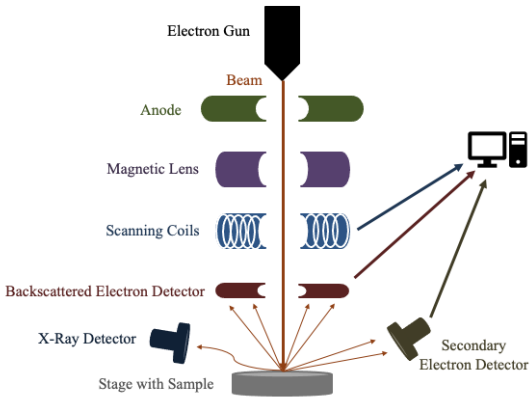


**Figure 3.5: Components of SEM.**

The Zeiss EVO-MA10 (Oberkochen, DEU) was used to examine plate and powder samples (Figure 3.6). Prior to SEM analysis, the samples were adhered to the sample holder using thin double-sided tape and gold sputtered to render the surface conductive to electrons and provide better images by avoiding local electron accumulation and charging.

**Figure 3.6: Zeiss EVO-MA10 SEM.**

### *3.2.2 X-Ray Diffraction*

XRD was used to verify the presence of heterogeneous $TiO_2$ nanostructures. XRD is a non-destructive rapid analysis technique that can identify phase compositions of crystalline substances [146]–[151]. X-ray diffractometers are composed of a cathode x-ray tube, sample holder, and x-ray detector. The cathode x-ray tube filament is heated to accelerate electrons and target collimated x-rays at the sample by applying a voltage.

The XRD setup is composed of the following [146], [152], [153]:

- Sample stage, along the $\theta$ axis.
- X-ray source, along the $\theta$ axis with wavelength $\lambda$.
- Goniometer, a precision device that positions and rotates the sample and/or detector to measure diffracted x-ray angles.
- Optical system, including foils or monochromators, and beam slits to shape and control x-ray paths. These can be located on the incident beam side before the sample or the diffracted beam side before the detector.
- Detector, along the $2\theta$ axis.

The goniometer rotates the sample in the pathway of the collimated x-ray beam of wavelength $\lambda$ at angle $\theta$ with the detector rotating at an angle of $2\theta$. This geometry can be seen in Figure 3.7 [146], [152]–[156].

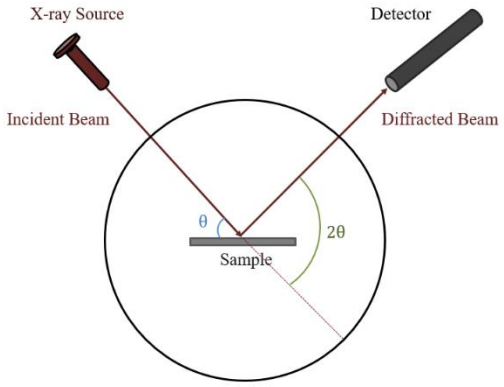


**Figure 3.7: Goniometer geometry of XRD.**

Diffraction is achieved by creating monochromatic x-rays by filtering using foils or crystal monochromators. When the geometry of the incident x-rays impinging upon the sample satisfy Bragg's law (Figure 3.8), then constructive interference causes diffracted x-rays, and peaks of intensity are recorded.

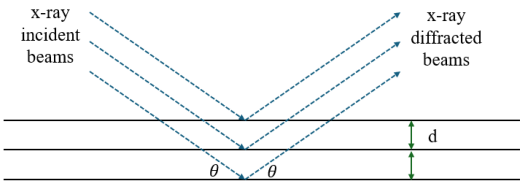


**Figure 3.8: X-ray diffraction within crystalline layers when satisfying Bragg's Law.**

Braggs law is seen in Equation 3.1, where d is the spacing in the family of crystalline lattice planes that reflect the x-rays of wavelength λ at an angle θ (n being a positive integer) [146], [147], [155]. Obtained x-ray spectra contain specific wavelengths coinciding with specific elements and provide material data [151], [155].

$$2\,d\sin\theta = n\,\lambda \qquad \textbf{3.1}$$

The XRD setup used a Rigaku Ultima IV X-ray diffractometer (Tokyo, JPN) equipped with a sealed tube Cu Kalpha source of $\lambda = 1.54184$ A (Figure 3.9).

**Figure 3.9: Rigaku Ultima IV X-ray diffractometer** [157].

### *3.2.3 Raman Spectroscopy*

Raman spectroscopy complemented XRD to confirm successful heterogeneous growth. XRD revealed the overall crystal structure, while Raman provided molecular insights into the $TiO_2$ shell composition near the surface. Raman spectroscopy is a non-destructive analysis technique that can provide information on the chemical structure and crystallinity interactions of the sample. It is a scattering technique based on the Raman effect that analyzes the wavelengths of the laser directed and deflected from the subjected sample. The Raman effect states that the frequency of scattered radiation is different from the incident radiation. Typically, upon contact, most scattered frequencies are equal to that of the incident source and are Rayleigh scattering, as it is an elastic interaction. A lesser amount is scattered due to inelastic collision at a different frequency which is Raman scattering. When the incident laser inelastically collides with the molecules of the sample and produces scattering, those frequency shifts can determine the composition of the sample on a molecular level. The frequencies are measured and recorded through the scattering colliding with a detector. The frequency shift between the incident light and Raman scattered light is called a Raman shift. Raman shifts are compared to known values of chemical structures, morphology, and crystallinity interactions to determine the specifics of the sample. [158]–[165]

A Raman spectroscopy setup is comprised of the following (Figure 3.10) [159], [161], [164], [165]:

- A monochromatic light source.
- The mounted sample.
- Detectors to record scattering.
- A stable environment that is fully sealed to prevent exposure to users.

Raman scattering is a weak phenomenon compared to Rayleigh and so the detectors are typically equipped with a device, like a notch or edge filter, to remove the Rayleigh component [160]–[162], [165].

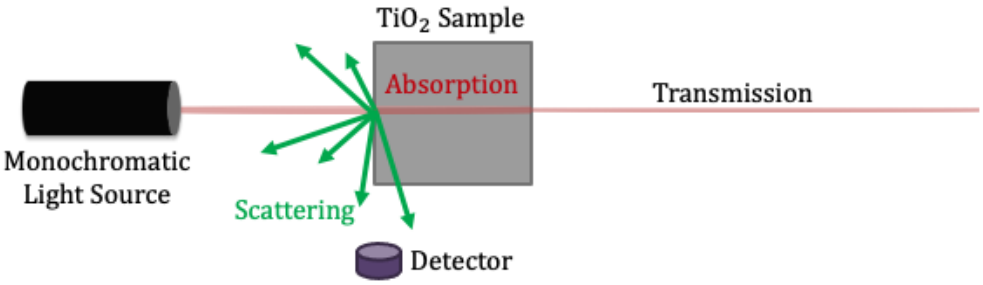


**Figure 3.10: Components of Raman spectroscopy.**

Raman spectroscopy was completed using a HORIBA XploRA Plus Raman Microscope (Burlington, CAN) (Figure 3.11).

**Figure 3.11: HORIBA XploRA Plus Raman Microscope** [166]**.**

## 3.3 Photocatalytic Reactivity Characterization

The following section outlines the equipment used to conduct photocatalytic testing on experimental and commercial powders by generating a UV light source, measuring organic matter degradation by light absorbance, and characterizing the powders surface area which affects adsorption properties.

### *3.3.1 Microprocessor Controlled Light System*

The microprocessor-controlled light curing system can artificially create UV light in a closed system (Figure 3.12). It produces a fast, repeatable, and consistent UV output by using a metal halide type arc lamp powered by a regulated switch-mode power supply, and a precise timer-controlled shutter to regulate light exposure duration [167].

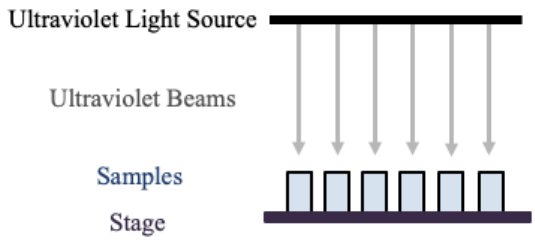


**Figure 3.12: Components of IntelliRay UV box.**

The microprocessor-controlled light curing system was the Uvitron IntelliRay 600 (Massachusetts, USA) (Figure 3.13). It can operate from 35 to 100% of its total power, which is controlled by its front panel [167]. The IntelliRay is stored in a UV safe room within the University of Ottawa so that experiments are not affected by either natural sunlight or artificial light from overhead lighting.

**Figure 3.13: Uvitron IntelliRay 600.**

### *3.3.2 Microplate Reader*

Microplate readers can measure the absorbance in liquid samples. Liquid samples are placed within a well plate within the microplate reader. The microplate reader measures absorbance by using a light source to illuminate the sample along a wavelength specified by the user upon set up and is selected by an optical filter or monochromator. The detector, a spectrometer, is located on the other side of the well and measures how much of the initial light is transmitted through the sample (Figure 3.14) [168]–[170].

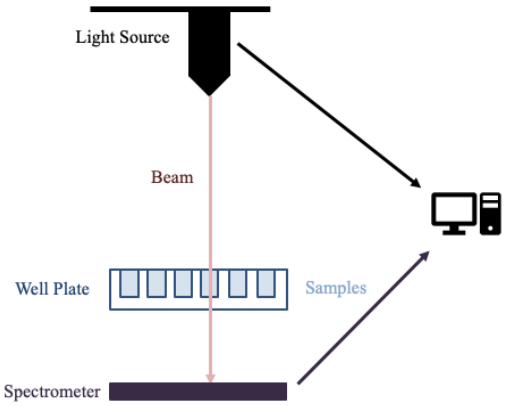


**Figure 3.14: Components of BioTek Synergy H1 Multimode Reader's absorbance measurer mechanism.**

Light transmission is affected by the concentration of molecules within the sample in the wells. Optical density (OD) or light absorbance (A) of the sample (Equation 3.2) [169]:

$$A_\lambda = \log_{10}\left(\frac{I_0}{I}\right) \quad \textbf{3.2}$$

Where:

- $\lambda$ is the specified wavelength that passes through the sample
- $I_0$ is the incident light intensity
- I is the transmitted light intensity

The BioTek Synergy H1 Multimode Reader (Vermont, USA) was the microplate reader used in experimentation to measure the amount of MB desorption in the presence of $TiO_2$ in a mixed aqueous solution (Figure 3.15) [170], [171].

**Figure 3.15: BioTek Synergy H1 Multimode Reader** [170]**.**

Samples were taken at 5-minute intervals, centrifuged, and pipetted into well plates for measuring. VWR 48 Well Treated Tissue Culture Plates were used to hold the samples. The well plates are sterilized with gamma irradiation, clear, and were used within their 3-year shelf life (Figure 3.16) [172].

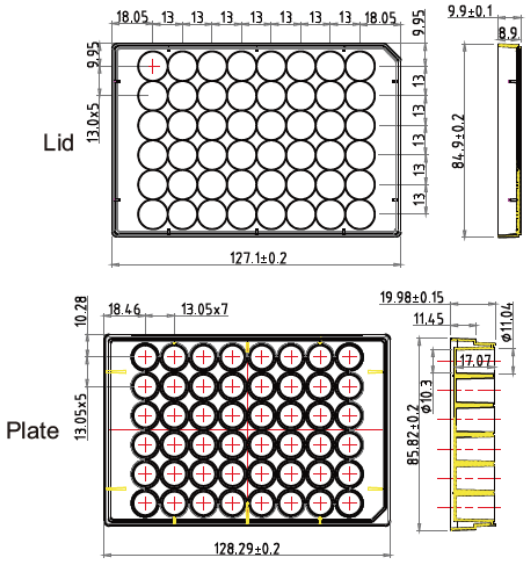


**Figure 3.16: VWR 48 Well Treated Tissue Culture Plate dimensions** [172]**.**

### *3.3.3 Dynamic Vapour Sorption*

DVS measures how quickly and how much of a solvent is adsorbed by a sample through gravimetric sorption and can obtain data on the surface area characteristics of the sample. It is done by varying vapour concentration surrounding the sample and measuring the change in produced mass. DVS requires little sample preparation, primarily the sample being dry before DVS, and no sample destruction [173]–[177]. DVS measures the adsorption and desorption of moisture by flowing a carrier gas at a specific relative humidity (RH) to the suspended sample housed in a weighing mechanism. Factors that can affect readings and stability of the DVS equipment are moisture and temperature, so sensors are located below the housed sample and reference holder. The RH is accomplished by mixing dry and saturated vapour gas and releasing in proportions by mass flow controllers. For baseline stability, there is a microbalance with a reference holder to account for the effects of vapour sorption on the sample holder itself (Figure 3.17) [173], [174], [176], [177].

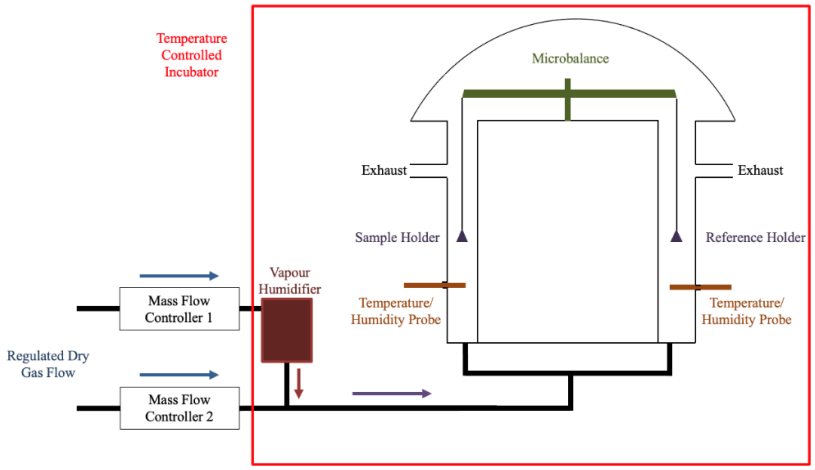


**Figure 3.17: Components of DVS set up.**

In DVS, $S_{BET}$ refers to the Brunauer-Emmett-Teller (BET) specific surface area that is calculated using monolayers data at relative humidity (RH) by the solid surface of a reference mass ($M_{ref}$). When there is a strong interaction between both the vapor molecules and the solid surface, along with the interactions between the vapor molecules themselves, the vapor is adsorbed as a monolayer on the surface, as opposed to being adsorbed in nonuniform clusters. There is the potential of additional complete monolayers forming upon the initial monolayer to create multilayers, indicating a heterogenous surface [178]–[182].

Monolayer data of vapor adsorption is measured through its association to relative pressure, $P/P_0$, where P is the partial vapor pressure of the sample in the system and $P_0$ is the saturation vapor pressure at the same temperature. Brunauer states there are five types of isotherms, which is the relationship between the amount of vapor adsorbed and the relative pressure at a given temperature to provide the monolayer, multilayer, or condensation characteristics. The five types surface features are summarized below, and the BET curves are shown in
Figure 3.18 [178], [179], [183]–[185].

- Type I
    - Quick uptake at low pressure followed by a plateau at saturation that indicates monolayer adsorption of a microporous material with pore diameters less than 2 µm.
- Type II

- S-shaped curve that indicates complete initial monolayer formation and beginnings of multilayers of a non-porous or macroporous material with pore diameters larger than 50 μm.

- Type III
  - A weak interaction with no asymptote in the curve indicates no monolayer is formed and BET is not applicable.
- Type IV
  - Capillary condensation occurs where the rate of adsorption is quicker than desorption indicating initial monolayer formation and beginnings of multilayers of a mesoporous material with pore diameters between 2 – 50 μm.
- Type V
  - A weak interaction producing a graph similar to Type IV. Multilayer formation begins before initial monolayer completion and BET is not applicable.

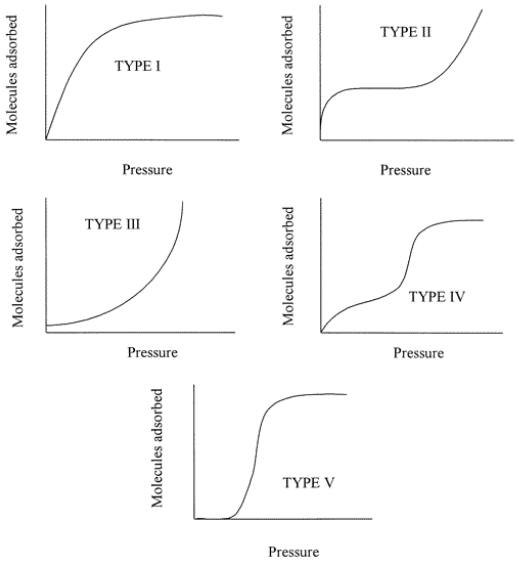


**Figure 3.18: Brunauer's five types of adsorption isotherms** [178]**.**

DVS was completed at the National Research Council (NRC) (Ottawa, CAN) on the developed experimental $TiO_2$ powder and the two commercial $TiO_2$ powders, Altair and Neoxid. DVS was done to characterize the surface areas of the powders and understand the adsorption behaviours for how that could affect photocatalytic activity. The NRC DVS set up can be seen in Figure 3.19.


**Figure 3.19: NRC DVS set up.**

# 4 TITANIUM PLATE TREATMENTS

## 4.1 Methodologies

Experiments were first completed on Ti plates to observe if a successful growth of $TiO_2$ was achieved by chemical bath. Ti plates were used for two reasons; much of the reference literature conducted experiments on Ti plates and could be used for comparison, and because they were readily available whereas there was a delay in obtaining Ti powder. Additionally, the large surface area of Ti could allow for quick verification of seeing apparent growth along the surfaces with the naked eye. The following section discusses the procedures and outcomes of the titanium plates. The plate experiments were referenced as T-#, where T symbolized 'plate' and the # is a plate batch that underwent a chemical bath.

All experiments with Ti plates, 9 mm diameter and 4 mm height, were roughly surface finished utilizing 200 grit grinding disc or polished utilizing 1200 grit polishing disc. A finishing was completed because the Ti plates were cut from a Ti rod and had rougher surfaces. Plates were surface finished to remove surface oxidation, immediately ultrasonically cleaned, and then then added to the chemical bath.

An acrylic gel tape was used to attach the plates to the machine sample holder for polishing because the plates were too small to fit into the machines sample holders. They were affixed with the gel to the base of a sample holder; this method proved efficient in ensuring plate surface contact to the grinding and polishing faces since using a thinner tape resulted in the plates detaching from the sample holder.

### *4.1.1 Hot Plate*

Through literature it was seen that experiments had success in developing $TiO_2$ nanostructures on Ti using a $H_2O_2$ bath [78], [92], [93]. A preliminary experiment (T-1) was completed using a Fisher Scientific hot plate and glass beaker before the water bath was received. Two Ti plates were roughly surface finished utilizing 200 grit grinding surfaces, ultrasonically cleaned in deionized water, and placed in 50 mL of $H_2O_2$ at 80 ℃ on a hot plate under a fume hood. The experiment used 30 wt% $H_2O_2$ from Fisher Scientific. A thermocouple was placed into the $H_2O_2$ to verify its

temperature (Figure 4.1). The experiment was to be maintained at 80 ℃ for 3 days. The plates were left to dry for two days under the fume hood before SEM imaging.

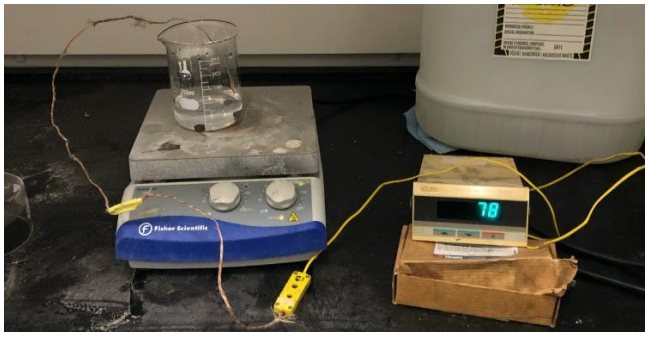


**Figure 4.1: Initial experiment with beaker, hot plate, and thermocouple.**

### *4.1.2 Hydrogen Peroxide Chemical Bath*

Ti plates were roughly surface finished utilizing 200 grit grinding disc or polished utilizing 1200 grit polishing disc and placed in a 125 mL flask that contained 100 mL of $H_2O_2$ at 80 ℃ for 72 hours. The experiments used 30 wt% $H_2O_2$ from Fisher Scientific. The purpose in initially using a water bath was to promote circulation and increase even heat transfer throughout the flask and $H_2O_2$.

The experimental set up had the flask held by an external arm and a coated carboard cover was used with a hole the diameter of the flask top to allow the flask to extrude from the water bath. The stopper in the flask had a small hole to prevent chemical pressure and gas buildup, minimize evaporation of the $H_2O_2$, and be large enough to insert a thermometer to verify the internal flask temperature. The entire water bath set up was also placed under a closed fume hood (Figure 4.2). All samples were ultrasonically cleaned in deionized water prior to chemical immersion and subsequently rinsed three times with deionized water upon experiment completion and air dried before SEM imaging.

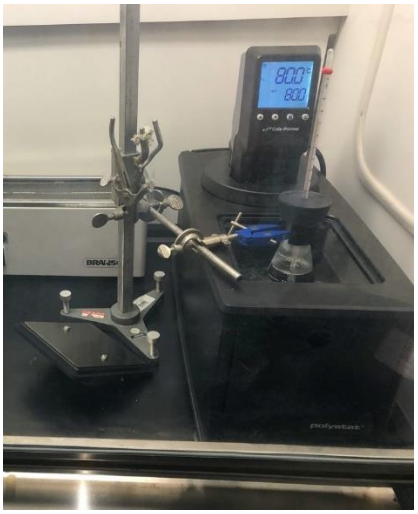

**Figure 4.2: Initial water bath set up without bath cover.**

Three independent batches were completed using the second experimental set up. All batches were surface finished, ultrasonically cleaned in deionized water, dried with compressed air, and submerged in $H_2O_2$ for three days. Each step began immediately following the completion of the previous. Batches T-2, T-3, and T-4 were conducted of similar chemical bath parameters while the experimental set up was being developed. The objectives were liquid retention and consistent, promising results. Batch T-2 used coated cardboard as its cover and experienced water loss. A plastic cover was used for Batches T-3 and T-4. Plate surface finishes, $H_2O_2$ final volume, and water level decreases are in Table 4.1.

**Table 4.1: First plate experiments completed in $H_2O_2$ bath.**

| Batch | Surface Finish | Final $H_2O_2$ Volume | Approximate Decrease in Water Level |
|---|---|---|---|
| **T-2** | Polished | 75 mL | 3 cm |
| **T-3** | Polished | 60 mL | 1 cm |
| **T-4** | Rough | 65 mL | 1 cm |

Water loss presented a concern early on as the water bath was not efficiently covered. The external arm used to hold the flask prevented submersion further than the 100 mL mark on the flask. The arm was replaced with a flask weight that allowed the provided water bath cover to be used and create a better seal (Figure 4.3). This set up proved to prevent water loss within the water bath and maintain temperature. Ti plates were roughly ground or polished and placed in a 250 mL flask that contained 100 mL of $H_2O_2$ at 80 ℃ for 72 or 96 hours.

**Figure 4.3: Water bath set up with flask weight and in water bath without cover on.**

Three batches of five variations were first completed. T-5, T-6a, and T-6b were covered with a plastic cover that had a hole to note if gas buildup would be a concern and if there needed to be an outlet for pressure and/or fumes. T-6a and T-6b were prepared at the same time and part of the same experiment, except T-6b was removed from the water bath 24 hours later. The same was done for T-7a and T-7b, except the water bath cover was used. Plate surface finish, experiment duration, and the heating equipment used are outlined in Table 4.2.

**Table 4.2: Subsequent plate experiments completed in $H_2O_2$ bath.**

| Batch | Surface Finish | Duration (hours) | Heating Equipment |
|---|---|---|---|
| **T-5** | Polished | 72 | Water bath |
| **T-6a** | Polished | 72 | Water bath |
| **T-6b** | Polished | 96 | Water bath |
| **T-7a** | Polished | 72 | Water bath |
| **T-7b** | Polished | 96 | Water bath |

### *4.1.3 Hydrogen Peroxide, Nitric Acid, & Melamine Chemical Bath*

Undesirable results were obtained through $H_2O_2$ experiments. The primary reference literatures utilized a brand of $H_2O_2$ from Sinopharm Group Co. (Shanghai, CHN) [78], [92], [93], [95]. Industrial and technical grade $H_2O_2$ ranging from 30 to 50% in concentrations have the possibility of housing impurities due to permissible stabilizers and trace contaminants [186], [187]. The presence of certain impurities in the Sinopharm Group Co. $H_2O_2$ different to Fischer Scientific $H_2O_2$ could affect the interactions between the Ti and $H_2O_2$ and subsequent experimental results. The chemical bath procedure was redeveloped to include $HNO_3$, to increase acidity and control uniformity, and $C_3N_3(NH_2)_3$, to improve charge separation and band structure. As $C_3N_3(NH_2)_3$ hydrolyzes to urea and then ammonia it creates a pH environment together with $HNO_3$ and $H_2O_2$

that supports the growth of nanorods and nanowires [97]–[100], [188]–[190]. The chemical specifications can be seen in Table 4.3.

**Table 4.3: Chemical specifications for plates in $H_2O_2$, $HNO_3$, and $C_3N_3(NH_2)_3$ bath.**

| Chemical | Annotation | Supplier | Concentration | Amount Used |
|---|---|---|---|---|
| **Hydrogen peroxide** | $H_2O_2$ | Fischer Scientific | 30 wt % | 50mL |
| **Nitric acid** | $HNO_3$ | Fisher Scientific | 68-70 wt % | 1mL |
| **Melamine** | $C_3N_3(NH_2)_3$ | Fischer Scientific | 99 % | 60 mg |

The chemical bath duration was also decreased to 12 hours as nanostructural growth would be present at that stage [95], [97]. Calcination on select samples was completed 450 ℃ for 1 hour to observe the changes in morphology if hydrogen titanate nanostructures were initially grown and thermally transformed to anatase with improved crystallinity and higher SSA [56], [62], [78], [90], [98], [100], [105].

In summary the following changes were made:

- The addition of $HNO_3$, and $C_3N_3(NH_2)_3$ to the chemical bath.
- Reduction in experiment duration to 12 hours.
- Experiments conducted in an oven.
- Plates were placed in chemical bath immediately after ultrasonic mixing and prior to heat subjection, meaning they had a cold start. Previously the $H_2O_2$ had been brought up to 80 ℃ prior to adding plates.
- Calcination at 450 ℃ for 1 hour was completed on select samples to observe changes in morphology.

The final batches of plate experiments were done in two batches with four variations. T-8a and T-8b were prepared with different surface finishes, placed in the same chemical bath in the water bath, and calcinated 450 ℃ for 1 hour. T-9a and T-9b were prepared together, placed in separate chemical baths in separated heating equipment (T-9a in the water bath and T-9b in the oven), and not calcinated. Plate surface finishes, experiment duration, heating equipment used, and if the plates were calcinated are seen in Table 4.4.

**Table 4.4: Plate experiments completed in $H_2O_2$, $HNO_3$, and $C_3N_3(NH_2)_3$ bath.**

| Batch | Surface Finish | Duration (hours) | Heating Equipment | Calcinated |
|---|---|---|---|---|
| **T-8a** | Polished | 12 | Water bath | Yes |
| **T-8b** | Rough | 12 | Water bath | Yes |
| **T-9a** | Rough | 12 | Oven | No |
| **T-9b** | Rough | 12 | Water bath | No |

## 4.2 Microstructure Analysis

### *4.2.1 Hot Plate*

The SEM images (Figure 4.4) presented no nanostructural growth on T-1. The Ti plates ground surface remained unchanged. No apparent change in the plates surface could have been due to the experimental set up factors, such as the open beaker system, surface oxidation on the plates, heating via conduction at the bottom of the beaker, the Ti to $H_2O_2$ ratio, or contamination from the thermocouple which had been used in previous laboratory experiments.

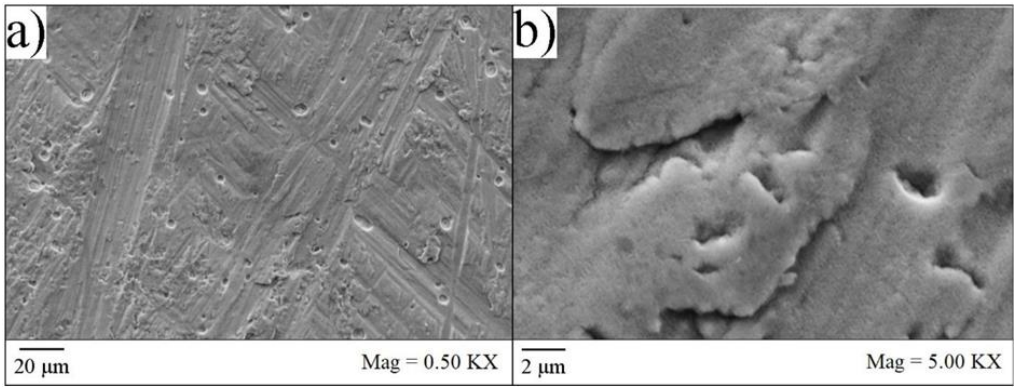


**Figure 4.4: SEM at a) 0.50 KX and b) 5.00 KX of Ti plate from $H_2O_2$ bath on hot plate that experienced complete evaporation.**

### *4.2.2 Hydrogen Peroxide Chemical Bath*

At the end of T-2 the $H_2O_2$ level had decreased from 100 mL to 75 mL (Figure 4.5). With a new water bath cover, T-3 and T-4 exhibited a larger decrease in $H_2O_2$ but better water retention in the water bath. All three batches had identical preparations and set ups, except for T-4 having a different surface finish procedure. The black line in Figure 4.5 marked the maximum water line in the water bath. After 3 days, the water decreased. The arm restricted the depth in which the flask could be submerged in the bath. At the beginning of experimentation, the 100 mL of $H_2O_2$ was just under the water line, but upon the completion of the three days the flask was submerged to the 50 mL mark, leaving the top 25 mL of the remaining $H_2O_2$ not submerged in the 80 ℃ water.


**Figure 4.5: Batch T-2 in water bath after three days.**

When the experiments were removed from the water bath after three days the $H_2O_2$ had a murky appearance and a thin blue-grey film could be directly seen on the plates (Figure 4.6).

**Figure 4.6: Batch T-3 plates inside flask upon removal from water bath.**

The thin blue-grey film remained on the plates following rinsing with deionized water and drying (Table 4.5), indicating that not only was there growth on the plates, but that it presented adhesion which could withstand the thrice rinsing, drying, and handling to prepare for SEM.

**Table 4.5: Plates prior to SEM for Batches T-2 to T-4.**

| Batch T-2 | Batch T-3 | Batch T-4 |
|---|---|---|
|  Plate surface sides that were facing upward in flask during chemical bath showing iridescent film along left plate and blue-grey film along right plate. |  Plate surface sides that were facing upward in flask during chemical bath showing blue-grey film. |  Plate surface sides that were facing upward in flask during chemical bath showing blue-grey film. |
|  Plate surface sides that were in contact with bottom of flask during chemical bath showing that each plate had an iridescent film on one side and blue-grey film on other side. | 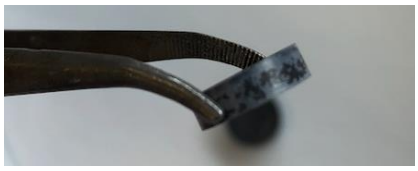 Side of plate showing uneven layer of blue-grey film. | |

The only batch to present an iridescent appearance was T-2, which also experienced the most water loss in the water bath and the lowest decrease in $H_2O_2$ level. The loss of water could have produced lower reactions between Ti and $H_2O_2$ due to lack of temperature control at 80 ℃ as majority of the flask was not submerged in the water bath. Evaporation of $H_2O$ in the flask would increase the concentration of the $H_2O_2$ breakdown products and affect the pH by slightly raising its acidity. Additionally, even though the top of the flask was covered, the coated cardboard cover could have introduced elements that interacted with the experiment. The uncontrolled experimental environment created higher fluctuations in temperature, $H_2O$ evaporation, $H_2O_2$ decomposition, and potential contamination than in the subsequent experiments.

T-2 had flaked deposits along the surface of the Ti plate that resembled if growth had developed along the surface and then curled inward resulting in poorer adhesion and cracking (Figure 4.7 a) and b)). It appeared the growth had begun development and then lacked the necessary conditions to maintain an even coating and continue upward growth. Along the flaked pieces of coating, a

network of slightly convex textures could be seen, especially at 1.50 KX magnification (Figure 4.7 c)). The convex growths appeared to potentially be the preliminary development of nanoroads growth as seen in literature (Figure 2.7). The cross section of the flaked coatings was fibrous, showing upward growth from the Ti plate (Figure 4.7 d)). The upward growth and then beginning of convex texture could be congruent with the beginning of a base that progresses to nanostructural growth.

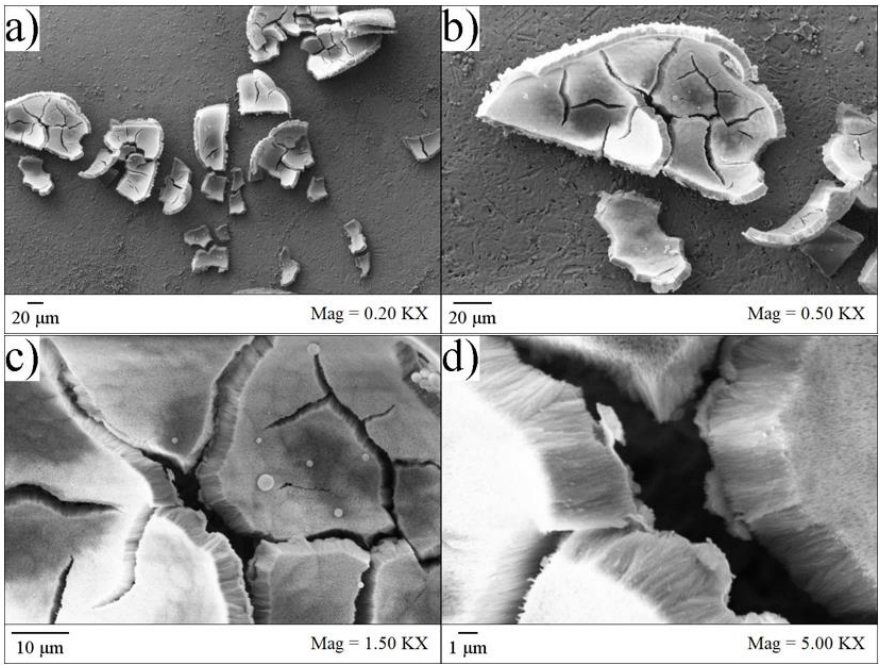


**Figure 4.7: SEM images of T-2 at a) 0.20 KX, b) 0.50 KX, c) 1.50 KX, and d) 5.00 KX. Experienced significant water bath evaporation resulting in uneven, poorly adhered deposits with perpendicular growth to plate surface.**

T-3 had a more even coating along its surface which had not curled inward but did present cracking predominantly near the edge of the plate (Figure 4.8 a)). The network of convex growths surface seen in T-2 was much more apparent in T-3 with clear pores along the surface (Figure 4.8 b) and c)). The growth appeared more even, textured, and covered more of the Ti plate surface. It appeared to be more successful than T-2 while still not producing optimal results. It appeared the base of nanostructural growth was present with slight porosity (Figure 4.8 d)) but lacking the conditions to achieve further structural growth.

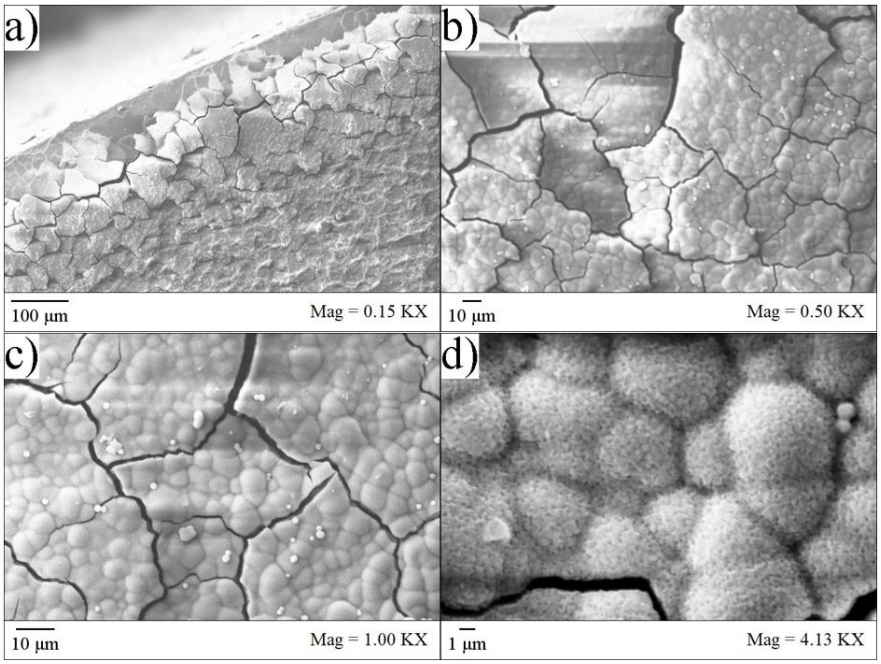


**Figure 4.8: SEM images of T-3 at a) 0.15 KX, b) 0.50 KX, c) 1.50 KX, and d) 5.00 KX. Improved water bath retention resulted in more even and better adhered convex, porous growths along the plate surface.**

T-4 was completed identical to T-3 for experimental consistency and presented similar results of textured, porous growth that evenly coated the Ti plate (Figure 4.9 a)). It also showed cracking throughout, but no pieces curled inward like in T-2 (Figure 4.9 b) and c)). The convex surface network provided promising results of potential early stages of nanostructural growth with increased porosity and SSA for increased active sites and ROS generation for photocatalytic activity (Figure 4.9 d)).

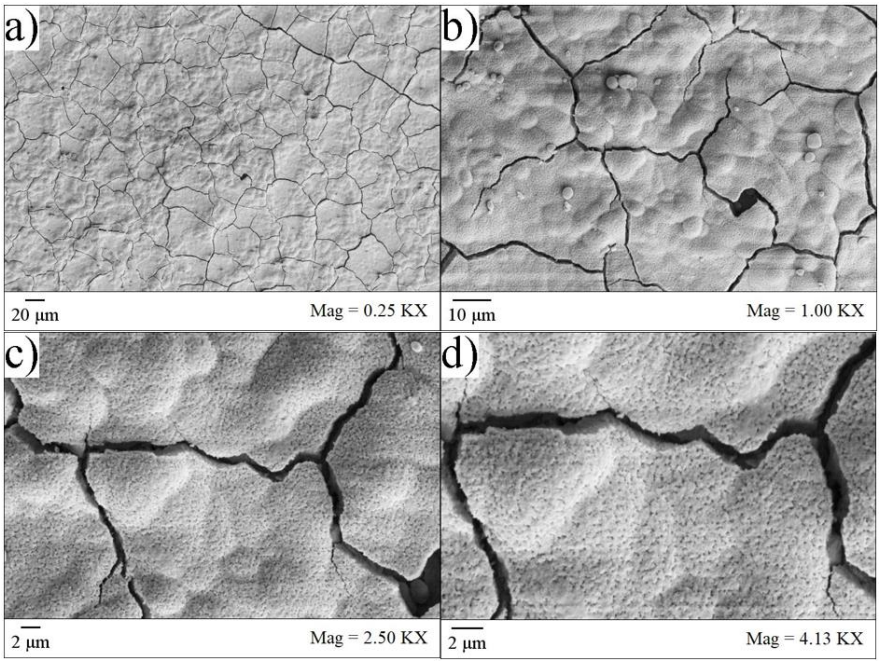


**Figure 4.9: SEM images of T-4 at a) 0.25 KX, b) 1.00 KX, c) 2.50 KX, and d) 4.13 KX. Improved water bath retention resulted in more even and better adhered convex, porous growths along the plate surface.**

The experimental procedure with the flask weight provided environmental control where the water and $H_2O_2$ levels were maintained. T-5 exhibited a blue film with equal coverage on the plates. T-6a and T-7a had a yellow film on the plates with T-7a having more coverage. T-6b had a dark grey film and T-7b had an inconsistent blue film. All layers were darkened after gold sputtering before SEM imaging (Figure 4.10).

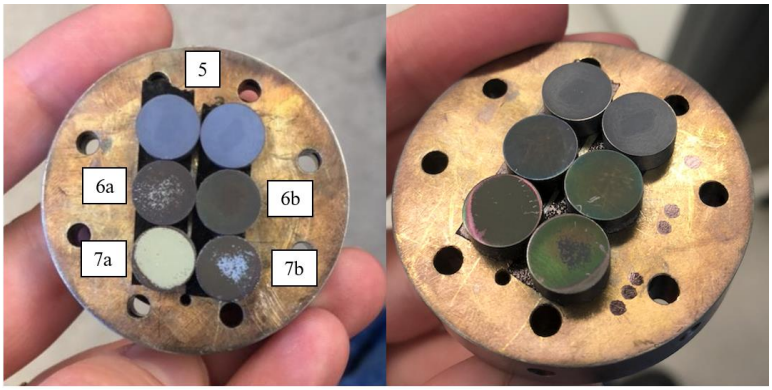


**Figure 4.10: Samples before (left) and after (right) gold spatter prior to SEM imaging.**

T-5 presented the most even growth with the most coverage along the Ti plate (Figure 4.11 a)). It also had less cracking, and the presented cracks were thinner than those previously seen (Figure 4.11 b)). T-5. maintained the porous surface with convex growths, but with more texture and complexity (Figure 4.11 c) and d)). The growth appeared be better adhered than T-2 to T-4 batches.

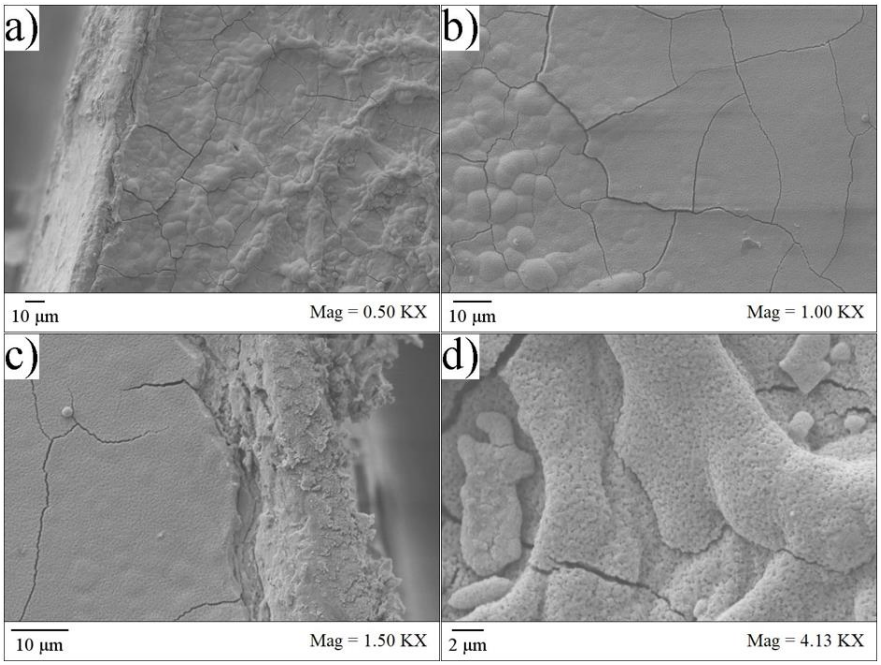


**Figure 4.11: SEM images of T-5 at a) 0.50 KX, b) 1.00 KX, c) 1.50 KX, and d) 4.13 KX. First experiment with flask weight ensured complete submersion of $H_2O_2$ in flask below water line. Growths presented less cracking with more diverse textual growths along plate surface.**

T-6 did not have the porous surface network previously seen, it was rough with no apparent porosity present (Figure 4.12 a)). Slight fibrous was seen in T-6b (Figure 4.12 b)) and not on T-6a (Figure 4.12 c)). Higher magnification did not show the growth to have porous nature (Figure 4.12 d)). The addition of water evaporating and condensing into the flask raised the volume from 100 mL to 125 mL, diluting the $H_2O_2$ concentration altered the conditions and negatively impacted growth development.

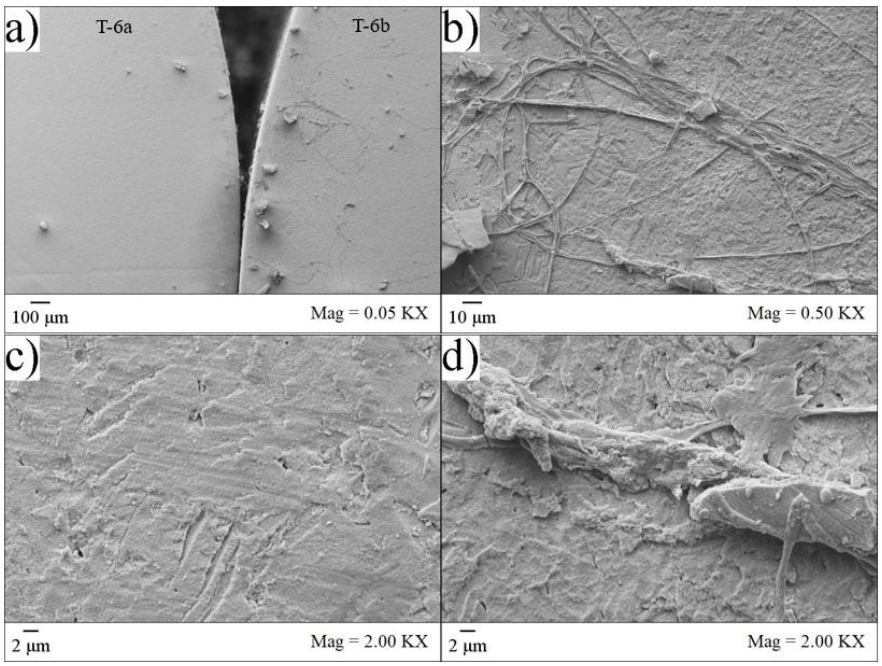


**Figure 4.12: SEM images at a) 0.05 KX of the edges of T-6a and T-6b, b) 0.50 KX of T-6b, c) 2.00 KX of T-6a, and d) 2.00 KX of T-6b. The addition of condensed water from the water bath diluted the $H_2O_2$.**

The growths along T-7a and T-7b had more successful growths than previously seen (Figure 4.13 a)). The growths along T-7a and T-7b were the first seen to have two clear layers grown one on top of the other (Figure 4.13 b) and c). The lower layer was rough with no clear directional growth, where the top layer grew upwards, congruent with what had been seen in previous batches. They both had convex, porous layers with cracks and appeared to have the beginning of desired nanostructures in spiked appearance (Figure 4.13 d)), corresponding to nanorods seen in literature (Figure 2.7). T-7b had an additional 24 hours of $H_2O_2$ submersion and had stronger spike formations. These results appeared to be further progressed than what was seen in previous batches that had a porous surface without the beginning of spiked growth. The growth was in line with the desired results, while still being smaller, further indicating an adjustment needed to be made to the experimental procedure.

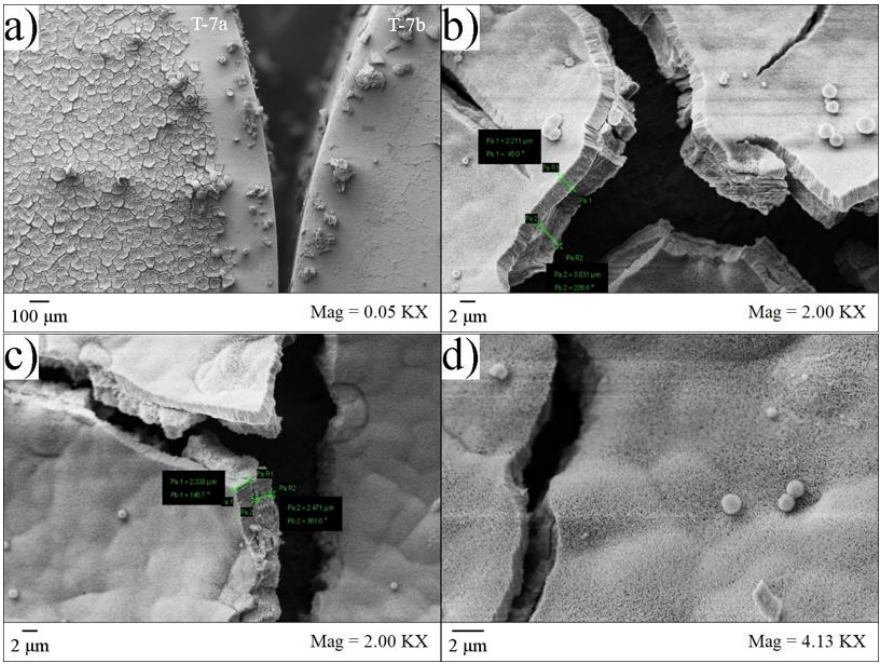


**Figure 4.13: SEM images at a) 0.05 KX of the edges of T-7a and T-7b, b) 2.00 KX of T-7b, c) 2.00 KX of T-7a, and d) 4.13 KX of T-7b. The addition of condensed water from the water bath diluted the $H_2O_2$.**

It was seen in literature that cracks occurred in Ti plate growths when the $H_2O_2$ concentration was too high and Ti was immersion too long as thicker layers carried higher risks of cracking upon removal and drying[91], [93], [94], [99]. This indicated the experimental procedure was too long with too much $H_2O_2$ as growths cracked, but the beginning of the desired nanostructures indicated with more time, potentially further growth could occur. This prompted revising the chemical bath with the aim of reducing time and increasing growth by additives that could alter the pH to promote anatase and rutile heterojunctions.

### *4.2.3 Hydrogen Peroxide, Nitric Acid, & Melamine Chemical Bath*

The results with the new chemical bath produced diverse growths with apparent low porosity. In T-8, the growths varied in height, having smooth surfaces with cracks throughout (Figure 4.14). Overall, there was a clear increase in growth on the Ti plate, but the desired nanorod or spike formations were not present. No change in results was seen between ground and polished surfaces on the Ti plates prior to immersion in the chemical baths. It was concluded that for the plates, oxidation did not play a large factor in the results regarding the amount and appearance of growths.

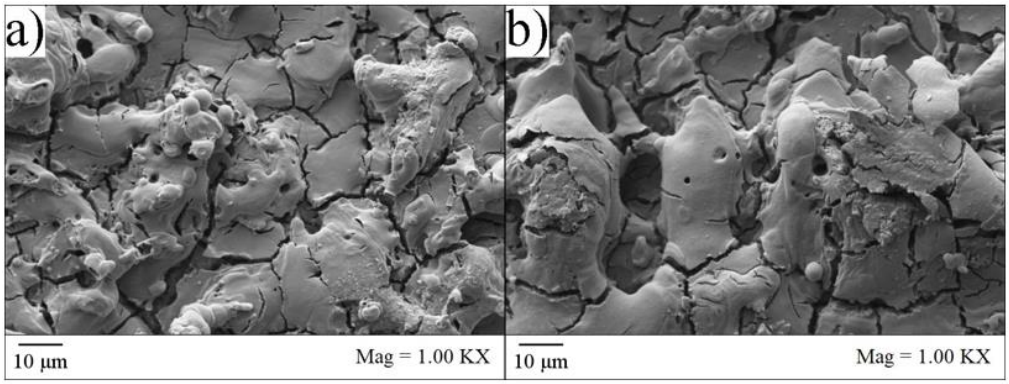


**Figure 4.14: SEM images at 1.00 KX of a) T-8a and b) T-8b as the first experiment following the updated chemical bath of $H_2O_2$, $HNO_3$, and $C_3N_3(NH_2)_3$ exhibiting highly textured surfaces with low apparent porosity.**

T-9a and T-9b were completed with plates prepared together and then placed into two chemical baths, one for the oven and one for the water bath, respectively. At the end of experimentation T-9a was clear, dark orange in colour, with T-9b being a murky, deep yellow (Figure 4.15). Literature stated that $H_2O_2$ could turn an orange-yellow colour with the release of titanium ions and that the eventual decrease in orange-yellow colouration indicated the $H_2O_2$ has been consumed [92], [93]. This indicated that both experiments did not fully consume all $H_2O_2$ and that T-9b appeared to have utilized more $H_2O_2$ than T-9a. Both plates looked similar in appearance upon removal from their chemical baths and rinsed thrice with deionized water.

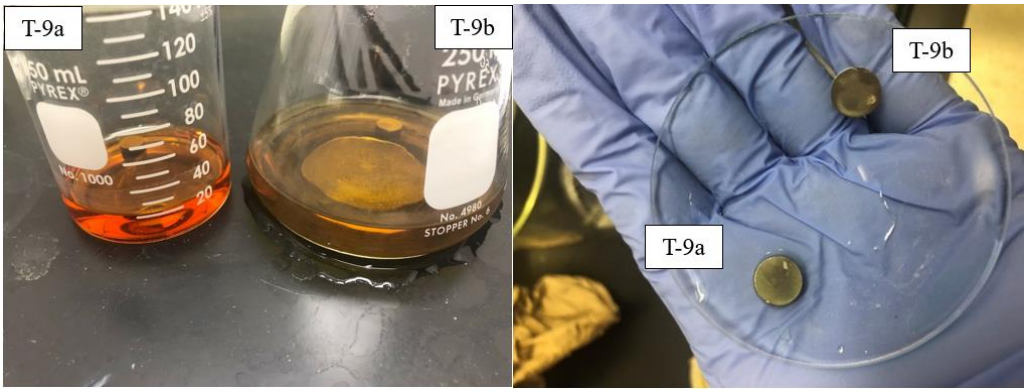


**Figure 4.15: Batches T-9a and T-9b at end of chemical bath.**

T-9a had similar topography to T-8 with lots of texture (Figure 4.16 a) and b)) but lack of porosity (Figure 4.16 c) and d)). The volume of the beaker placed in the oven dropped from 50 mL to 20 mL, whereas T-9b in the water bath experienced no volume loss. The oven experiment was sealed with thin plastic, which proved to be inefficient in retaining liquid and evaporation created inconsistent pH conditions.

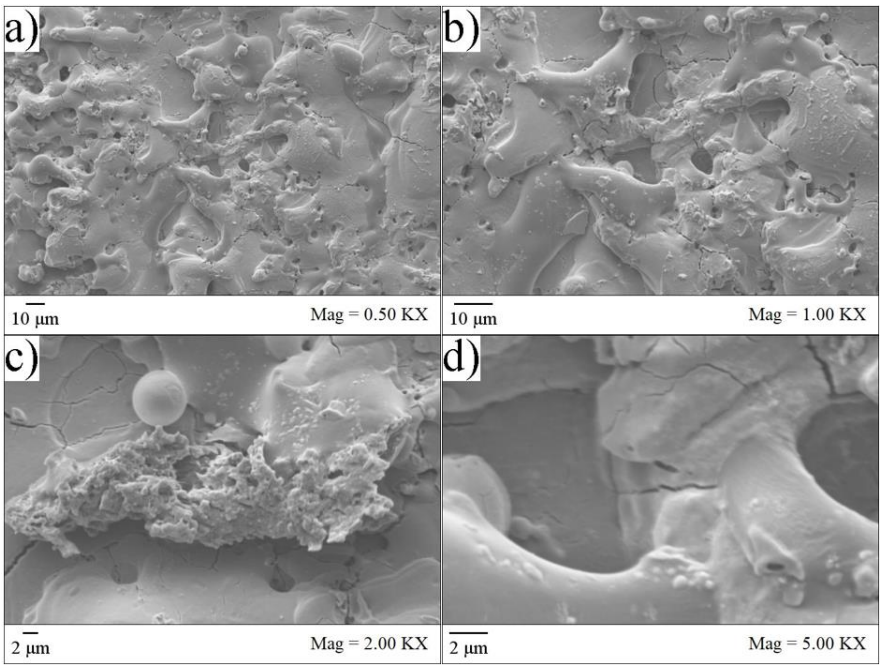


**Figure 4.16: SEM images of T-9a at a) 0.50 KX, b) 1.00 KX, c) 2.00 KX, and d) 5.00 KX which experienced significant evaporation. The growths presented low apparent porosity but with highly textured surface.**

Cracking occurred in T-9b, but continuous growth incorporated it into new growth creating a strong and consistent geometry along the plate (Figure 4.17 a)). The coating appeared thick, with the highest surface area in appearance out of all plate experiments with its extremely porous framework (Figure 4.17 b)). As predicted by the yellow colour and liquid retention in the flask upon removal from the water bath, T-9b exhibited a more porous and higher SSA surface than T-9a, with sponge-like topography (Figure 4.17 c) and d)).

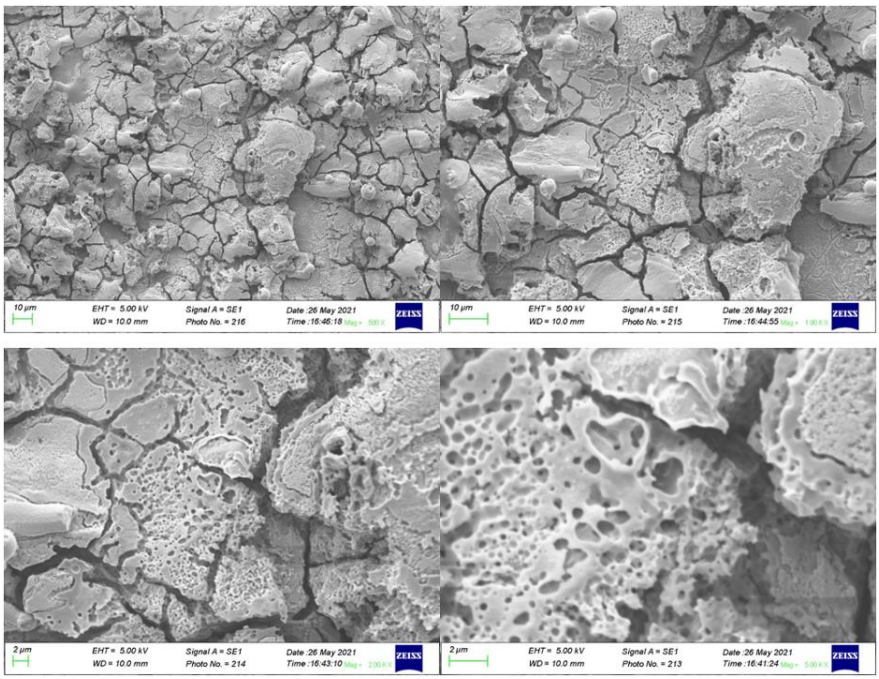


**Figure 4.17: SEM images of T-9b at a) 0.50 KX, b) 1.00 KX, c) 2.00 KX, and d) 5.00 KX which efficiently retained liquid levels. The growths presented high apparent porosity and SSA with a sponge-like surface.**

Ultimately promising results were developed on the Ti plates with highly porous, even nanostructural growth. A consideration in experimentation could be the amount of Ti present in the chemical baths. When compared to literature, samples were typically much smaller than the 9 mm diameter and 4 mm height plates used. Additionally, the chemical bath remaining yellow in colour suggests there was more $H_2O_2$ available for consumption. Ultimately, the plate experiments confirmed growth on Ti and the experimental procedure was refined while powder was in transit. Upon the receival of powder, the priority was shifted to powder experiments.

# 5 TITANIUM POWDER TREATMENTS

## 5.1 Methodologies

Powder experiments overlapped with plate experiments (T-5 to T-10). Ti powder was the primary choice of material for experimentation since the objective was powder development for CGDS, and powder experiments began upon its delivery. The Ti powder used was Advanced Powders and Coatings (AP&C) spherical grade 1 CP-Ti with particle size 15 - 45 μm and a typical oxygen content of 0.16 wt % [180]. SEM images showed the CP-TI powder particles were smooth and spherical with no textured surface growths prior to experimentation (Figure 5.1).

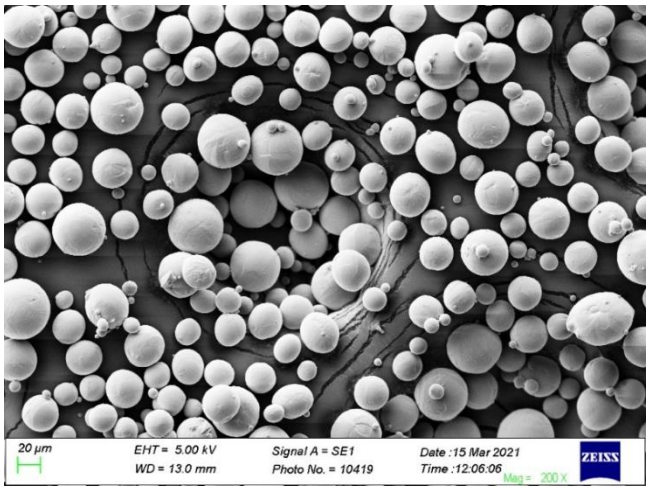


**Figure 5.1: SEM image of untreated CP-Ti powder.**

The CP-Ti powder was opened under vacuum within a glove box and 1-gram (g) samples were placed in glass vials (Figure 5.2).

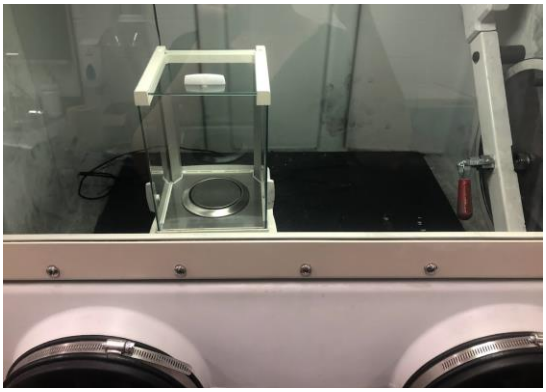

**Figure 5.2: Glove box under vacuum with scale used for CP-Ti powder separation.**

The vials were individually sealed and then vacuum sealed. The powder container was sealed in the same manner (Figure 5.3).


**Figure 5.3: CP-Ti powder separated and resealed.**

The powder experiments were referenced as P-#, where P symbolized 'powder' and the # was the batch of powder that underwent the same chemical bath. For SEM imaging, the powders were adhered to the sample holder using thin double-sided tape and then gold sputtered to render the surface more conductive to electrons and provide better images by avoiding local electron accumulation and charging

### *5.1.1 Hydrogen Peroxide Chemical Bath*

The experimental procedure established with the plates in 4.1.2 was carried over to the powder, except the powder did not require a surface finish procedure. Chemical bath specifications are seen in Table 5.1.

**Table 5.1: Chemical specifications for powder in $H_2O_2$ bath.**

| Component | Annotation | Supplier | Concentration |
|---|---|---|---|
| **Titanium powder** | $CP-Ti$ | AP&C | - |
| **Hydrogen peroxide** | $H_2O_2$ | Fischer Scientific | 30 wt % |

The powder was removed from its vacuum seal, measured, and immediately added to $H_2O_2$ which was either preheated to 80 ℃ (hot start) or at room temperature (cold start) (
Figure 5.4). The purpose of having hot and cold starts was to note a difference in results between powders that were subjected to an immediate 80 ℃ or were gradually warmed up with the $H_2O_2$. After 72 hours in the $H_2O_2$ bath, in either the water bath or oven, the powder was rinsed three times with deionized water and let dry completely before SEM imaging. Experiments were completed in both the water bath and oven to compare different heating methods and see if convective heating through circulating water provided consistent temperature to the $H_2O_2$ that altered results when compared to stationary air in an oven.

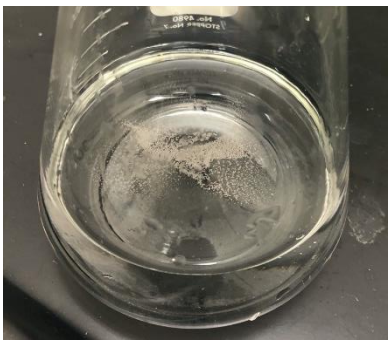

**Figure 5.4: CP-Ti powder added to $H_2O_2$.**

Five powder batches were completed using this methodology (Table 5.2). P-5 was scaled up proportionally to note any changes in results. A benefit of the oven was that due to its size it allowed for larger batch sizes than the water bath.

**Table 5.2: Powder experiments completed in $H_2O_2$ bath.**

| Batch | Start | Heating Equipment | CP-Ti (mg) | $H_2O_2$ (mL) |
|---|---|---|---|---|
| **P-1** | Hot | Water bath | 100 | 100 |
| **P-2** | Cold | Water bath | 100 | 100 |
| **P-3** | Cold | Oven | 100 | 100 |
| **P-4** | Cold | Water bath | 100 | 100 |
| **P-5** | Cold | Oven | 200 | 200 |

### *5.1.2 Hydrogen Peroxide, Nitric Acid, & Melamine Chemical Bath*

The procedure established with the plates in 4.1.3, was carried over to the powder, except the powder did not require a surface finish procedure. The chemical bath component specifications can be seen in Table 5.3.

**Table 5.3: Chemical specifications for powder in $H_2O_2$, $HNO_3$, and $C_3N_3(NH_2)_3$ bath.**

| Component | Annotation | Supplier | Concentration |
|---|---|---|---|
| **Titanium powder** | $CP-Ti$ | AP&C | - |
| **Hydrogen peroxide** | $H_2O_2$ | Fischer Scientific | 30 wt % |
| **Nitric acid** | $HNO_3$ | Fischer Scientific | 68-70 wt % |
| **Melamine** | $C_3N_3(NH_2)_3$ | Fischer Scientific | 99 % |

The chemical bath was ultrasonically mixed for 10 minutes to combine the $H_2O_2$, $C_3N_3(NH_2)_3$, and $HNO_3$, the CP-Ti powder was then added and the beaker was placed in either the oven or water bath at 80 ℃ for 6, 8, 12, or 24 hours. At the conclusion of the chemical bath, the powder was rinsed three times with deionized water and let air dry under the fume hood before potential calcination at 450 ℃ for one hour. Calcination was added as a last step to the experimental powder procedure to decompose the hydrogen titanate nanowires to anatase. The final powder procedure

can be seen in Figure 5.5 where the calcination in step 5 is notated in grey as it was not completed for all powder experiments. Complete experimental parameters are included in tables later in this chapter section.

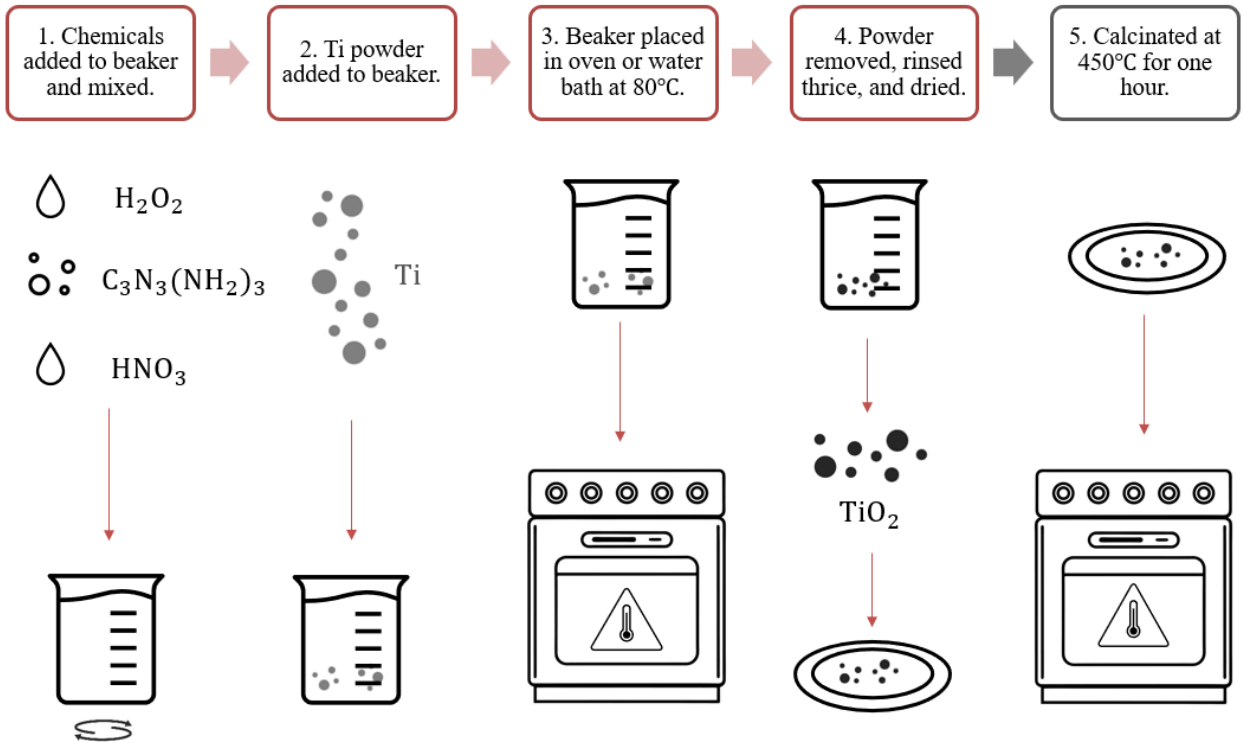


**Figure 5.5: Experimental powder procedure broken down by steps. 1. Combine $H_2O_2$, $C_3N_3(NH_2)_3$, and $HNO_3$ and ultrasonically mix. 2. Add CP-Ti powder. 3. Place in either the oven or water bath at 80 ℃ for experiment duration. 4. Remove powder from chemical bath, rinse thrice with deionized water and let air dry. 5. Select experiments were calcinated 450 ℃ for one hour.**

Experiments P-#a and b were of the same powder vial and chemical bath with variation in if they were calcinated at 450 ℃ for one hour. Experiment durations, heating equipment, if calcinated, and if vacuum sealed are outlined in Table 5.4.

**Table 5.4: Powder experiments completed in $H_2O_2$, $HNO_3$, and $C_3N_3(NH_2)_3$ bath.**

| Batch | Duration (hours) | Heating Equipment | Calcinated | Vacuum Sealed Powder |
|---|---|---|---|---|
| **P-6** | 24 | Water bath | No | Yes |
| **P-7a** | 12 | Water bath | No | Yes |
| **P-7b** | 12 | Water bath | Yes | Yes |
| **P-8a** | 12 | Oven | No | Yes |
| **P-8b** | 12 | Oven | Yes | Yes |
| **P-9a** | 12 | Oven | No | No |
| **P-9b** | 12 | Oven | Yes | No |
| **P-10a** | 12 | Oven | No | Yes |
| **P-10b** | 12 | Oven | Yes | Yes |
| **P-11a** | 12 | Oven | No | No |
| **P-11b** | 12 | Oven | Yes | No |
| **P-12a** | 12 | Oven | No | Yes |
| **P-12b** | 12 | Oven | Yes | Yes |
| **P-13a** | 12 | Oven | No | No |
| **P-13b** | 12 | Oven | Yes | No |
| **P-14** | 12 | Oven | Yes | No |

The chemical amounts used for every experiment are outlined in Table 5.5. Experiments were scaled up by two for P-9a to P-14.

**Table 5.5: Chemical amounts used in $H_2O_2$, $HNO_3$, and $C_3N_3(NH_2)_3$ bath.**

| Batch | CP-Ti (mg) | $H_2O_2$ (mL) | $HNO_3$ (mL) | $C_3N_3(NH_2)_3$ (mg) |
|---|---|---|---|---|
| **P-6** | 50 | 50 | 1 | 6 |
| **P-7a & P-7b** | 50 | 50 | 1 | 6 |
| **P-8a & P-8b** | 50 | 50 | 1 | 6 |
| **P-9a & P-9b** | 100 | 100 | 2 | 12 |
| **P-10a & P-10b** | 100 | 100 | 2 | 12 |
| **P-11a & P-11b** | 100 | 100 | 2 | 12 |
| **P-12a & P-12b** | 100 | 100 | 2 | 12 |
| **P-13a & P-13b** | 100 | 50 | 2 | 12 |
| **P-14** | 100 | 100 | 2 | 12 |

Once the chemicals were combined, they were ultrasonically mixed until the melamine powder had fully dissolved. This typically took 5-10 minutes as the melamine would clump together. The

powder was added once the chemical bath was uniform in appearance (Figure 5.6). All experiments completed with the updated chemical bath were cold starts.

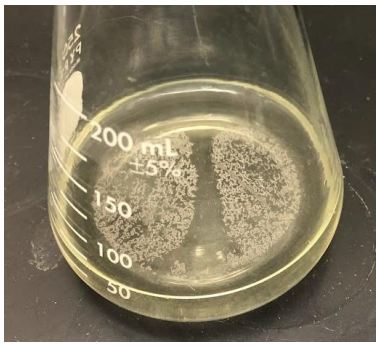


**Figure 5.6: P-6, CP-Ti powder added to flask containing ultrasonically mixed chemical bath.**

The procedure was scaled up to produce more powder. The chemical specifications and amounts are outlined in Table 5.6.

**Table 5.6: Chemical specifications and amounts used in scaled up $H_2O_2$, $HNO_3$, and $C_3N_3(NH_2)_3$ bath.**

| Chemical | Annotation | Supplier | Concentration | Amount Used |
|---|---|---|---|---|
| **Titanium powder** | Ti | AP&C | - | 1 g |
| **Hydrogen peroxide** | $H_2O_2$ | Fischer Scientific | 30 wt % | 1000 mL |
| **Nitric acid** | $HNO_3$ | Fischer Scientific | 68-70 wt % | 20 mL |
| **Melamine** | $C_3N_3(NH_2)_3$ | Fischer Scientific | 99 % | 120 mg |

Experiments were completed on powders for 6, 8, and 12 hours to compare the differences in apparent nanostructural growth. The start temperature, duration, heating method, and if calcinated at 450 ℃ for 1 hour are outlined in Table 5.7.

**Table 5.7: Scaled up powder experiments completed in $H_2O_2$, $HNO_3$, and $C_3N_3(NH_2)_3$ bath.**

| Batch | Start | Duration (hours) | Heating Equipment | Calcinated |
|---|---|---|---|---|
| **P-15** | Cold | 12 | Oven | Yes |
| **P-16a** | Cold | 6 | Oven | No |
| **P-16b** | Cold | 6 | Oven | Yes |
| **P-17a** | Cold | 8 | Oven | No |
| **P-17b** | Cold | 8 | Oven | Yes |

## 5.2 Microstructure Analysis

### *5.2.1 Hydrogen Peroxide Chemical Bath*

Upon removal from the water bath, the $H_2O_2$ bath was clear with white precipitates floating throughout (Figure 5.7). Literature noted that white precipitates could form in an $H_2O_2$ bath with Ti [92].

**Figure 5.7: Batch P-1 after removal from water bath.**

The powder did not change colour after the $H_2O_2$ bath but the powder particles did aggregate to each other creating flake-like appearance after thrice rinsed with deionized water (Figure 5.8).

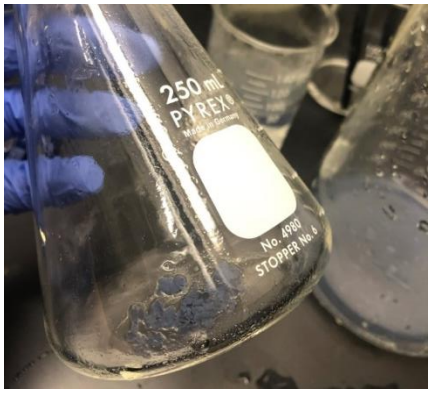


**Figure 5.8: Batch P-1 after three rinses in deionized water.**

Upon drying, the powder particles appeared to separate and be a darker grey than the original Ti powder. The powder was adhered to the SEM holder with thin double-sided tape and gold sputtered. P-1 did not present signs of desired nanostructural growth when compared to literature at the same magnifications (Figure 2.7). Instead, P-1 had brittle flaky layers of amalgamated spherical CP-Ti particles with cracks throughout (Figure 5.9 a), b) and c)). Some porous characteristics could be seen at higher magnifications but overall, the layers appeared dense and brittle (Figure 5.9 d)).

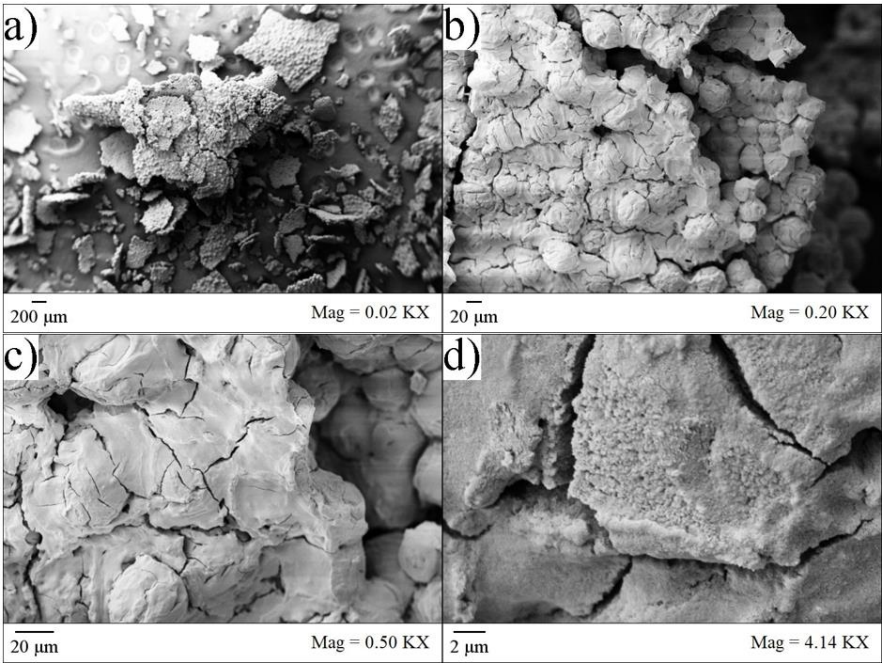


**Figure 5.9: SEM images of P-1 at a) 0.02 KX, b) 0.20 KX, c) 0.50 KX, and d) 4.14 KX completed in $H_2O_2$ and water bath with a hot start. Powder amalgamated together and showed low apparent porosity.**

P-2 and P-3 were conducted at the same time with P-2 in the water bath and P-3 in the oven. P-2 was conducted identical to P-1 apart from a cold start. P-3 had a concave glass cover placed on top for $H_2O_2$ retention. P-3 did not have any liquid $H_2O_2$ left in the beaker by the end of the 72 hours, confirming the concave glass beaker cover was not sufficient in liquid retention (Figure 5.10).

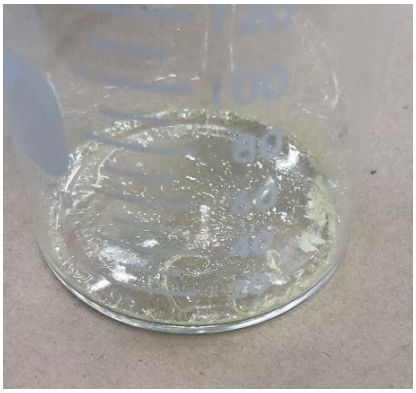

**Figure 5.10: P-3 at the end of 72-hour oven experiment.**

SEM imaging was completed on P-2 and P-3 together. It was expected to not see much, if any, growth on P-3 as the liquid had evaporated and was not available to the powder to react. P-2 presented similar results to P-1 showing the growth around the particles (Figure 5.11 a)) with low apparent porosity (Figure 5.11 b)). Although P-1 had more amalgamation into flaky layers, whereas P-2 did not form layers amongst the individual powder particles. The difference in

experimental procedure was that P-1 had a hot start where the $H_2O_2$ was brought up to temperature before the Ti powder addition. The temperature shock caused the particles to adhere together, which was not seen when the powder was heated up with the $H_2O_2$. P-3 powder particles remained smooth which was due to the $H_2O_2$ loss by evaporation and no growth was observed (Figure 5.11 c) and d)).

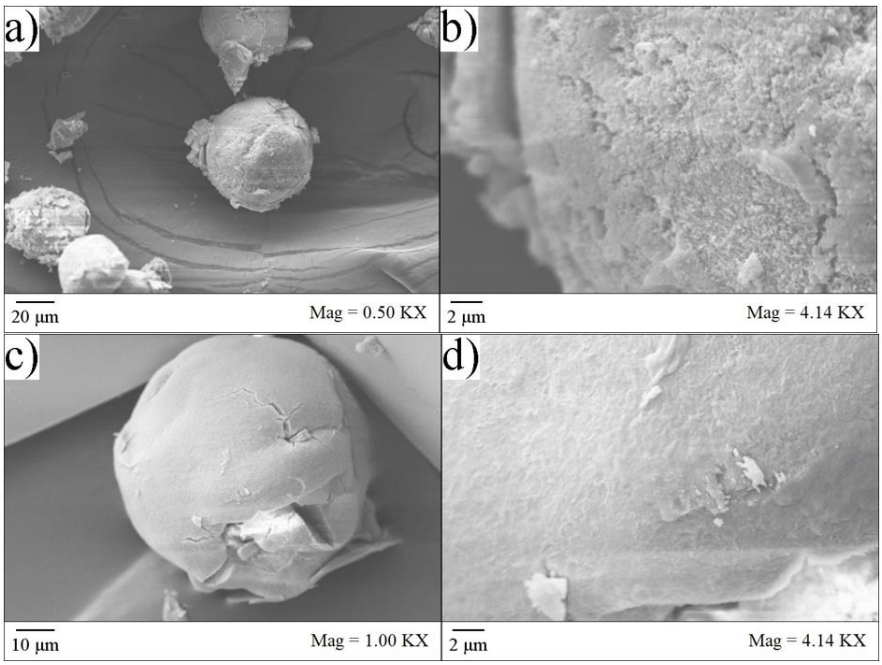


**Figure 5.11: SEM images of P-2 at a) 0.50 KX and b) 4.14 KX completed in the water bath. Powder did not amalgamate together and showed low apparent porosity. SEM images of P-3 at c) 1.00 KX and d) 4.14 KX completed in the oven. Complete $H_2O_2$ evaporation occurred, and powder surface remained smooth.**

P-4 was conducted identical to P-2 in the water bath with a cold start. A 500 mL flask beaker was used for P-5 with a cold start, and the flask stopper was reused from early experiments in section 4.1.2. This yielded better $H_2O_2$ retention with white precipitates forming (Figure 5.12). As a larger flask was used, the dosages were also doubled; 200 mg of powder was placed in 200 mL of $H_2O_2$ to gauge if scaling up the experiment impacted results.

**Figure 5.12: P-5 at beginning and end of 72-hour oven experiment showing successful $H_2O_2$ retention.**

The $H_2O_2$ levels were maintained over 72 hours in both P-4 and P-5 experiments with white precipitates developing (Figure 5.13).

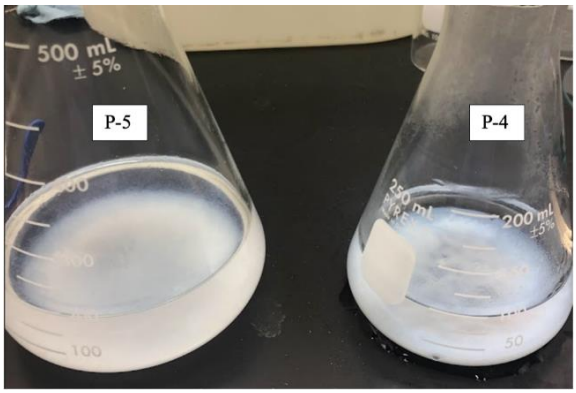


**Figure 5.13: P-4 and P-5 at the end of 72-hour experiments.**

P-4 produced similar results to P-1 and P-2 with flakes and rough surfaces along the Ti powder particles. There was clear growth, but no clear nanostructural growth (Figure 5.14 a) and b)). P-5 was also alike to previous experiments with rough surface texture along the powder particles (Figure 5.14 c) and d)). Undesirable plate and powder results prompted re-evaluation of chemical bath methodology, and the experimental procedure was adjusted.

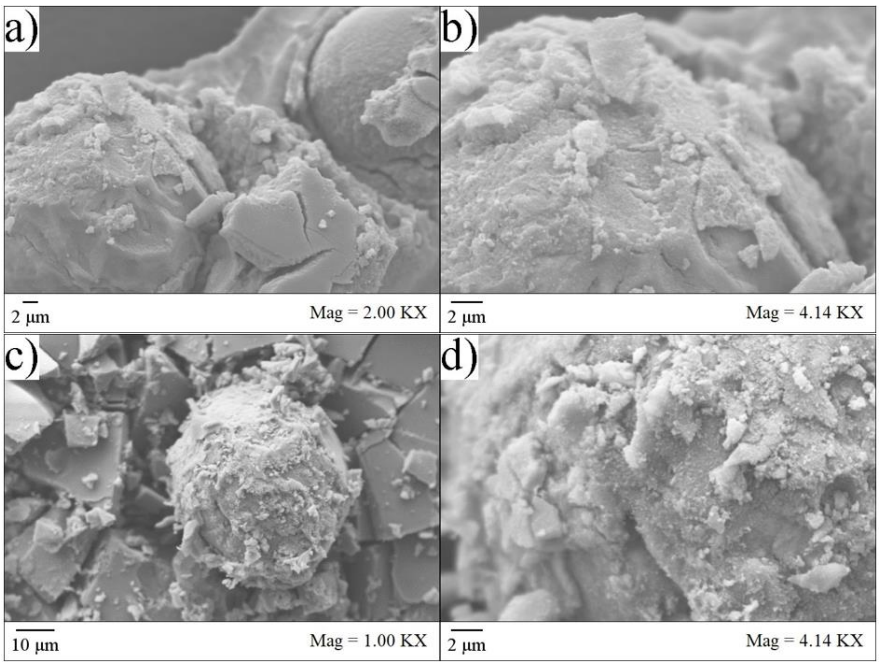


**Figure 5.14: SEM images of P-4 at a) 2.00 KX and b) 4.14 KX completed in the water bath. Powder had growths, but low apparent porosity. SEM images of P-5 at c) 1.00 KX and d) 4.14 KX completed in the oven. Efficient $H_2O_2$ retention resulted in more growths, but with low apparent porosity.**

### *5.2.2 Hydrogen Peroxide, Nitric Acid, & Melamine Chemical Bath*

P-6 was the first powder experiment completed with the new chemical bath composition. Vacuum sealed powder was placed into the chemical bath for 24 hours in the water bath. By the end of the duration the chemical bath turned a deep yellow, and the powder was a dark grey (Figure 5.15).

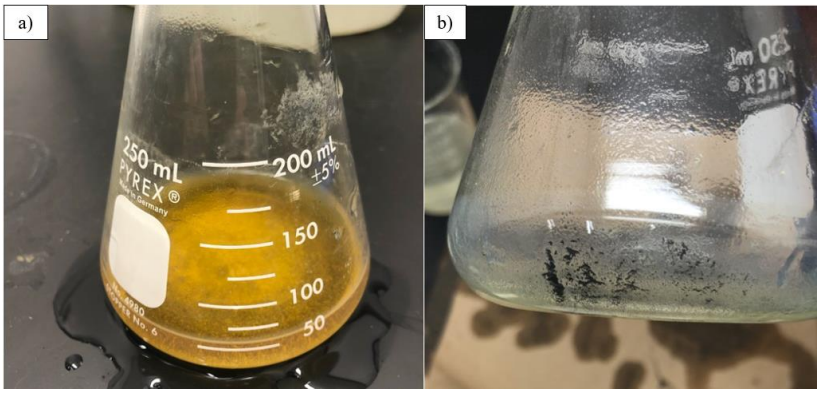


**Figure 5.15: P-6 upon a) removal from water bath and b) after rinsing with deionized water.**

SEM images of P-6 showed the continuation of cold starts prevented powder aggregation (Figure 5.16 a)). It exhibited smooth spherical shell growth with rivets running throughout (Figure 5.16 b) and c)). Clear nanostructural growth was not present with a smooth surface and low apparent

porosity and SSA (Figure 5.16 d)). These results were the first instance of seeing cracking throughout the Ti shell itself. The shells appeared dense with low surface areas.

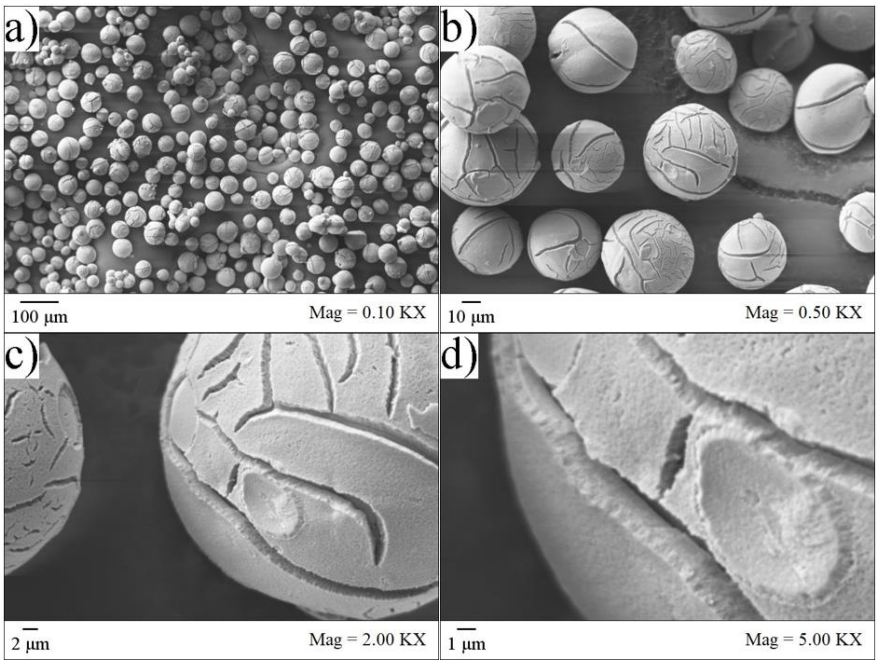


**Figure 5.16: SEM images of P-6 at a) 0.10 KX, b) 0.50 KX, c) 2.00 KX, and d) 5.00 KX as the first powder experiment completed with new chemical bath of $H_2O_2$, $HNO_3$, and $C_3N_3(NH_2)_3$ in water bath and not calcinated. Powder had growths with cracking and smooth surface.**

P-7 and P-8 were conducted at the same time with P-7 using the water bath and P-8 using the oven. Both had good liquid retention and were cloudy and yellow-orange in colour (Figure 5.17).

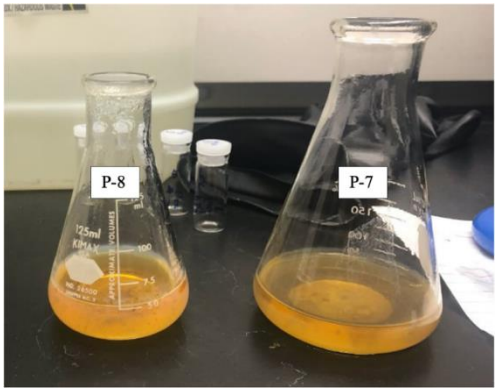


**Figure 5.17: P-7 and P-8 after removal from heat sources.**

P-7 and P-8 powders were each separated into two batches, un-calcinated (a) and calcinated at 450 °C for 1 hour (b). P-7a had a smooth shell with no crack formations like seen in P-6 (Figure 5.18 a)). There was minor porosity, but still low in apparent surface area from lack of porous growth (Figure 5.18 b)). P-7b presented minor cracks, potentially from the calcination process heat (Figure

5.18 c)). There was increased surface texture and slightly more porosity than in P-7a (Figure 5.18 d)).

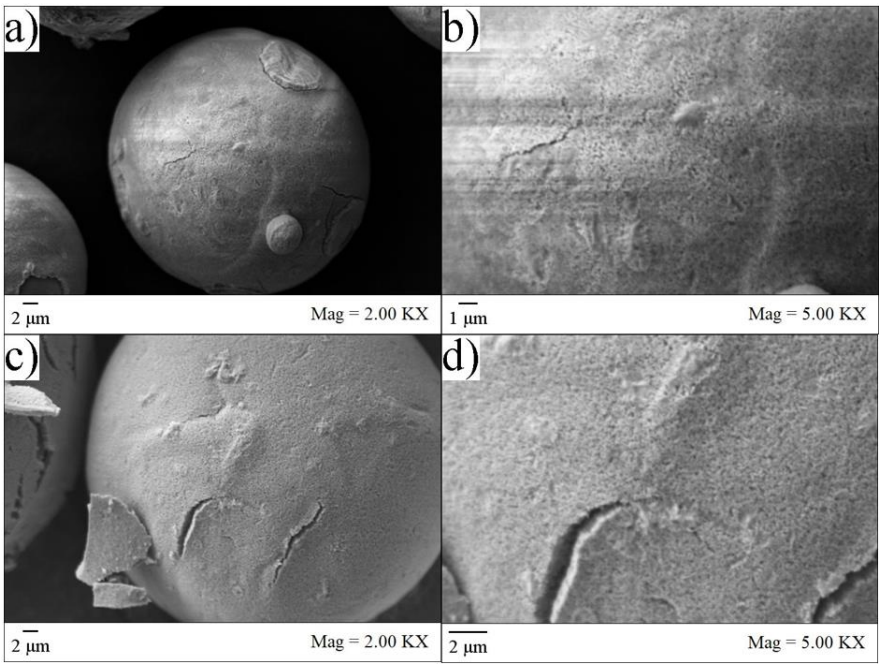


**Figure 5.18: SEM images of P-7a: not calcinated at a) 2.00 KX and b) 5.00 KX. Smooth surface with slight porosity. SEM images of P-7b: calcinated at c) 2.00 KX and d) 5.00 KX. Cracking with slightly increased apparent porosity.**

P-8a was comparable to P-7a in appearance, with smooth surfaces (Figure 5.19 a)) and minor porosity along the shells (Figure 5.19 b)). P-8b had the most promising powder results with nanostructural growth and increased porosity following calcination (Figure 5.19 c)). The nanostructural growth resembled nanorods with spike formations and some spiky cluster deposits, resembling nanoflowers, along the powder particles (Figure 5.19 d)).

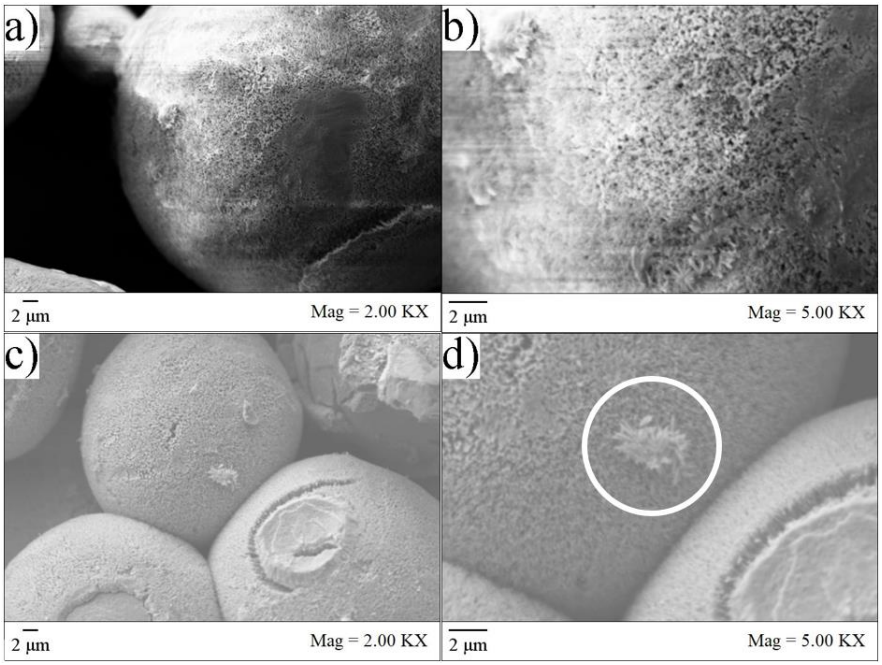


**Figure 5.19: SEM images of P-8a: not calcinated at a) 2.00 KX and b) 5.00 KX. Smooth surface with slight porosity. SEM images of P-8b: calcinated at c) 2.00 KX and d) 5.00 KX with nanoflowers highlighted. Increased porosity and nanostructural growth following calcination.**

The $HNO_3$ that had been used for experiments was found in the chemical storage of the uOttawa Cold Spray Lab. It did not have a visible expiration date on the bottle. As it was the only chemical not purchased for these experiments and the purchase / expiration date could not be confirmed, a new bottle was purchased. All experiments onward (P-9 and all subsequent powder experiments) were conducted with the new $HNO_3$ purchased from Fischer Scientific.

P-9 and P-10 were conducted at the same time. P-9 powder was opened and let sit before being added to the chemical bath, whereas the powder was immediately added to P-10. The objective of this was the see if oxidation was a concern with the powder and if it affected the results. Similar methodology was completed on the plates with polishing before immediate or delayed chemical submersion and no change in results was noted. Both beakers were placed together in the oven with thin plastic film on top to avoid evaporation (Figure 5.20).

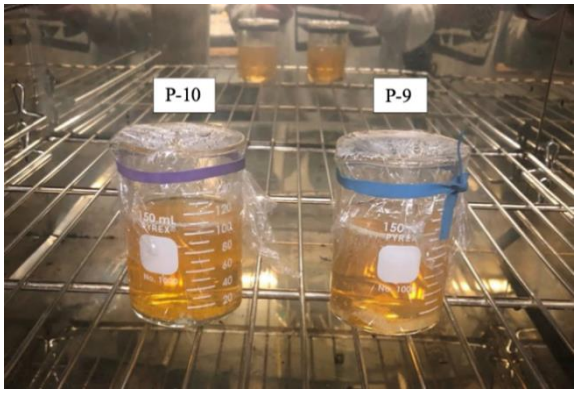


**Figure 5.20: P-9 and P-10 after 12 hours in oven.**

The results with the new $HNO_3$ produced more growth with clear nanostructural rods ending in spikes. This confirmed that a prominent error in previous experiments was the usage of old $HNO_3$ which had likely decreased in potency over time. The efficacy of $HNO_3$ increases acidity, decreases the pH level, and promotes anatase-rutile growth. As a result, expected growth was not previously achieved on the Ti powder because the chemical bath was not at a pH level that facilitated effective anatase and rutile formations. Anatase growth is cultivated in more alkaline conditions with higher pH levels, the growths seen in previous experiments reasonably possessed minimal anatase growth with low surface area.

P-9a showed high porosity in spongelike appearance with increased nanoflowers spanning the powders surfaces (Figure 5.21 a) and b)). The nanostructures were interconnected in a web-like system (Figure 5.21 c) and d)). It had increased SSA which would support numerous points of contact for ROS reactions and pollutant degradation.

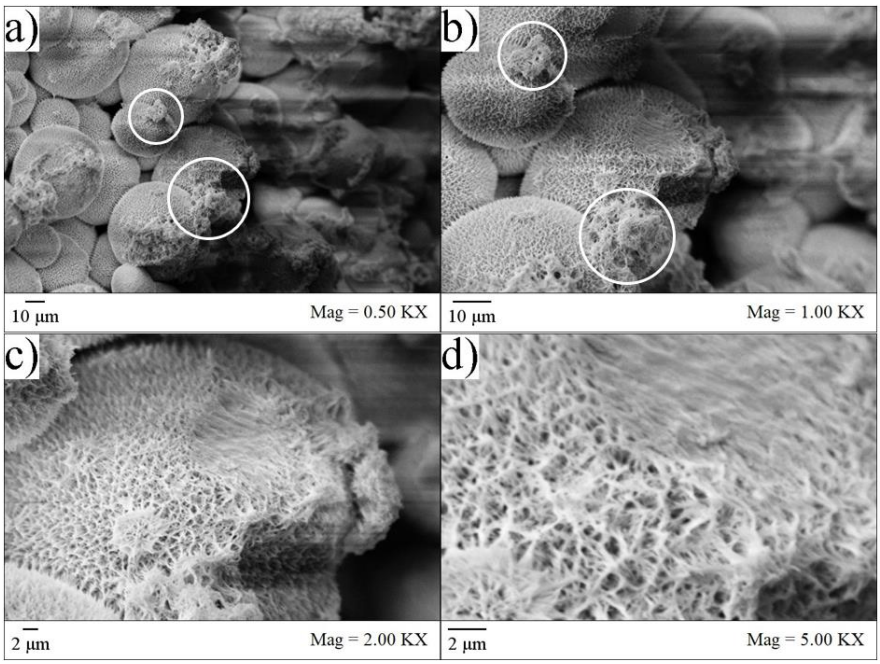


**Figure 5.21: SEM images of P-9a: not calcinated, which was the first experiment completed with the new $HNO_3$, at a) 0.50 KX, b) 1.00 KX c) 2.00 KX and d) 5.00 KX. Powder had clear nanostructural growth of sponge-like connected networks with nanoflowers (highlighted).**

Calcination at 450 ℃ for 1 hour was completed with the intent of deconstructing hydrogen titanate nanowires and improving the crystallinity of anatase structures (Figure 5.22 a)) with the presence of nanoflowers maintained (Figure 5.22 b)). P-9b, which was powder from the same experimental batch at P-9a except calcinated, had deconstructed the web-like interconnected system into nanorods that grew to points at the end, providing a spiky look in appearance (Figure 5.22 c) and d)).

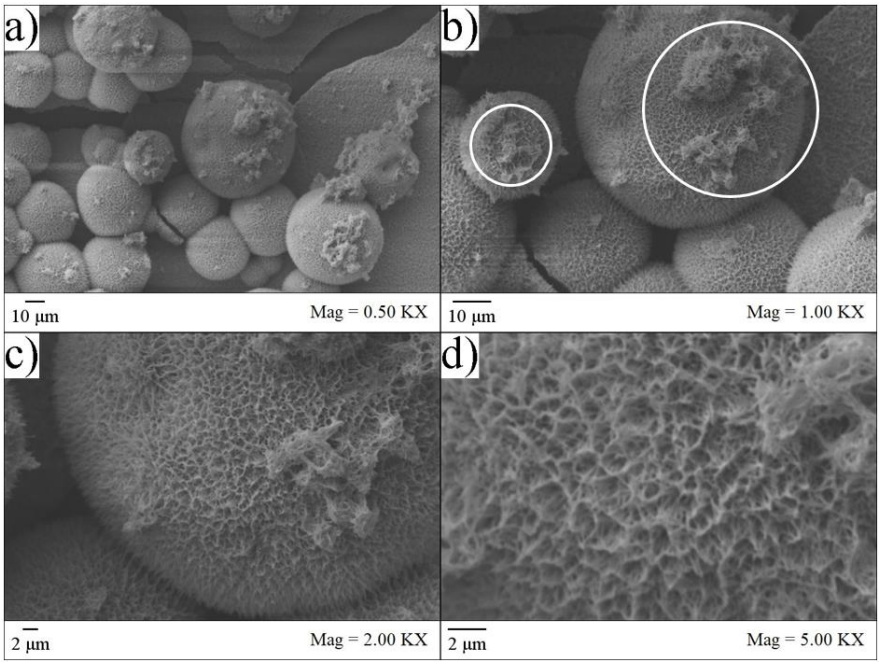


**Figure 5.22: SEM images of P-9b: calcinated at a) 0.50 KX, b) 1.00 KX highlighting nanoflowers, c) 2.00 KX and d) 5.00 KX. Powder had deconstructed the interconnected network to spiked nanorods.**

There was also the presence of titania aggregates along the surface in P-9 powder, which resembled flower-like nanostructures seen in studies (Figure 5.23). Within the studies it was noted that nanoflower aggregates were typically seen to only exist along the top layers of titania. It is remarked that the nanoflowers growth patterns were affected by the $HNO_3$ concentration [95], [99], [100]. This aligns with observable nanoflower aggregates forming in powder experiments that used effective $HNO_3$.

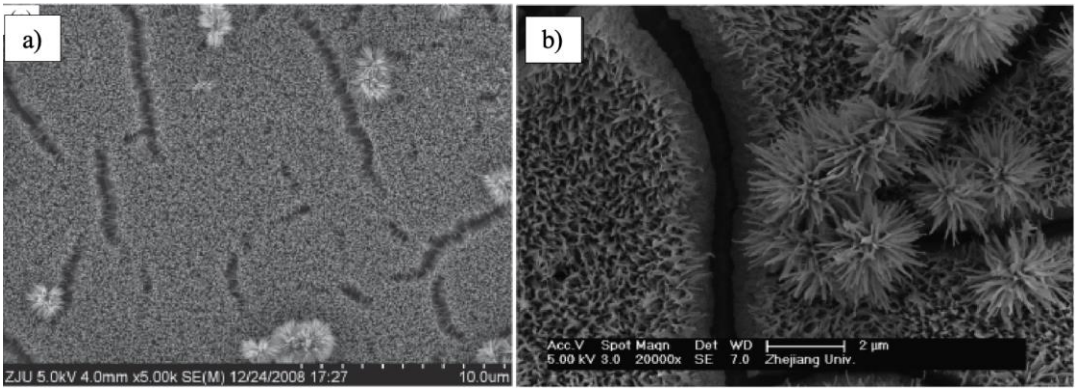


**Figure 5.23: Nanoflowers from reference literature a)[100] and b) [95].**

P-10a exhibited different results than those seen in P-9a with the particles appearing to have more strongly attached together (Figure 5.24 a)). It presented less visible porosity with smaller nanorods and areas that had low-profile rough surfaces (Figure 5.24 b)). It also lacked the web-like spongy

texture that P-9a had. Spiked nanorods were still present and it was considered that the SEM images were taken on a location that was pressed against the beaker which could have potentially produced a flatter surface. This was speculated because the flatter areas are seen on the most outward presenting surfaces with the nanorod structures seen in the portions between powder particles. P-10b had growths extended to spikes and while there were fewer flat areas, they were still present (Figure 5.24 c)). It presented similar results to P-9b with strong formations of nanorods following calcination at 450 ℃ for one hour (Figure 5.24 d)). P-9b and P-10b presented the most promising results thus far closely resembling reference literature SEM images developing $TiO_2$ shells on Ti powders (Figure 2.7). There were not notable differences between P-9 and P-10 regarding adding the Ti powder either immediately or delayed to the bath upon being unsealed.

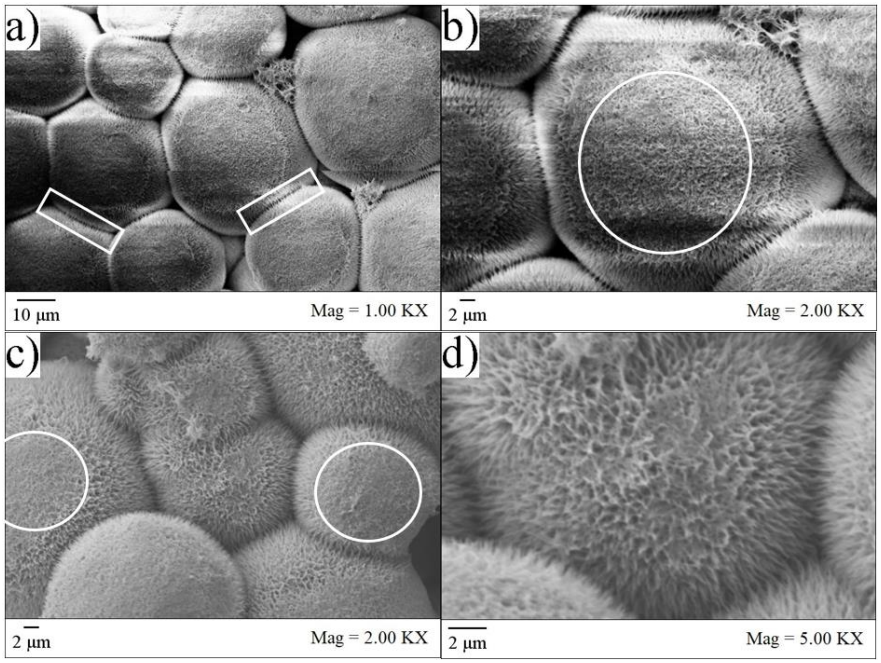


**Figure 5.24: SEM images of P-10a: not calcinated at a) 1.00 KX highlighting particle adhesion and b) 2.00 KX highlighting flat surfaces. Powder had nanostructural growth with many flat areas. SEM images of P-10b: calcinated at c) 2.00 KX highlighting flat surfaces and d) 5.00 KX. Nanostructural growth improved and nanorod growth became more defined.**

P-11, P-12, and P-13 were conducted at the same time. P-11 was completed like P-9 with the powder being open prior to the experiment. P-12 was conducted like P-10 with the powder being added immediately after being unsealed. The previous experiments were repeated to verify result consistencies. P-13 was conducted with half the amount of $H_2O_2$ to see how the shell growth was

affected. All the experiments had the powder separated following the oven, rinsing and drying, and half was calcinated. A thin plastic film was used again to avoid liquid loss (Figure 5.25).

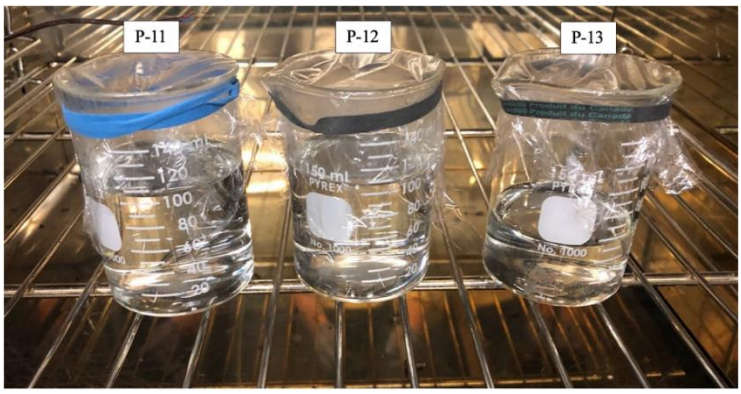


**Figure 5.25: P-11, P-12, and P-13 initially placed in oven before experiment duration.**

P-11a had similar results to those previously seen with nanorods throughout and areas with flat surfaces (Figure 5.26 a)). After calcination at 450 ℃ for one hour, P-11b had distinguished nanorods, but still had the areas with smoother surfaces present (Figure 5.26 b)). P-12a, like P-10a, had nanorods between particles with flatter areas along the outermost parts of the particles (Figure 5.26 c)). P-12b had more defined nanostructural growth than that seen in P-12a. Like P-10b, the flat areas on the surface seemed to minimize following calcination and the nanorods appeared more defined (Figure 5.26 d)).

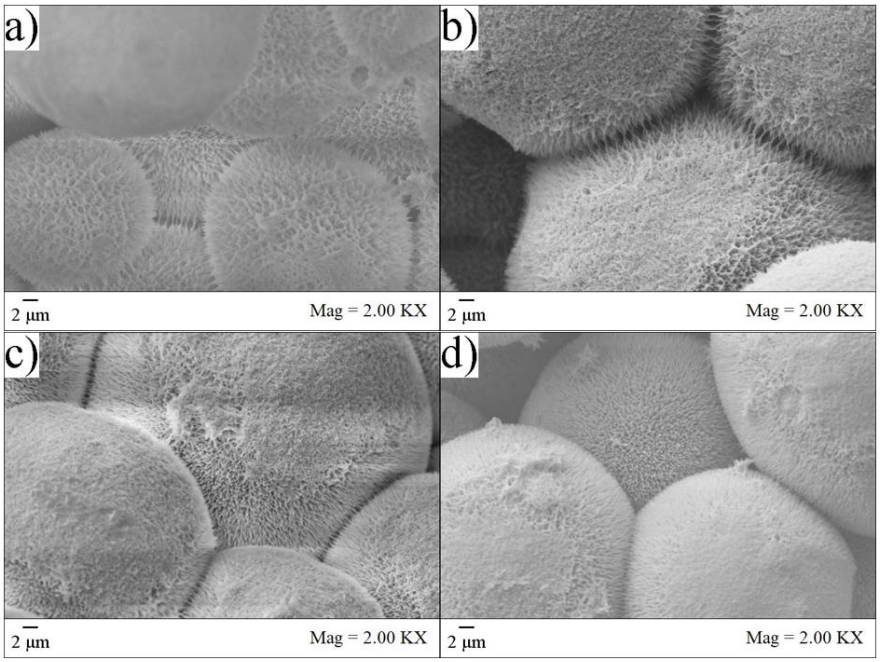


**Figure 5.26: SEM images at 2.00 KX of a) P-11a: not calcinated, b) P-11b: calcinated, c) P-12a: not calcinated d) P-12b: calcinated. Growths exhibited improved crystallinity following calcination.**

P-11b and P12b verified the results found in P-9b and P-10b powder batches with defined nanorod growths that grew to spiked tips. Better SEM images of nano formations were seen in the calcinated batches, substantiating that the addition of calcination at 450 ℃ for 1 hour did strengthen the crystallinity of the $TiO_2$ shell. Furthermore, discrepancies in results were not seen when comparing the oxidized vs. non-oxidized powders, concluding that the powder being exposed to air for extended periods of time before chemical bath submersion did not alter the nanostructural growths. Powders prepared in the oven yielded successful growths indicating that a water bath was not required for circulating heated water opposed to air as a heating source.

Reducing the amount of $H_2O_2$ had the expected effect of reducing the nanostructural growths on the Ti powder particles (Figure 5.27 a)). There were still nanorod formations that grew to spiked ends, but they did appear smaller in size than other powder batches with lower visible porosity (Figure 5.27 b)). After calcinating P-13 powder at 450 ℃ for 1 hour, flat areas like previously seen were noted again (Figure 5.27 c)). Calcinating P-13 powder at 450 ℃ for 1 hour did increase porosity and define the nanorods which did continue to appear shallower than the experiments with twice the amount of $H_2O_2$ (Figure 5.27 d)).

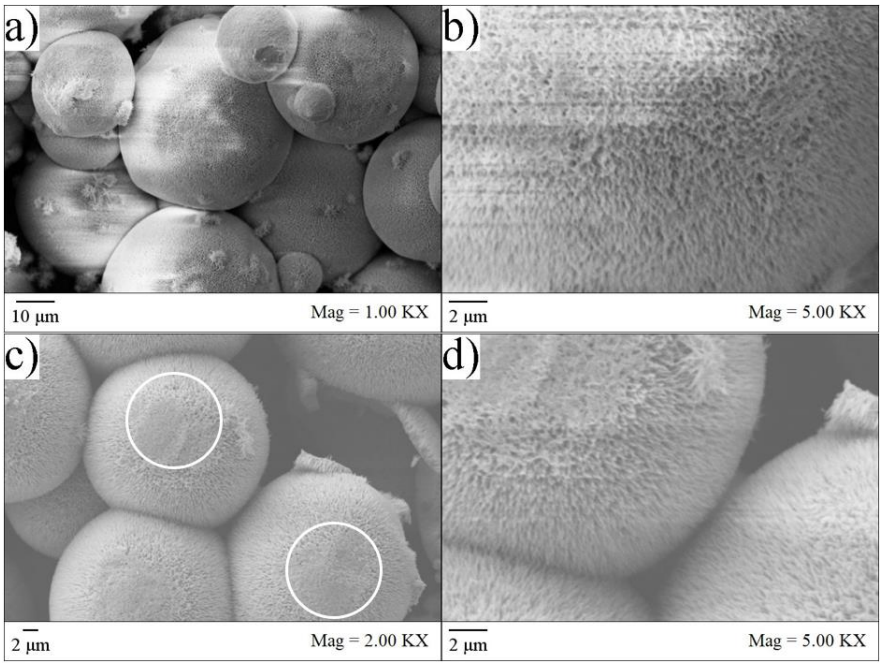


**Figure 5.27: SEM images of P-13a: half nitric acid and not calcinated at a) 1.00 KX and b) 5.00 KX. Less nanostructural growth than in previous experiments. SEM images of P-13b: half nitric acid and calcinated at c) 2.00 KX highlighting flat surfaces and d) 5.00 KX. Powder had more defined growth following calcination.**

P-14 was the first experiment using a polytetrafluoroethylene (PTFE) cover. PTFE was ordered specifically for the powder experiments to avoid potential cross contamination as the thin plastic film was already in the laboratory's inventory, like the initial $HNO_3$ used in the preliminary experiments prior to P-9. It was selected because of its durability, hydrophobicity, and temperature and chemical resistance. Its flexibility meant it could be secured with a band around the 150 mL beakers to minimize evaporation (Figure 5.28).


**Figure 5.28: Batch P-14 in oven prior to 12 hours with PTFE cover.**

The powder was opened prior to being added to the chemical bath and calcinated at 450 ℃ for 1 hour after the oven, rinsing, and air drying. P-14 had many tiny nanorods throughout the shells of

the powders with less flat areas (Figure 5.29 a)). Nanoflowers were also present (Figure 5.29 b) and c)). The nanorods appeared more densely placed that previously noted which could indicate higher SSA due to more spikes or lower SSA due to potentially less porosity in the shell (Figure 5.29 d)).

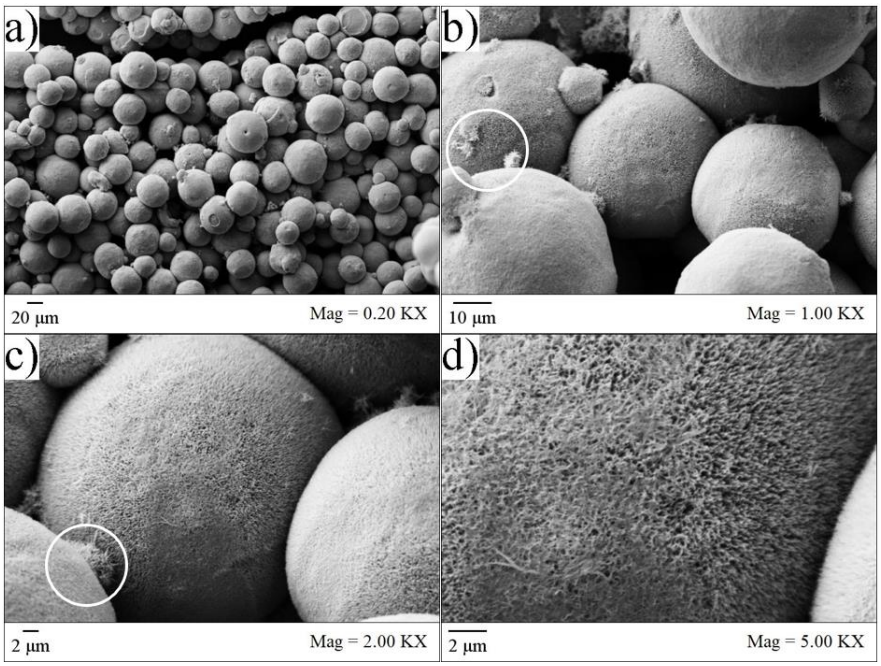


**Figure 5.29: SEM images of P-14: calcinated, which was the first experiment to use a PTFE cover, at a) 0.20 KX, b) 1.00 KX, c) 2.00 KX, d) 5.00 KX highlighting the presence of nanoflowers.**

In summary, the powder experiments P-9 to P-14 exhibited nanostructures on the CP-Ti powder that aligned with the literature after new nitric acid was introduced. Powder experiments prior to P-9 did not have the right chemical bath conditions, negatively impacting the pH level, to promote the growth of anatase and rutile nanostructures. Calcinated powder at 450 °C for 1 hour did present the most promising SEM images with defined nanorods that grew to pointed tips, spiked in appearance. Concluding that calcination did strengthen the crystallinity of the grown $TiO_2$ shells by decomposing the hydrogen titanate nanowires. There was no apparent difference in experiments completed in the water bath or the oven. Concluding that the heating method of circulating water or noncirculating air did not ultimately alter the heating of the chemical bath enough to negatively affect the results. Nor was there a notable difference in powders added immediately or left exposed to the air prior to being added to the chemical bath. Concluding that oxidation by exposure to air prior to chemical bath immersion did not negatively affect the results. Therefore, the heat transfer methods and potential surface oxidation did not present concerns in affecting the experimental

powder results. As a result, the experimental powder production could be scaled up in the oven as it could accommodate larger beakers than the water bath could accommodate larger flasks.

P-15 was the first scaled up experiment to produce more powder for nanostructural characterization and photocatalytic reactivity testing. The PTFE was continued to be used, and a metal clamp held it in place on the 1 L beaker. Its thickness and slight rigidity provided the structure necessary to be used with the metal bracket in the scaled-up experiments and create a strong seal to avoid evaporation loss. This was preferred as the metal bracket would slip down if used with the thin plastic film. The bath turned a yellow-orange colour and contained white precipitates, congruent with the smaller batch experiments (Figure 5.30).

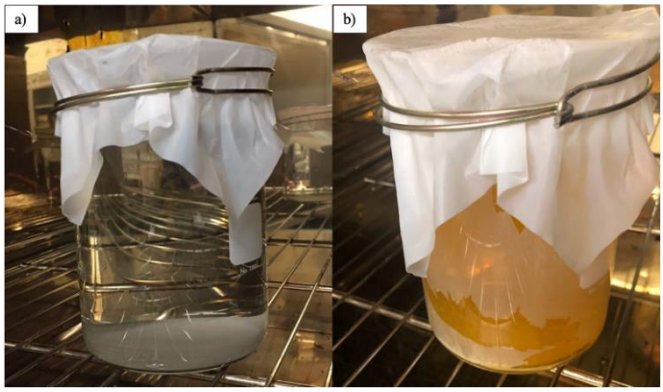


**Figure 5.30: P-15 at a) the beginning and b) end of 12-hour oven experiment.**

The powder was dark grey in appearance and the powder amalgamated into flakes following the chemical bath and retained their flakes after calcination. The flakes were delicate and slight aggravation or soft grinding resulted in powder particle separation (Figure 5.31).

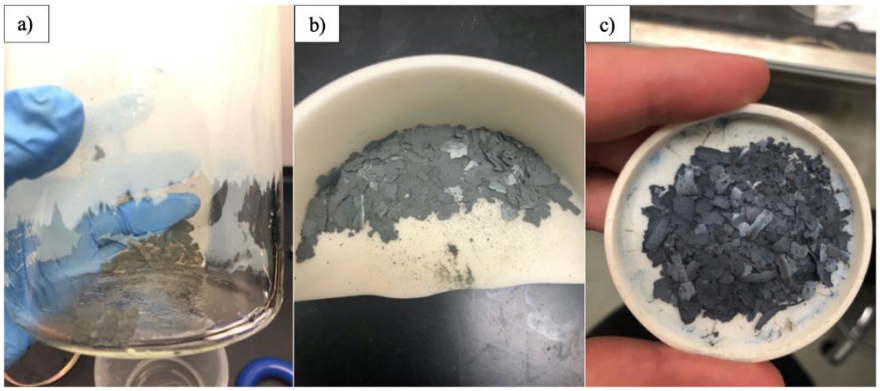


**Figure 5.31: P-15 a) after rinsing, b) air dried before calcination and c) after calcination.**

The powder was adhered to the sample holder with thin tape and gold sputtered prior to SEM imaging. SEM images were already acquired for 12-hour powder, but images of the flake's

formation were the objective. SEM images of P-15 targeting the flat flake portions revealed an almost flat uniform surface. The surface had a fibrous texture appearing that the nanostructural growth had fused together, consequently joining powder particles to each other and creating a flat base along the bottom of the beaker (Figure 5.32 a)). The powder particles at unjointed areas and facing upward produced results as seen previously with distinct spiked nanorods in calcinated 12-hour powders (Figure 5.32 b)).

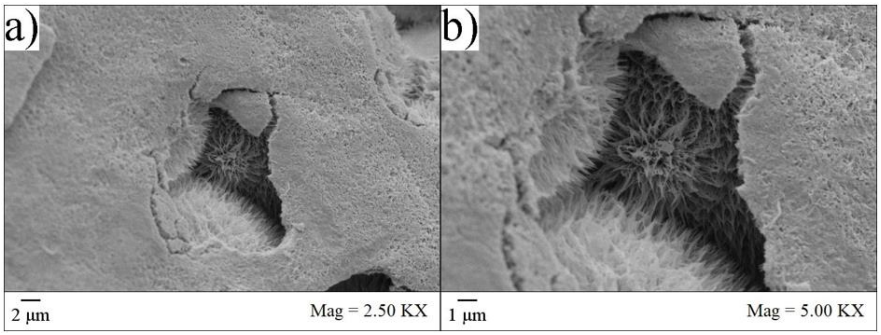


**Figure 5.32: SEM images of P-15: calcinated, which was the first experiment scaled up, at a) 2.50 KX showing the flat surface from agglomerated particles and b) 5.00 KX showing nanorod formations with spiked ends.**

Powder subjected to the chemical bath for 6 hours produced powders with minor nanostructural growth prior to calcination (Figure 5.33 a) and b)). The results were alike to P-13 which had half hydrogen peroxide. Upon calcination at 450 ℃ for one hour, the 6-hour powder had distinct nanostructural growth comparable to the 12-hour powders. It also had a strong presence of nanoflowers along the powder shells (Figure 5.33 c)). The crystallinity appeared to have significantly improve following calcination based on the SEM images (Figure 5.33 d)). P-16b was not like P-13b, which did not significantly improve following calcination.

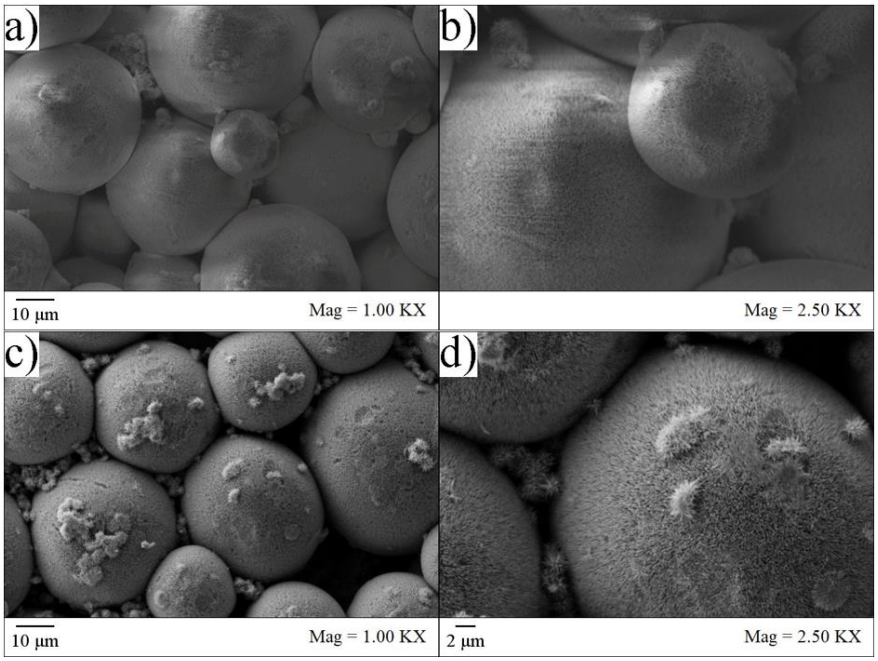


**Figure 5.33: SEM images of P-16a: not calcinated at a) 1.00 KX and b) 2.50 KX and P-16b: calcinated at c) 1.00 KX and d) 2.50 KX exhibiting more crystalline nanorods and nanoflowers after calcination.**

P-17a, which was subjected to the chemical bath for 8 hours, was similar to P-16a where there was nanostructural growth, but it appeared smaller and less defined than in the 12-hour powders (Figure 5.34 a) and b)). P-17b was similar in appearance to both P-16b and the 12-hour powders with spiked nanorods and nanoflowers on top (Figure 5.34 c) and d)).

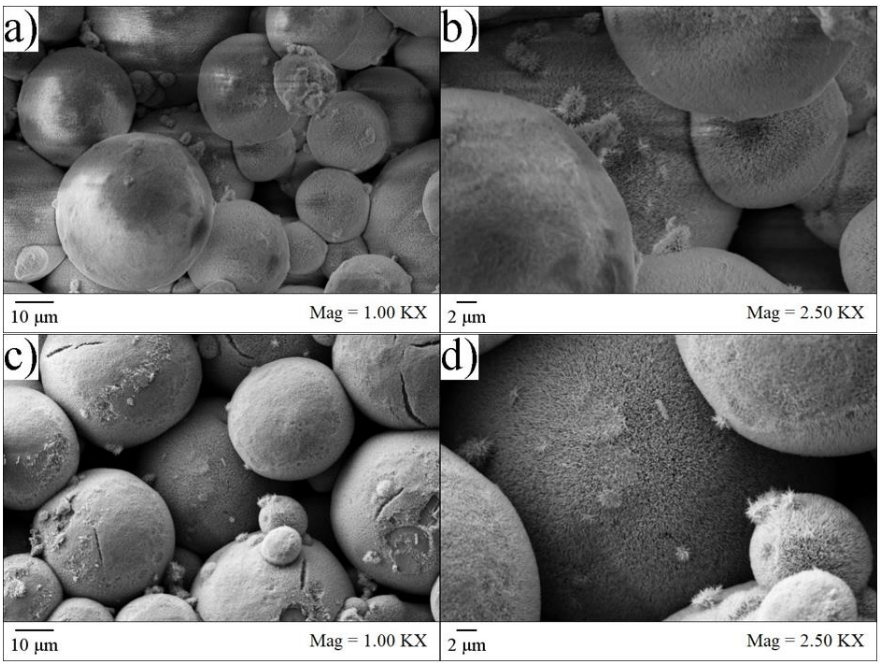


**Figure 5.34: SEM images of batches P-17a: not calcinated at a) 1.00 KX and b) 2.50 KX and P-17b: calcinated at c) 1.00 KX and d) 2.50 KX exhibiting more crystalline nanorods and nanoflowers after calcination.**

The addition of $HNO_3$, and $C_3N_3(NH_2)_3$ to the initial $H_2O_2$ chemical bath provided a pH environment that favoured more desirable growth of spiked nanorods with apparent high surface area for increased active sites for ROS generation. The chemical bath pH determines the phase and formations of $TiO_2$ synthesized. pH testing and experiments altering the chemical quantities and bath duration could produce more photocatalytically enhanced powder. The spiked nanorods appeared longer and more refined following calcination. It appeared that the chemical bath produced hydrogen titanate nanowires that increased in crystallinity following calcination [40], [56], [67], [191], [192]. Increasing calcination temperature or duration would affect crystallinity, crystallite size, and particle size with the ideal parameters for the photocatalytic reactivity dependent on the $TiO_2$ synthesis. Researchers have noted temperatures ranging from 450 to 650 ℃ and durations ranging from 1 to 4 hours produced the most promising results characterized by enhanced photocatalytic activity. Although the calcination parameters differed, the most optimal results carried the features of the highest anatase to rutile ratio, largest SSA, largest pore volume, and smallest k [6], [10], [11], [40], [48], [62], [104]–[109].

In conclusion, spiked nanorods were developed on CP-Ti powders through a chemical bath of $H_2O_2$, $HNO_3$, and $C_3N_3(NH_2)_3$ which were found more distinct in structure by SEM images

following calcination at 450 ℃ for 1 hour. It was concluded that utilizing a water bath or oven as a heating source produced identical results. It was also seen that exposing the powder to air for an extended time prior to chemical immersion did not influence the results. The powder production was successfully scaled up, and powders were developed for 6, 8, and 12 hours. There appeared to be smaller nanorods on the 6- and 8-hour powders prior to calcination, but afterwards they were very similar to the 12-hour powder SEM images.

## 5.3 X-Ray Diffraction Analysis

### *5.3.1 Methodology*

XRD was utilized to confirm if the desired $TiO_2$ nanostructures, anatase and rutile, were present in the CP-Ti particle shells. Calcinated powders of 6- and 12- hours developed using a $H_2O_2$, $HNO_3$, and $C_3N_3(NH_2)_3$ bath following the methodology outlined in were analyzed. The most promising SEM images were seen on calcinated powders. As there was not a strong difference in the 6- and 12-hour powder SEM images, both were chosen to confirm if the time durations produced comparable results.

### *5.3.2 Results*

Diffraction peaks of rutile occur around 27.4°, 36.0°, 41.2°, 44.0°, 54.3°, 56.6°, 62.7° and 69.0° which correspond to the crystal planes of rutile (110), (101), (111), (210), (211), (220), (002), and (301) respectively. Diffraction peaks of anatase occur around 25.3°, 37.8°, 48.1°, 53.9°, 55.1°, and 70.3° which correspond to the crystal planes (101), (004), (200), (105), (211), and (220), respectively [47], [59]–[61], [104], [106], [181]. 6-hour and 12-hour XRD data was plotted and compared to XRD data markers for titanium (mp-46), rutile (mp-2657) and anatase (mp-390) nanostructures from The Materials Project database (Figure 5.35) [182], [193]–[284]. Both graphs had their largest peaks coinciding with Ti, followed predominantly by anatase peaks, and less rutile peaks.

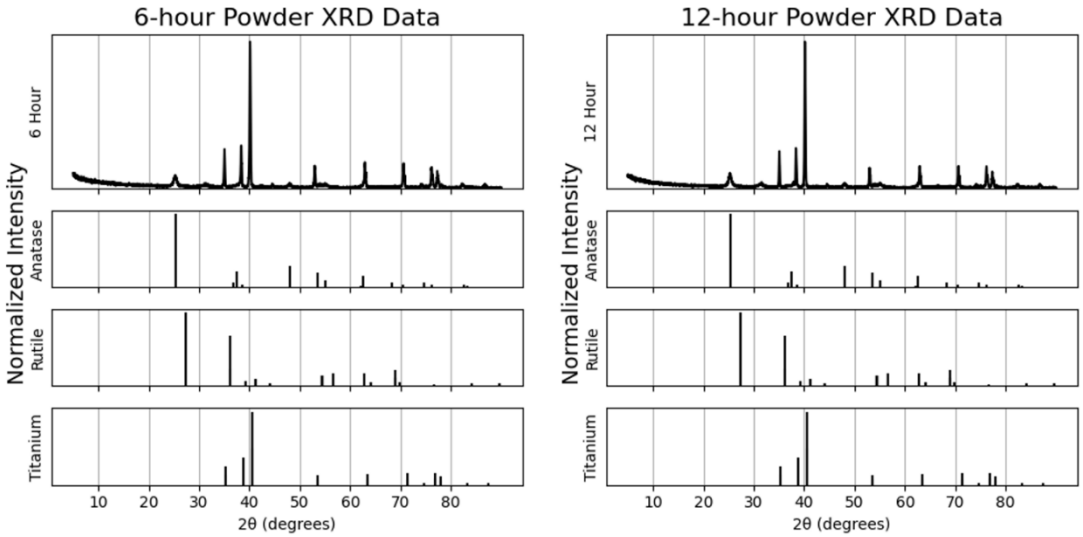


**Figure 5.35: 6- and 12-hour powder XRD graphs with Ti, anatase and rutile for reference.**

Highlighted in Table 5.8, peaks around 35°, 38°, and 40° coincide with Ti. Strong peaks around 25°and 53° align with anatase and the crystal planes of (101) and (105), with smaller peaks coinciding with additional crystal planes. Rutile had two peaks around 44° and 63° of the (210) and (002) planes. The results indicate stronger anatase over rutile growth in multiple crystal dimensions. Predominant growth in the one-dimensional plane for each structure is expected as the SEM images indicated nanorod growth, a one-dimensional structure.

**Table 5.8: XRD peaks with indicated structure and crystal plane for 6- and 12-hour powders.**

| 6-hour Powder Peak (°) | 12-hour Powder Peak (°) | Indicated Structure | Crystal Plane |
|---|---|---|---|
| 25.56 | 25.38 | Anatase | 101 |
| 35.04 | 35.06 | Titanium | 110 |
| 38.34 | 38.40 | Titanium | 101 |
| 40.12 | 40.16 | Titanium | 101 |
| 44.52 | 44.42 | Rutile | 210 |
| 48.1 | 48.26 | Anatase | 200 |
| 52.98 | 53.04 | Anatase | 105 |
| 55.3 | 55.22 | Anatase | 211 |
| 62.88 | 62.9 | Rutile | 204 |

## 5.4 Raman Spectroscopy Analysis

### *5.4.1 Methodology*

Like XRD, the purpose of using Raman spectroscopy was to confirm the presence of the desired $TiO_2$ nanostructures, anatase and rutile. XRD was performed on whole powder particles to provide the composition at a surface layer. Raman was performed on cross sectional powder particles providing additional structural information from the core CP-TI particle through the thickness of the $TiO_2$ shell.

Challenges primarily faced were that loose powder samples could not effectively be subjected to Raman spectroscopy due to movement and that they could not conveniently provide a cross section due to small size. The 6- and 12-hour powder were placed in green resin and gently polished to create stable cross sections for analysis. Low (Figure 5.36 a) and b)) and high contrast (Figure 5.36 c) and d)) SEM images display a cross-sectional view of $TiO_2$ shells grown on CP-Ti powder with measured thickness ranging from $\sim 2.5$ µm to $\sim 2.7$ µm.

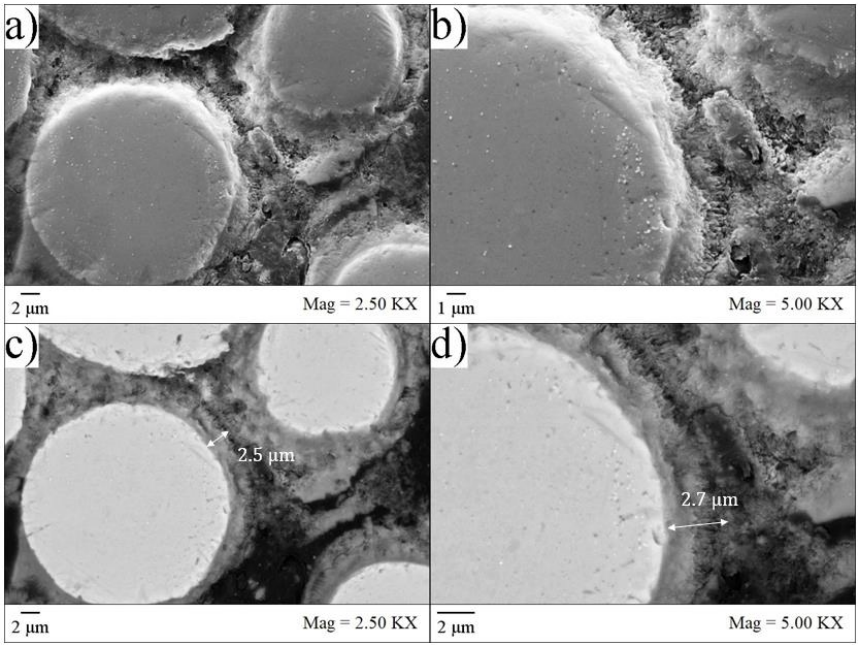


**Figure 5.36: SEM images of cross sectional 12-hour powder showing $TiO_2$ shell on CP-Ti powder for Raman analysis at low contrast a) 2.50 KX and b) 5.00 KX and high contrast c) 2.50 KX and d) 5.00 KX with thickness measurements.**

Successful analysis was completed on the cross sections of the powder placed in resin, and crystallinity was able to be determined and verified. High resolution Raman maps were made that highlighted two regions within the $TiO_2$ shell:

- Proximal Region (PR) was along the inner $TiO_2$ shell and closest to the CP-Ti particle core.
- Distal Region (DR) was along the outer $TiO_2$ shell and farthest from the CP-Ti particle core.

Light microscopy images of the scanned regions, highlighted in yellow, for Raman spectroscopy is shown in Figure 5.37 with the PR and DR regions highlighted.

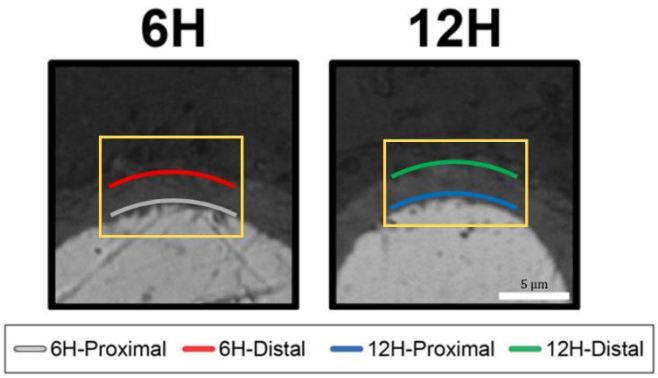


**Figure 5.37: LM images of cross sectional 6- and 12-hour powder. Scanned regions in yellow for Raman spectroscopy with PR and DR regions highlighted.**

### *5.4.2 Results*

Characteristic Raman bands for anatase and rutile forms were recognized in the spectral fingerprints for the 6- and 12-hour powders. The measured PR and DR vibration wavelengths from Raman scattering were compared to the active vibrational modes in the crystal structures of anatase and rutile with anatase possessing six ($A_{1g} + 2B_{1g} + 3E_g$) and rutile possessing four ($A_{1g} + B_{1g} + B_{2g} + E_g$) [285]–[287]. The active mode notations reference points and their symmetry in $TiO_2$ molecules for Raman characterization [288]–[291].

The plotted Raman spectra in Figure 5.38 have the following peaks which align with the known active modes at $B_{1g}$ at $402\ cm^{-1}$, $A_{1g}$ at $522\ cm^{-1}$, and $E_g$ at $640\ cm^{-1}$ in anatase and $E_g$ at $430\ cm^{-1}$ and $A_{1g}$ at $610\ cm^{-1}$ in rutile [37], [287], [292]. The strong anatase peaks and lack of rutile peaks in the PR regions (blue and grey) indicate primarily anatase structures on the inner part of the $TiO_2$ shell. Rutile peaks are present along with anatase peaks in the DR regions

(green and red), indicating a heterogenous crystal structure along the outer regions of the $TiO_2$ shell.

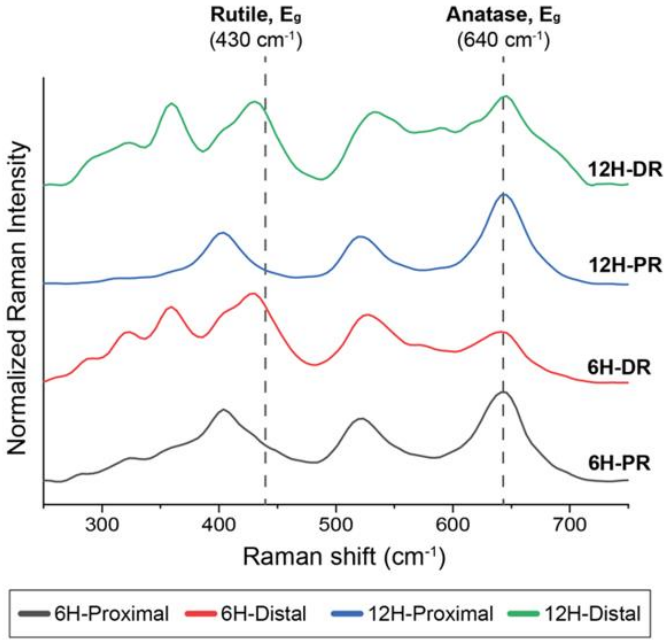


**Figure 5.38: Raman spectra of the PR and DR regions of 6- and 12-hour powders.**

Contrast maps generated from signal intensity of representative anatase ($640\ cm^{-1}$) and rutile ($430\ cm^{-1}$) identified distinct regions of anatase in both PR and DR regions and rutile in DR regions in both the 6- and 12-hour powders. Shown in Figure 5.39, with a dashed line identifying the CP-Ti border, during anatase signal intensity (grey and blue) both PR and DR regions are illuminated, whereas during the rutile signal intensity (red and green) only the DR region is. The illuminated regions are highlighted in square brackets for each image. Results suggested that in both the 6- and 12-hour powders the PR was predominantly anatase and the DR was a mixture of both anatase and rutile crystalline forms of $TiO_2$.

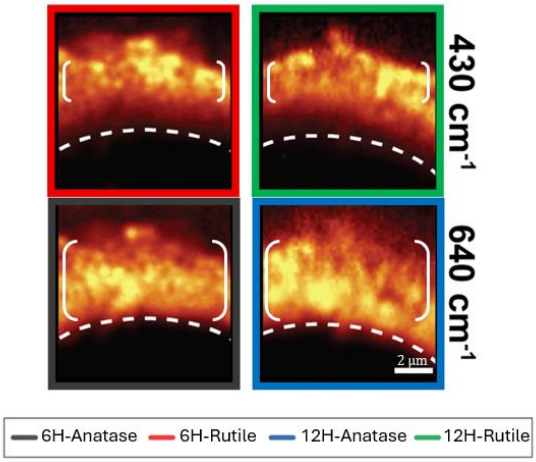


**Figure 5.39: Contrast maps of scanned regions generated from the representative signal of rutile ($430\ cm^{-1}$) and anatase bands ($640\ cm^{-1}$) with the CP-Ti border identified by dashed line. Illuminated regions highlighted with square brackets identify anatase (grey and blue) presence in PR and DR regions and rutile (red and green) presence in DR region.**

## 5.5 Photocatalytic Testing

### *5.5.1 Methodology*

The next step after verifying the growth of anatase and rutile nanostructures was to test its photocatalytic behaviour. Calcinated 6- and 12-hour powders were subjected to organic pollutant, methylene blue (MB), and mixed into deionized water to create a slurry. 1 L of MB solution was prepared by mixing 0.5 g of MB with 1 L of deionized water to produce a 500 ppm (parts per million) concentration. 0.01 g of $TiO_2$ was added to 48 mL of deionized water and ultrasonically mixed for 15 minutes. Then, in a UV safe room under a fume hood, 2 mL of 500 ppm MB was added and magnetically mixed for 30 minutes to achieve adsorption - desorption equilibrium. These parameters were selected by utilizing available equipment and referencing literature to have a baseline for comparison [44].

After 30 minutes and while still mixing, 5 mL samples were removed from the beaker and placed in glass vials before UV exposure. Vials were used because samples were removed at 5-minute intervals from the UV box and it was unsure if altering the concentration by 5 mL in a single larger sample size during every time interval could affect performance. Samples were subjected to 75% of 600W. Samples were removed from the light source at timed intervals and centrifuged at 6000 rpm for 10 minutes to separate the powder from the MB. 1 mL from the MB samples was then pipetted into well plates for plate reading to measure light absorbance (A).

Experiments were also conducted with commercial anatase powders already in the University of Ottawa Cold Spray Lab inventory, Altair and Neoxid, for performance comparison. SEM images were taken of the powders to see the surface level differences (Figure 5.40). Both The Altair and Neoxid powders had similar particle size, both being smaller than the 12-hour powder with all three presenting different surface morphologies. Altair had a rough surface with no clear nanostructural type. Its surface morphology appeared diverse with many non-symmetrical obtrusions giving it an uncharacterized geometry. On the other hand, Neoxid presented a uniform morphology of nanospheres of uniform thickness encompassing the total circumference of each particle. In some instances, cylindrical nanorod formations were noted which gave the appearance of nanospheres that had fused together. The 12-hour powder presented non-uniform thickness of spiked nanorods that grew to a point as they elongated. Its nanostructure layer appeared to have the most depth out the three different surface morphologies.

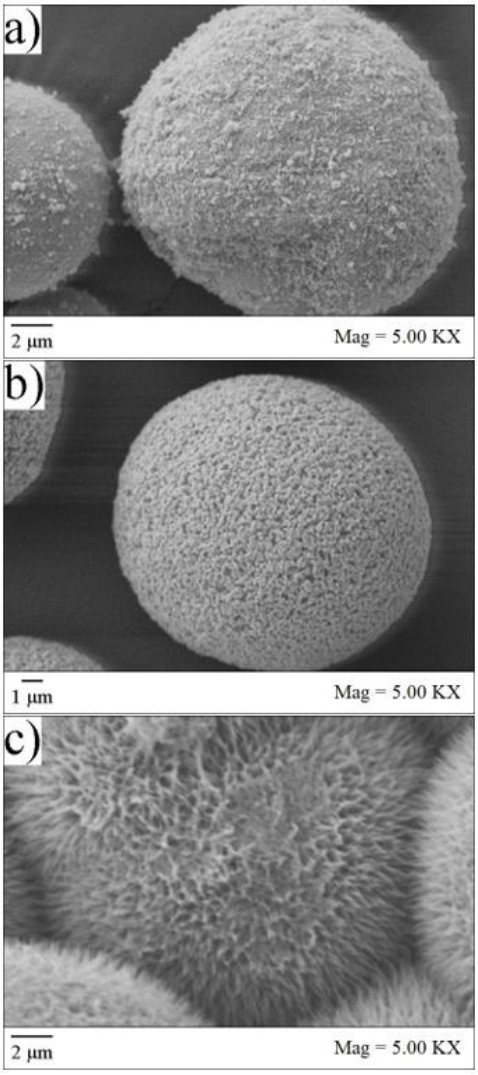


**Figure 5.40: SEM images of a) Altair, b) Neoxid, and c) 12-hour powder at 5.00KX magnification.**

By decreasing the magnification, aggregates on the nanorods could be seen on the 12-hour powder (Figure 5.41 a)). The aggregates exhibited similar morphological shape to studies that successfully grew nanoflowers [95], [99], [100]. In theory, the presence of additional growths would contribute to higher surface area and more locations for ROS generation. Alternatively, in some areas it presented like the nanorods had fused together creating smoother surfaces (Figure 5.41 b)). Which would in turn decrease porosity and surface area, also affecting ROS generation locations.

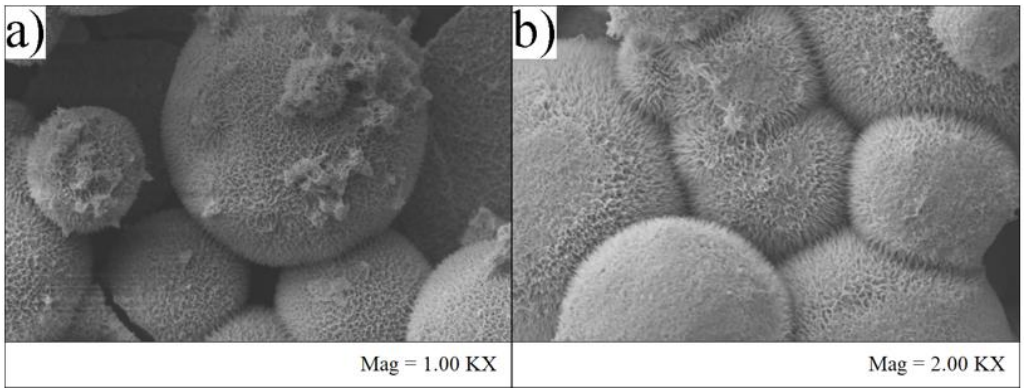


**Figure 5.41: SEM images of 12-hour powder batches at a) 1.00KX and b) 2.00KX magnification.**

Experiments were also completed that placed the 150 mL beaker used for mixing directly into the UV box and samples were pipetted out of the single slurry vessel every 5-minutes. The primary reason vials were used was to limit the effects of altering the volume and potentially component concentrations every 5-minutes could have on the overall system. For example, the first 5 minutes would be exposed to 50 mL, then 10 minutes would be exposed to 45 mL, and so on. Alternatively, changing the procedure a larger birds-eye surface area for UV exposure could result in better reactivity due to more direct exposure to $TiO_2$. Both vial and beaker experimental procedures are shown in Figure 5.42 where steps 1, 2, and 4 were completed in a UV safe room. Step 3 was completed just outside the UV safe room as this was where the centrifuge was located. The microplate reader was also located outside of the UV safe room.

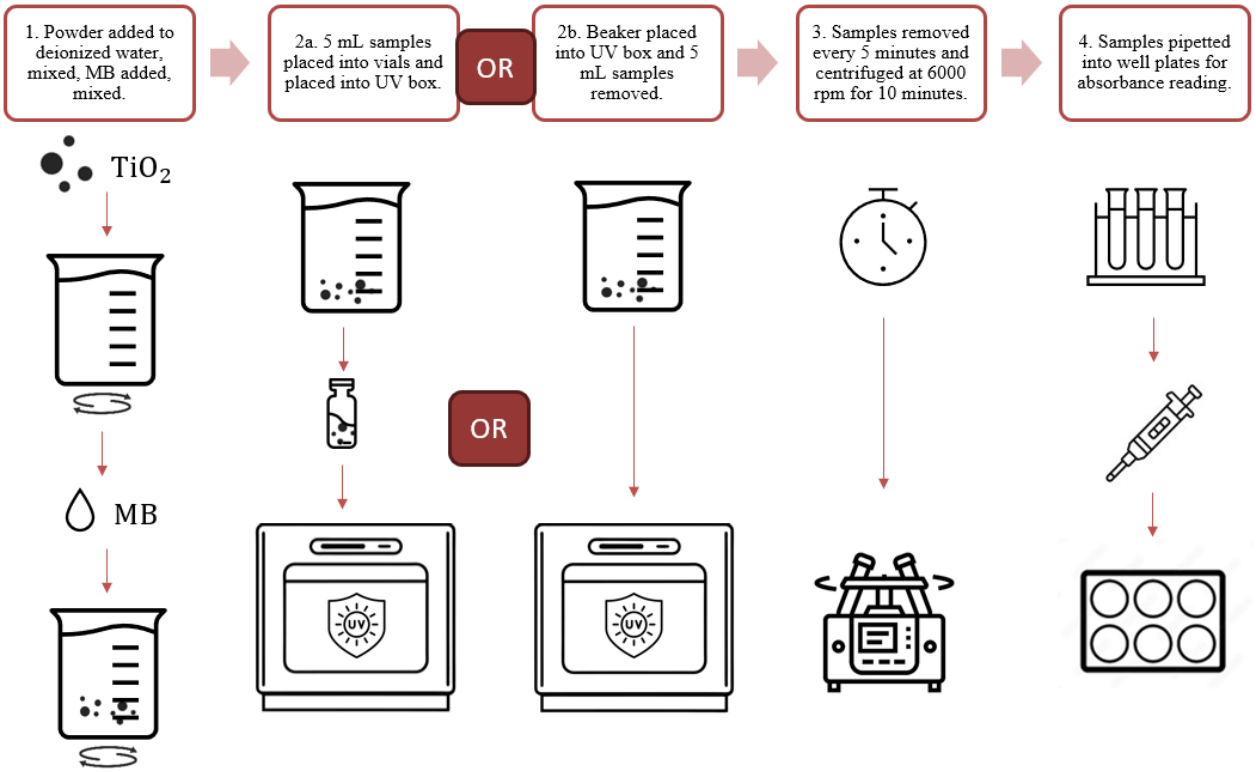


**Figure 5.42: Photocatalytic testing procedural steps. 1. $TiO_2$ added to beaker and mixed for 15 minutes, MB added and mixed for 30 minutes. 2a. 5 mL samples placed into vials and then placed into the UV box OR 2b. The beaker is placed into the UV box and 5 mL samples are pipetted out. 3. Samples are removed every 5 minutes and centrifuged at 6000 rpm for 10 minutes. 4. Samples are pipetted into well plate for absorbance reading.**

### *5.5.2 Results*

5 mL vials were removed every 5-minutes from the UV box, centrifuged, and then 1 mL was pipetted into well plates for absorbance readings (Figure 5.43).

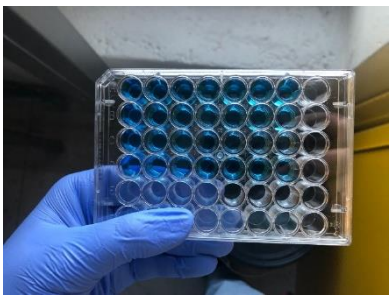

**Figure 5.43: MB and $TiO_2$ aqueous slurries after UV exposure, centrifugation, and being pipetted into well plate for light absorbance readings.**

Comparing the 6- and 12-hour powders in vials revealed that they followed similar paths, with the 12-hour powder decomposing more MB than the 6-hour powder (Figure 5.44, where V denotes vials and the measurement at 0 minutes is a sample of the MB and $TiO_2$ slurry after 30 minutes of

mixing with no UV exposure). This indicated that the 12-hour powder was more reactive than the 6-hour powder. As a result, the 12-hour powder was used as the reference when comparing to commercial powders.

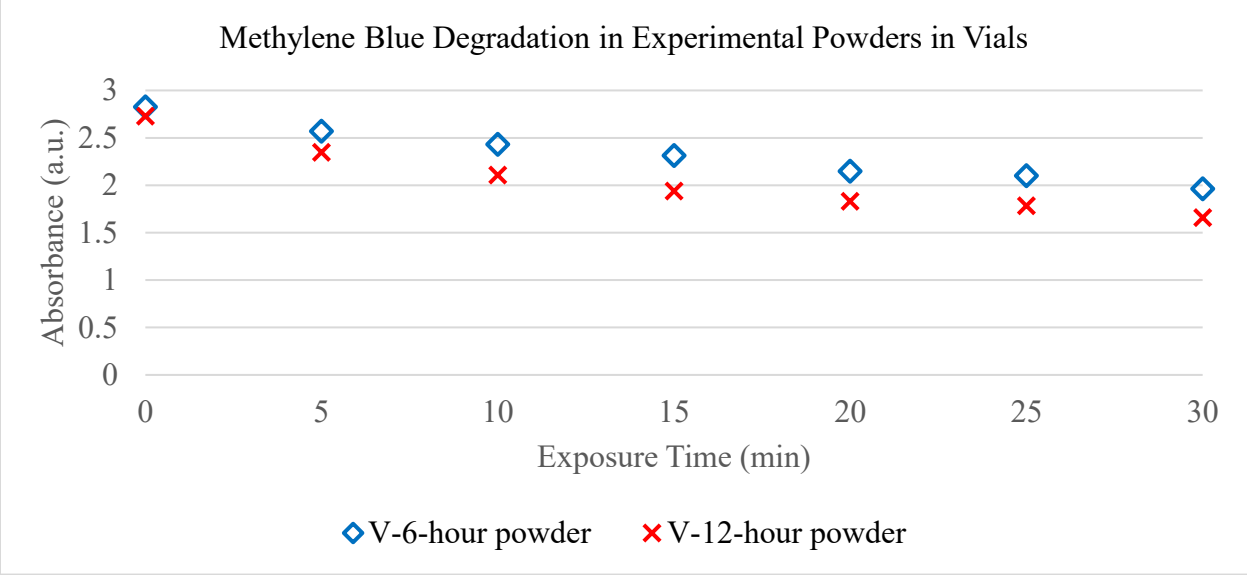


**Figure 5.44: Plotted MB degradation in 6- and 12-hour powders after 30 minutes of UV exposure in vials.**

Visually comparing the commercial powders to the 12-hour powder; immediately upon mixing with deionized water in the beaker with the powders, Neoxid was white and cloudy creating an opaque slurry. The Altair slurry was minorly cloudy becoming translucent, and the 12-powder was not cloudy in appearance, remaining transparent (Figure 5.45).

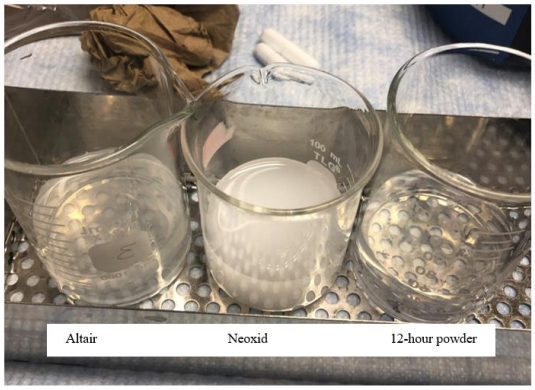


**Figure 5.45: $TiO_2$ powders mixed with deionized water, prior to MB addition and UV exposure.**

After 30 minutes of mixing in the MB and prior to UV exposure, both the Altair and Neoxid were cloudy, akin to how they appeared prior to MB addition. As a result, the slurries looked lighter in appearance, but the lightness could be attributed to the effect of the powder in water and its

transparency, and not to MB being adsorbed (Figure 5.46 a)). After 30 minutes of UV exposure all three samples had turned lighter blue with Altair being the lightest in colour, followed by Neoxid, and then the 12-hour powder (Figure 5.46 b)).

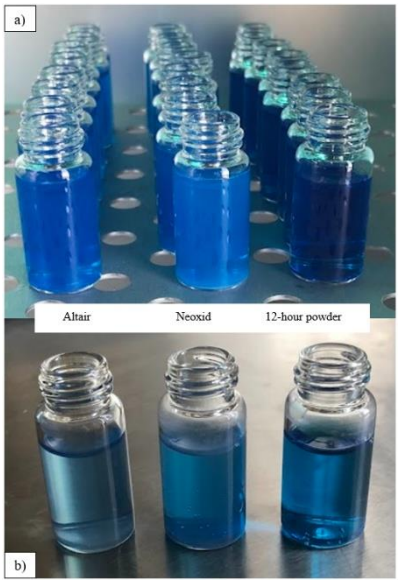


**Figure 5.46: MB slurries in vials a) before and b) after 30 minutes of UV exposure.**

Absorbance readings showed that all three powders started with similar MB concentrations and that after 30-minutes of exposure the Altair had adsorbed the most MB, followed by Neoxid, and then the 12-hour powder. At 5- and 10-minutes, the 12-hour powder had adsorbed more than Neoxid. All three powders showed higher absorption in the first 15 minutes, than when compared to the last 15 minutes. Indicating higher reaction rates immediately upon UV exposure (Figure 5.47).

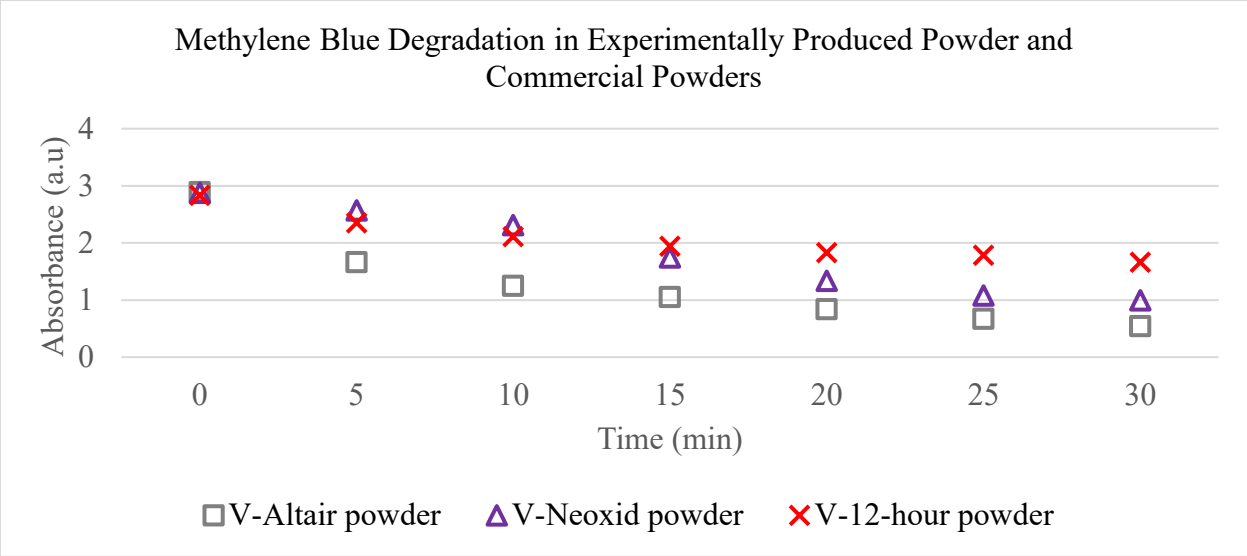


**Figure 5.47: Plotted MB degradation in Altair, Neoxid, and 12-hour powders after 30 minutes of UV exposure in vials.**

Completing the experiment without vials and leaving the 50 mL slurries in the 150 mL beakers with 5 mL being removed every 5-minutes showed better MB adsorption in both the 6- and 12-hour powders. Interestingly, they recorded similar values to the 15-minute mark before the 12-hour powder adsorbed more MB than the 6-hour powder up to the 30 minutes of UV exposure. The results indicated that having a larger surface area for UV exposure resulted in higher photocatalytic activity. Additionally, the 12-hour experimental powder may have had the ability to maintain increased MB adsorption than the 6-hour powder for longer durations (Figure 5.48, where V denotes vials and B denotes beakers).

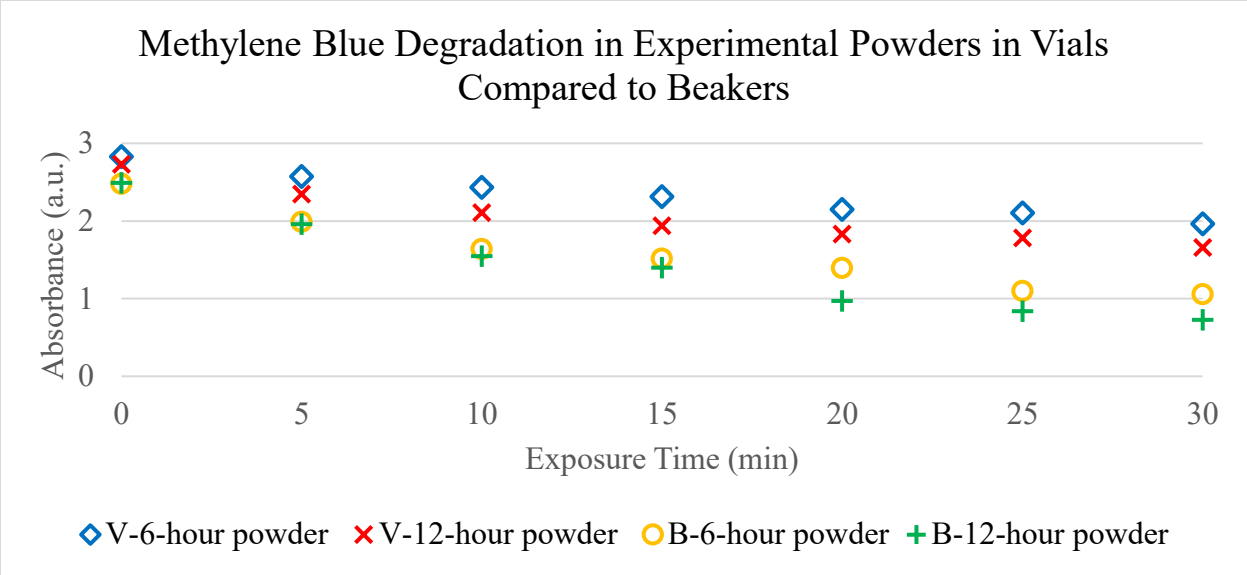


**Figure 5.48: Plotted MB degradation in 6- and 12-hour powders after 30 minutes of UV exposure in vials and beakers.**

The Altair, Neoxid, and 12-hour powder beaker slurries prior to UV exposure did not present the same notable differences in appearance as in the vials. Due to the higher volume of slurry, less transparency characteristics were noted and all three appeared dark blue in appearance, with Neoxid presenting slightly more opacity (Figure 5.49 a)). The most notable change was seen after 30 minutes of UV exposure where the Neoxid slurry was almost fully void of blue colouring, reverting to a pale blue, cloudy mixture, similar to its appearance prior to adding MB (Figure 5.49 b)). Due to the lack of blue in appearance correlating to the absence of MB, Neoxid could be expected to have the highest photocatalytic activity.

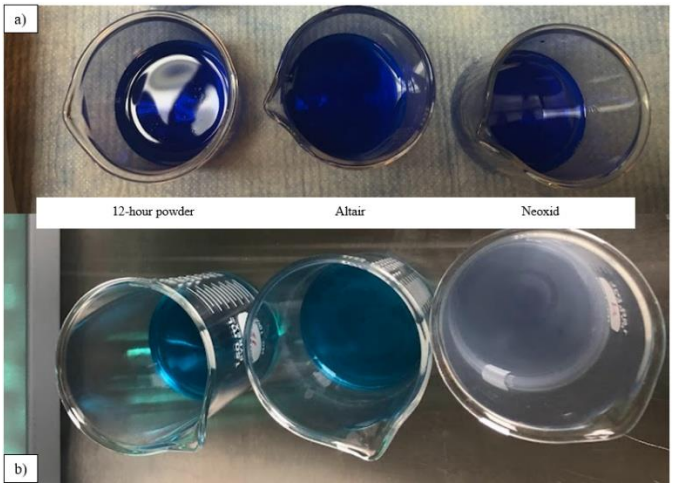


**Figure 5.49: MB slurries in beakers a) before and b) after 30 minutes of UV exposure.**

As predicted, the Neoxid slurry in the beaker showed the most photocatalytic activity out of all vial and beaker experiments. For both Neoxid and the 12-hour powder, there was more reactivity when exposed to UV in the beaker than in the vials. The B-12-hour powder beaker showed the highest 5-minute interval of adsorption in the first 5 minutes, and B-Neoxid in 15–20-minute where it overtook the 12-hour powder in overall adsorption. Interestingly, the Altair powder performed better in the vials than the beaker. Samples were pipetted out near the surface of the slurry with the intent of removing the least amount of $TiO_2$ if it had settled to the base of the beaker. Depending on the characteristics of the powder, if the Altair powder remained well-mixed and suspended in the slurry, more could have been removed than the other powders every 5 minutes. The potential overall decrease in $TiO_2$ concentration could affect its photocatalytic performance. Overall, the produced 12-hour powder performed similarly to the commercial powders, not exhibiting superior photocatalytic activity, indicating it did not possess the reactivity threshold required to react under visible light.

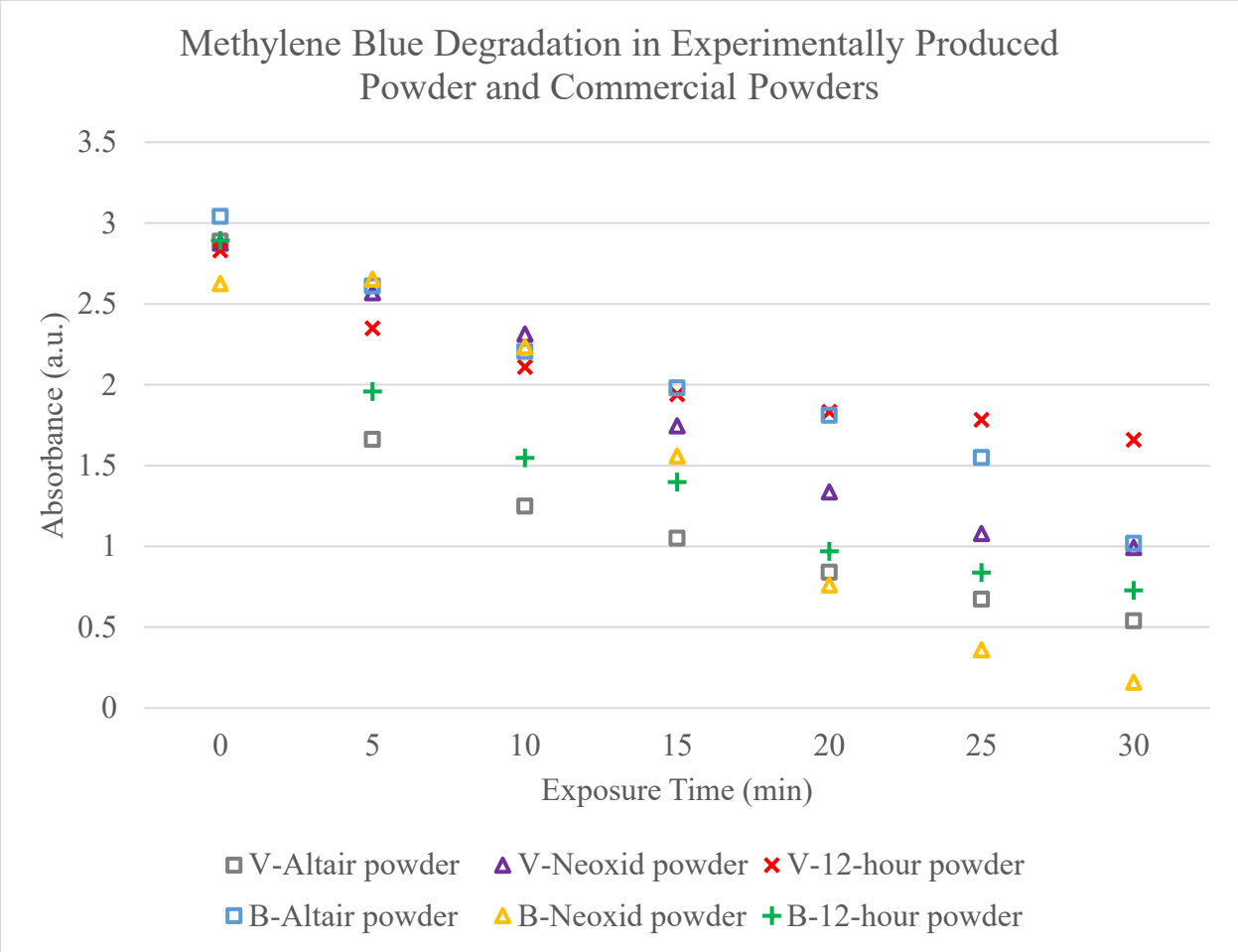


**Figure 5.50: Plotted MB degradation in Altair, Neoxid, and 12-hour powders after 30 minutes of UV exposure in vials and beakers.**

Studies have seen that increasing the available surface area for reactions increases photocatalytic activity because the generation of ROS occur at the $TiO_2$ surface [78]. This correlated to observed higher reactivity in beakers than vials because more $TiO_2$ was present in the single location that provided a larger surface area for UV exposure. Additionally, as seen in the SEM images of the powders (Figure 5.40), both commercial powders were smaller in particle size than the experimental powder. Even by conducting experiments based off measuring the same mass of each powder, the commercial powders would have more surface area to promote more ROS generation. Furthermore, the format of this photocatalytic test was impacted by the powders behaviour when suspended in a slurry, which are a result of the material properties such as nanostructure type and shape, surface area size and morphology, and particle size and density. In CGDS, the powders suspension properties in deionized water would not affect its photocatalytic reactivity.

The photocatalytic behaviour of the powders in the slurry could be affected if a method of mixing was presented throughout UV exposure. For example, continuous magnetic stirring, although this was impossible due to the size of UV box and inability to run electronics inside while the machine was on. Or potentially mixing the slurries after each UV exposure to redistribute the powder. The current methodology pipetted samples near the top of the vials and beakers, centrifuged, and once again pipetted samples near the top of the centrifuge tubes into the well plates. The purpose of this was to ensure no powder particles were placed into the well plates. If samples were continuously mixed throughout exposure there would have been a higher chance of powder particles in the well plates. This methodology did not guarantee powder particles were not in the well plates which could have affected the readings. To avoid this in future experimentation it is recommended a blank absorbance reading is taken of the powders each within water and without MB. Subtracting this reading from those measured ensures the powder is not affecting the MB absorbance results.

Factors that could influence the absorbance readings and experimentation reproducibility include the following:

- Mixing.
    - Particle suspension behaviour resulting in uneven suspension, settling, or grouping.
- Sample Volume.
    - Slight variations would alter optical pathways in microplate reader.
- Time.
    - Delays and variations between removing samples from UV box, centrifuging, and plate readings could have allowed adsorption and desorption to continue causing inconsistent time-point readings.
- Ambient Light Exposure.
    - Although the mixing and UV box experiments were completed in a UV safe room, both the centrifuge and microplate were located outside. The exposure to ambient light and duration could alter the photocatalytic reaction rates.
- Temperature.
    - Variance in temperature would affect the adsorption and photocatalytic behaviour.
- Centrifugation.
    - Removing powder from samples could also remove MB dye adsorbed.

    - Fine particles that remain could alter absorbance readings.
- Sample Holder.
    - Residues, scratches, and geometry could scatter light and affect transmission in both the UV box and microplate reader.
- Microplate Settings.
    - Wavelength accuracy, slit width, and scanning speed can cause small deviations.

As previously discussed, the experimental powder synthesis procedure could be analyzed step by step to produce more reactive powder. Variation to the chemical bath and calcination parameters to control the nanostructures and geometry for higher UV reactivity and / or visible light reactivity. Considering that the breakdown of $C_3N_3(NH_2)_3$ introduces nitrogen (N) atoms which can substitute for oxygen in the $TiO_2$ lattice and potentially create N-doped $TiO_2$. N-doping can narrow $TiO_2$ band gap and enhance photocatalytic reactivity in the visible light range [12], [40], [50], [56], [67], [190], [293], [294]. Although, at higher calcination temperatures the nitrogen content decreases [118]. Considering this, the optimal chemical bath and calcination parameters could vary for enhanced photocatalytic activity under UV with higher anatase presence or photocatalytic reactivity closer to the visible light range with higher rutile phase and N-doping. The confirmation of synthesizing photocatalytic $TiO_2$ using the established methodology in this work allows for advancement in precise experiments to optimize the developed powder.

## 5.6 Dynamic Vapour Sorption

### *5.6.1 Methodology*

The DVS performed used octane as the solvent and dry $TiO_2$ powder as the sample. DVS was completed on powders to measure the isotherms and surface properties of experimental and commercial powders that influence photocatalytic properties. 1.5 g samples of Altair and Neoxid along with two 0.1 g samples of calcinated 12-hour powder from two separate batches were provided.

### *5.6.2 Results*

The powders were analyzed at around standard octane sorption temperature ($T_{oct}$), 25 ℃, which allowed for optimal conditions to analyze and compare sorption behaviours and the BET specific

surface areas ($S_{BET}$) were obtained (Table 5.9). Altair exhibited the largest $S_{BET}$, with Neoxid presenting the smallest. The 12-hour powders were in the middle.

**Table 5.9: $M_{ref}$ and $S_{BET}$ of DVS powders.**

| Sample Vial | Powder | $T_{oct}$ (°C) | $M_{ref}$ (mg) | $S_{BET}$ $m^2/g$ |
|---|---|---|---|---|
| **1** | Altair | 25.3 | 16.97 | 17.3 |
| **2** | Neoxid | 25.3 | 10.46 | 3.8 |
| **3** | 12-hour powder sample 1 | 24.2 | 19.18 | 11.7 |
| **4** | 12-hour powder sample 2 | 23.9 | 11.67 | 11.4 |

Altair presented large $S_{BET}$ with minor impurities and relatively uniform mesopores. It displayed a Type II S-shaped isotherm. The uptake at the top of the rise in the curve at around 60% indicates the completion of the monolayer and the beginning of a second monolayer. There was no strong indicator to confirm a completed second monolayer, confirming a homogeneous surface composed solely of anatase (Figure 5.51).

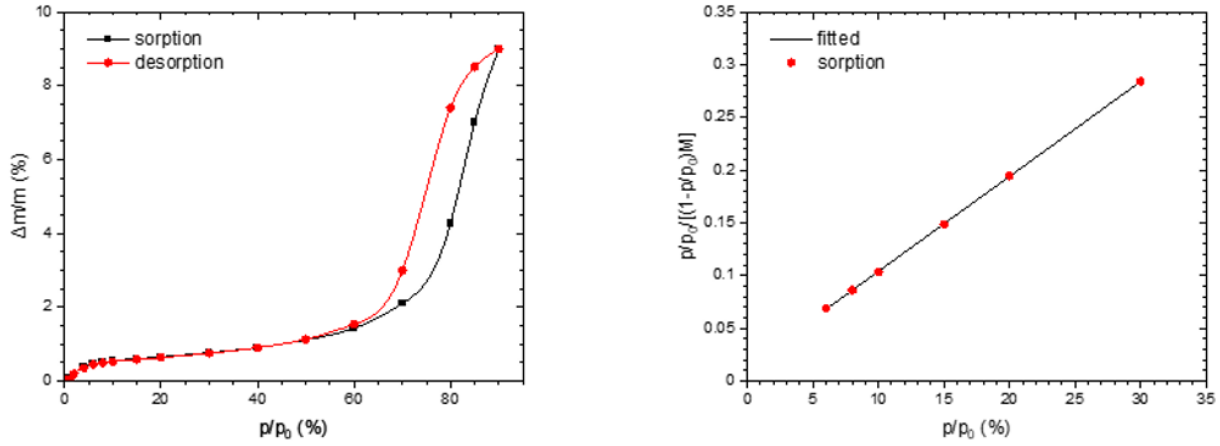


**Figure 5.51: DVS results of commercial Altair powder.**

Neoxid presented a smaller surface area which made the BET curve harder to achieve. The smaller $S_{BET}$ could be associated to either larger particles or a higher powder density. As the Neoxid and Altair seemed comparable in particle size from the SEM images, the smaller $S_{BET}$ could then be attributed to higher powder density. Neoxid could also be categorized as a Type II isotherm with the completion of the monolayer at around 35% (Figure 5.52). Like Altair, it did not have completion of a second monolayer also concluding a homogenous anatase surface.

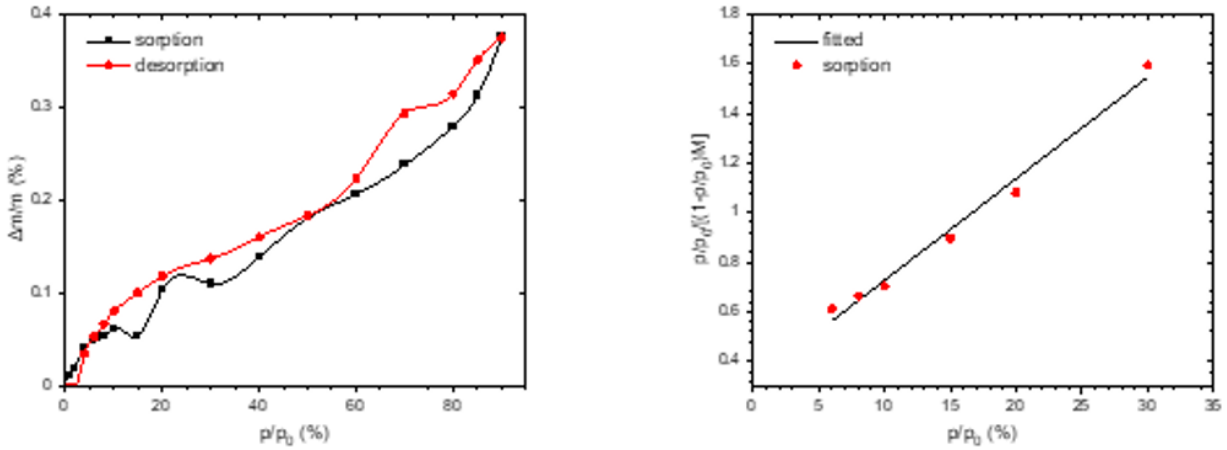


**Figure 5.52: DVS results of commercial Neoxid powder.**

Neoxid powder having high density could provide the justification for its photocatalytic testing results where it outperformed the other two powders exclusively in the beakers. If the powder had notably different density and settled quicker and more efficiently to the bottom of the beaker then possibly more powder avoided being pipetted out every 5 minutes. Furthermore, potentially stationary powder at the bottom of the beaker created a better environment for ROS generation than powder particles suspended and moving in the slurry. Powder particles settling to the base of a beaker and potentially being in contact with each other could have created a larger surface for ROS reactions. Contrastingly, Altair having a large $S_{BET}$ could then be congruent with a lower density, promoting better suspension in the slurries. If so, Altair performing with more degradation in the vials could be attributed to more exposure because of the moving $TiO_2$ particles. The vial design tapers at the top, which could result in less direct UV exposure to the base of slurries.

There was no significant difference between the two samples of 12-hour powders. They presented a prominent hysteresis loop which is seen when there is a gap between the adsorption and desorption curves indicating the sample material adsorbed more octane than it released at the same RH (Figure 5.53). The area between the sorption and desorption curves indicated octane trapped in the mesopores resulting in capillary condensation. Capillary condensation is a phase transformation where the pores of the powder would be filled with liquid-like phase of octane [178]. This type of hysteresis loop is typically seen in platy particles and/or complex interconnected networks of slit-shaped mesopores as the geometry contributes to a faster adsorption rate than desorption rate. The 12-hour powders had the most uniform surface and were Type IV isotherms with clear multilayer adsorption indicating highly porous adsorbents. The first

monolayer was completed around 45% with the second monolayer being completed around 68%. The presence of two clear monolayers could be due to the heterogeneous nanostructures, anatase and rutile.

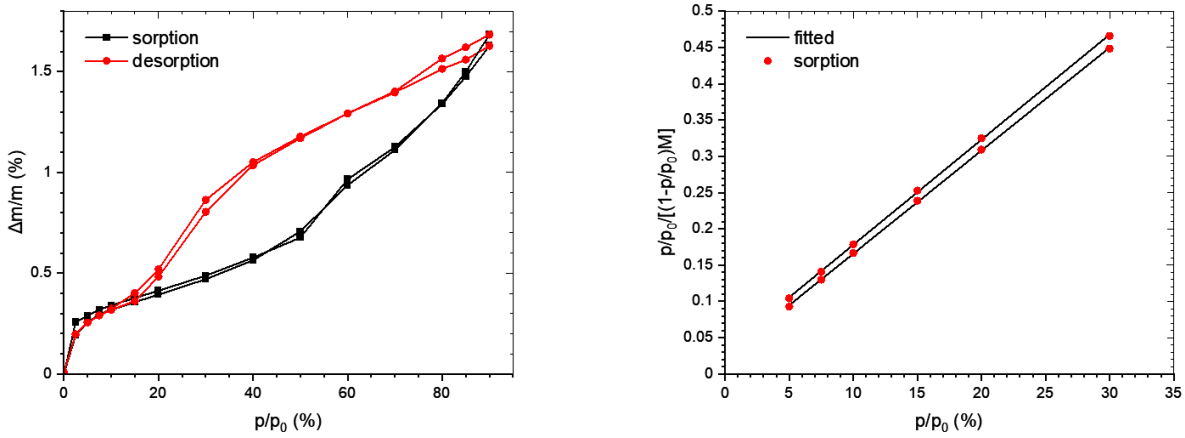


**Figure 5.53 DVS results of both 12-hour powders plotted together.**

The experimental powders having multilayer adsorption indicating highly porous adsorbents was extremely favourable as those results are congruent with strong ROS generation zones. The photocatalytic procedure may have not promoted optimal reactivity in the experimental powder. For example, how changing to a larger slurry vessel improved Neoxids performance and subsequent results significantly. The plot from Figure 5.50 was re-plotted measuring the absorbance over $S_{BET}$ with respect to time. Applying this fraction provided data points of absorbance per 1 $m^2/g$ of each powder for comparison (Figure 5.54).

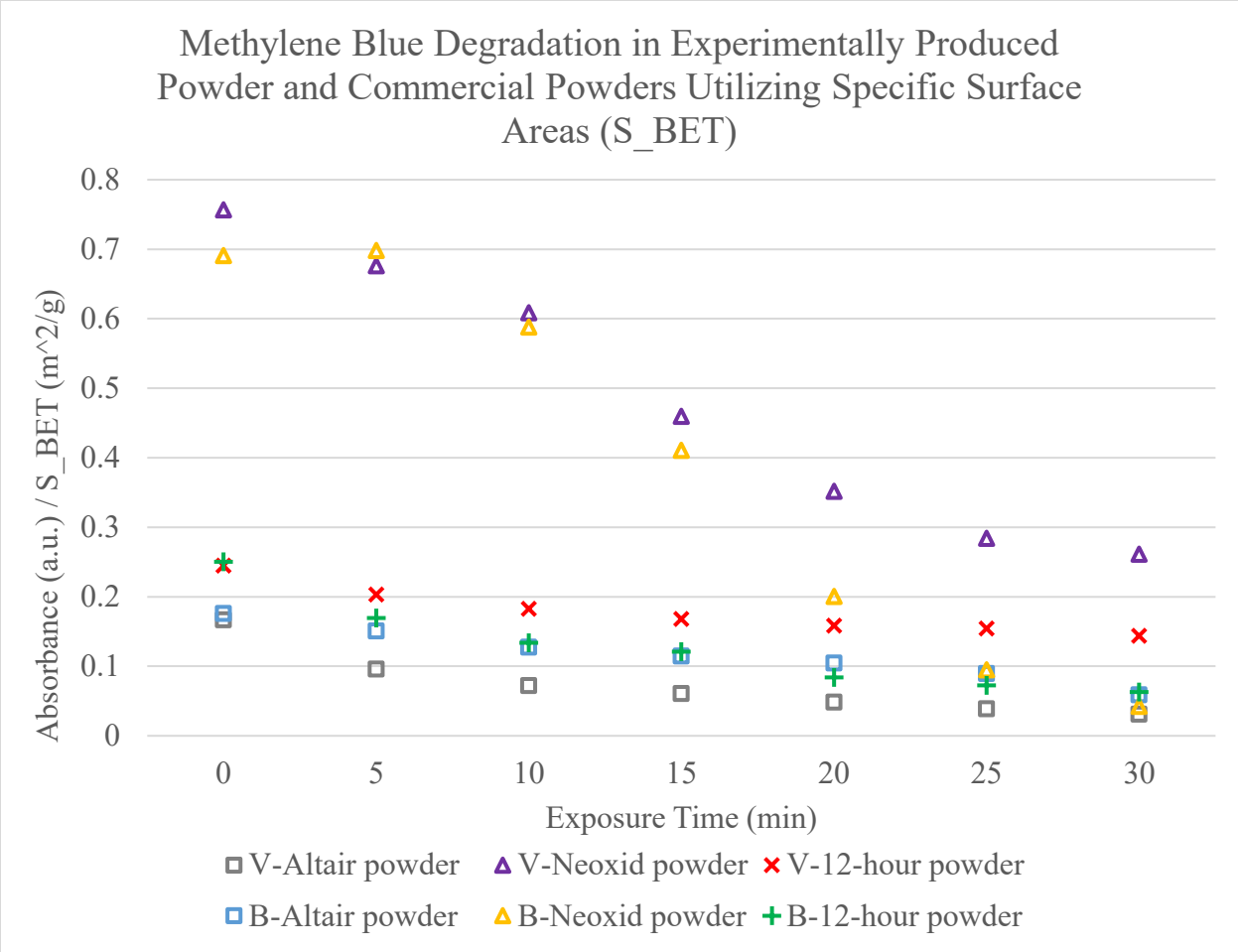


**Figure 5.54: Plotted MB degradation in Altair, Neoxid, and 12-hour powders after 30 minutes of UV exposure in vials and beakers utilizing $S_{BET}$.**

Neoxid exhibited the highest rate of change over time. This was expected as it had a significantly smaller $S_{BET}$ to that of Altair and the 12-hour powder, providing it with the highest starting value at 0-minutes. Interestingly, the V-Neoxid powder had the poorest performing absorbance at the 30-minute mark, different from Figure 5.50 which was the V-12-hour powder. Due to their high $S_{BET}$ differential, the Altair powder had the highest absorbance at the 30-minute mark, whereas Neoxid did in Figure 5.50. The V-Altair and B-Altair had the closest final absorbance at 30-minutes than the other powders when comparing the same powders behaviour in vials and beaker. Altair having the largest $S_{BET}$ with uniform mesopores could correlate to low density, an opposite feature of Neoxid. Consequently, it is possible the Altair powder exhibited the strongest integration in the slurry with less powder settling to the bottom of the vials and beakers.

The V-Altair, B-Altair, B-Neoxid, and B-12-hour powder had similar levels of absorbance at 30-minutes ranging from $\sim 0.03$ to $\sim 0.06$ $(A/S_{BET})$. These values had a smaller differential than when compared to the sole absorbance values ranging from $\sim 0.16$ to $\sim 1.02$ $(A)$ seen in Figure 5.50, signifying that the powders produced similar results after 30-minutes per 1 $m^2/g$ for each powder. This corroborates the statement that the 12-hour experimental powder performed comparatively to commercial $TiO_2$ powders in this form of photocatalytic testing, validating the successful growth of photocatalytic $TiO_2$ on Ti powder. The 12-hour powder did not outperform the commercial powders, which would have implied higher reactivity. This could be attributed to varying factors regarding powder properties, like type of isotherm or nanostructures, or also powder performance in conjunction with the photocatalytic testing methodology.

# 6 CONCLUSION

The objective of the thesis was to successfully grow a $TiO_2$ shell on a CP-Ti powder with heterogenous nanostructures of anatase and rutile for photocatalytic behaviour, with the intent to eventually produce sprayable powder for strong adhesive CGDS coatings on various surfaces. The motivation of this work was to utilize the ductility of Ti below its melting point to promote deposition efficiency in CGDS applications to develop a coating with photocatalytic properties from the ceramic $TiO_2$ shell that undergoes phase transformations at higher temperatures. Heterogeneous nanostructures were grown because research showed strong reactivity from anatase with stability from rutile and that the presence of their coupling increased lattice structure disorder and promoted the generation of ROS, crucial to photocatalytic reactivity. Rutile's smaller band gap closer holds promise in further project development for photocatalytic coatings under the visible light range.

Preliminary experiments were completed on Ti plates with $H_2O_2$ before being done on CP-Ti powder due to ease of access and for comparisons with reference literature where $TiO_2$ was grown on Ti surfaces. Limited growth development on the plates and first few powder batches was a result of initial chemical loss due to experimental set up and then the realization of using expired $H_2O_2$ in experiments. Final changes to the powder production methodology included effective $H_2O_2$, the addition of $HNO_3$ and $C_3N_3(NH_2)_3$ to the chemical bath and duration decrease from 72 to 12 hours, PTFE coverings for liquid retention, and calcination once the powder was dry at 450 ℃ for 1 hour. SEM images showed more distinguished nanorod like growth on calcinated samples. XRD and Raman spectroscopy confirmed the heterogeneous nature of the $TiO_2$ that correlated to successful growth of anatase and rutile nanostructures with the ratio favouring more anatase than rutile. The shells presented more rutile in the growth closest to the CP-TI core with primarily anatase along the outside of the $TiO_2$. The shell thickness was measured to range from 2.5 μm to 2.7 μm.

Photocatalytic testing was conducted using a UV box and combining deionized water, $TiO_2$ powder, and MB as the organic pollutant to be adsorbed by the $TiO_2$ surface and subsequently deteriorated by the ROS generated under UV photoexcitation. The slurries were subjected to 30-

minutes of UV exposure with samples removed every 5-minutes, centrifuged, and pipetted into a well plate for light absorbancy readings. Experimental powders that had been immersed in a chemical bath for 6- and 12-hours were first subjected to photocatalytic testing because they presented similar SEM images. The 12-hour powder did show higher anatase and rutile peaks in the XRD analysis, which was supported when the 12-hour powder exhibited more MB degradation than the 6-hour powder. It was seen that the commercial Altair powder in vials exhibited the most MB degradation, with commercial Neoxid and the experimental powder showing similar degradation. The experiment was repeated with larger beakers holding the slurries, providing a larger singular surface area for UV exposure. These results yielded a more prominent decrease in blue colour in all three beakers, visually indicating MB degradation. The commercial Neoxid powder was most pale in colour after 30-minutes which correlated to it having the most MB degradation in the plate readings. The 12-hour experimental powder performed better than the commercial Altair powder during the beaker experiments, but Altair performed better in the vials. The results indicated more degradation in larger vessels for Neoxid and 12-hour powder, which could be a result of a larger area for UV exposure and a higher concentration of $TiO_2$ in the slurries than when in smaller vials. SEM images of all three powders showed the particle size of Altair and Neoxid to be similar and smaller than the 12-hour powder. Per weight, the commercial powders having more particles due to their size could translate to having more $TiO_2$ readily available to react with the UV light and generate ROS as opposed to the experimental powder with larger particles.

Through DVS, the commercial Altair and Neoxid powders were both categorized as Type II isotherms with single monolayers. This confirmed they possessed singular nanostructures of anatase. The experimentally produced powder was a Type IV isotherm having two distinct monolayer completions in DVS from the heterogenous nanostructures of anatase and rutile. Altair exhibited the largest $S_{BET}$ which could have contributed to the highest MB degradation seen in the vial experiments. A large $S_{BET}$ could imply low density and subsequently integrate more efficiently into the slurry and maintain suspension. Neoxid presented high powder density which could have contributed to its high performance in the beaker experiments having the powder settle at the base of the slurry, providing powder particle contact and surface for ROS generation, and avoid being pipetted out every 5-minutes. The data from photocatalytic testing was re-plotted with the ratio of

absorbancy over $S_{BET}$ in respect to time to take into consideration the effects of varying $S_{BET}$ of each powder. All three powders from the beaker experiments had similar levels of degradation at the 30-minute mark concluding they achieved similar overall MB degradation per 1 $m^2/g$. Ultimately, powder behaviour in the slurries could have affected results due to material properties and therefore proportionally impacted reactivity. A higher density powder settled to the bottom of a beaker with higher MB degradation could propose better photo reactivity along a surface, like a CGDS coating, than when suspended in a slurry.

In conclusion the experimentation was successful in developing a $TiO_2$ shell on a spherical CP-Ti powder with heterojunctions of anatase and rutile nanostructures. The experimental powder had confirmed photocatalytic behaviour when mixed with MB and subjected to UV light and compared to commercial powders. This work created a strong foundation to improve upon in creating experimental $TiO_2$ on Ti powders for CGDS applications that exhibit superior adhesion to substrates with increased ductility and higher photocatalytic properties than commercial powders.

# 7 FUTURE WORK

The thesis work offers various future avenues of exploration. The following section is broken down into the stages of research objectives and options for expansion are discussed.

## 7.1 Experimental Powder Production

Powder production holds variabilities in the procedure that could be altered and analyzed to produce varied $TiO_2$ shell outcomes. As this was the first stage of the research, altering any element could have varying effects on the subsequent stages such as anatase-rutile ratios, nanostructure surface morphologies, photocatalytic reactivity, and deposition efficiency in CGDS. The elements in which could be altered and the effects analyzed include:

- Completing experiments on various brands of CP-Ti.
- Powder preparation and storage prior to the chemical bath.
- Chemical ratios in the bath or introducing a new chemical bath methodology.
- Ultrasonic mixing of chemical bath duration.
- Duration and temperature of the oven.
- Coverage mechanism of chemical bath in the oven.
- Duration and temperature of the calcination.

The powder could be developed and tested for reactivity under visible light as the intent behind creating a shell with both anatase and rutile was to increase the reactivity through dislocations in the lattice structure and better charge separation. Anatase is commonly used for its reactivity, but rutile is the crystalline structure with its band gap the closest to the visible light range. Powder methodologies could be developed to vary the ratios of anatase to rutile, as well as the nanostructural morphology, and test the photocatalytic properties to determine an optimal ratio and growth pattern. Additionally, the $TiO_2$ powder could also be doped or co-doped with metal or non-metal ions to reduce the band gap or have dye added for increased sensitivity that captures visible light and transfers it to the $TiO_2$ surface. The experimental powder should be verified to see if it did produce N-doped $TiO_2$ from the $C_3N_3(NH_2)_3$ in the chemical bath. $TiO_2$ could also be developed on Ti alloy powders where additional semiconductor metal presences aim to push the

reactivity into the visible light range with a narrower band gap. Alternatively, the $TiO_2$ powder could be mixed with others powders that promote photocatalytic reactivity or CGDS deposition.

Also, pH testing should be completed on the experimental chemical bath developed. Understanding the pH of the chemical bath can allow for altering quantities or chemicals to promote rutile or anatase structures, as well as specific nanostructure formations to promote photoreactivity. An alternative powder methodology for high anatase to rutile ratios could include a chemical bath of pH that supports growth of pure anatase, followed by higher calcination temperatures around 650 to 700 ℃ to induce phase transformations from anatase to rutile for heterogenous $TiO_2$. Experiments with a focus on calcination could be completed to analyze the effect of calcination temperature and duration on photocatalytic performance to determine ideal parameters for the developed experimental powder that maintain the reactivity from anatase and potential visible light reactivity from rutile.

As the experimental powder is intended to be used in CGDS, a key change to the procedure would be increasing the powder production output. Currently, the powder production does not provide a significant amount of powder to that of chemical bath, producing 1 g of powder per 1 L. Significantly increasing the amount of powder made would provide the research with enough powder needed to effectively CGDS and analyze deposition.

## 7.2 Photocatalytic Testing

The photocatalytic procedure was developed through reference literature and equipment available within the University of Ottawa research teams. The procedure itself could be altered through durations of any stage such as mixing of the slurries, UV exposure, and time spent in the centrifuge to separate the powder. The methodology in which powder was exposed to a UV source could be changed in numerous ways such as the slurry housing containers, slurry mixing equipment and execution, sample extractions, and centrifuged parameter. An alternative method to plate reading could also be used to measure the degradation of MB, or other organic pollutants as completing experiments with varying pollutants could present observations of varying reactions to different forms of bacteria. Commercial powders could be purchased that are of the same isotherm as the experimental powder to compare the photocatalytic properties in more similar $TiO_2$ powders. Furthermore, photocatalytic testing procedures could be developed for successfully CGDS sprayed

surfaces, creating more realistically accurate environments for the ultimate application of photocatalytic $TiO_2$ powder in CGDS applications.

Additionally, photocatalytic testing following the established methodology should be completed on MB in the deionized water as well as a Ti powder and MB slurry to create baselines for comparison to the $TiO_2$ powder to better evaluate the material modifications accomplished.

## 7.3 Cold Gas Dynamic Spray

The final objective of this research is to produce a photocatalytic $TiO_2$ shell on CP-Ti powder that can be used in CGDS. Further research could be completed using the procedures in this thesis to produce and spray powder. Once a powder is developed with the desired photocatalytic properties, the optimal spray method can be achieved. CGDS considerations include:

- Substrate material.
- Preheating the substrate.
- Preheating the powder.
- Process gas type.
- Spray parameters (process gas temperature and velocity).
- Nozzle angle.
- Nozzle geometry.
- Stand-off distance.

Additionally, spraying initial layers of Ti powder followed by a final $TiO_2$ surface layer could promote deposition on a rough, ductile Ti surface. The photocatalytic reaction occurs across the surface of the $TiO_2$ that is available to light excitation, therefore layering $TiO_2$ spray passes in CGDS is unnecessary as the initial layers would not contribute to the decomposition of organic matter. A coating methodology like this could improve the outcome of even, durable coatings, as well as decrease the amount of $TiO_2$ powder required and result in less experimental powder necessary to be produced subsequently lowering production costs.

# 8 REFERENCES


[1] N. T. Padmanabhan and H. John, "Titanium dioxide based self-cleaning smart surfaces: A short review," *J. Environ. Chem. Eng.*, vol. 8, no. 5, p. 104211, Oct. 2020, doi: 10.1016/J.JECE.2020.104211.

[2] S. Y. Lee and S. J. Park, "TiO2 photocatalyst for water treatment applications," *Journal of Industrial and Engineering Chemistry*, vol. 19, no. 6, pp. 1761–1769, Nov. 2013, doi: 10.1016/J.JIEC.2013.07.012.

[3] Z. Zahra, Z. Habib, S. Chung, and M. A. Badshah, "Exposure Route of TiO 2 NPs from Industrial Applications to Wastewater Treatment and Their Impacts on the Agro-Environment", doi: 10.3390/nano10081469.

[4] A. J. Haider, R. H. Al-Anbari, G. R. Kadhim, and C. T. Salame, "Exploring potential Environmental applications of TiO2 Nanoparticles," *Energy Procedia*, vol. 119, pp. 332–345, Jul. 2017, doi: 10.1016/J.EGYPRO.2017.07.117.

[5] M. N. Chong, Z. Y. Tneu, P. E. Poh, B. Jin, and R. Aryal, "Synthesis, characterisation and application of TiO2–zeolite nanocomposites for the advanced treatment of industrial dye wastewater," *J. Taiwan Inst. Chem. Eng.*, vol. 50, pp. 288–296, May 2015, doi: 10.1016/J.JTICE.2014.12.013.

[6] H. A. Foster, I. B. Ditta, S. Varghese, and A. Steele, "Photocatalytic disinfection using titanium dioxide: spectrum and mechanism of antimicrobial activity," *Appl. Microbiol. Biotechnol.*, vol. 90, no. 6, p. 1847, Jun. 2011, doi: 10.1007/S00253-011-3213-7.

[7] G. R. Khan and S. I. Malik, "Ag-enriched TiO2 nanocoating apposite for self-sanitizing/ self-sterilizing/ self-disinfecting of glass surfaces," *Mater. Chem. Phys.*, vol. 282, p. 125803, Apr. 2022, doi: 10.1016/J.MATCHEMPHYS.2022.125803.

[8] A. Afzal, A. Habib, I. Ulhasan, M. Shahid, and A. Rehman, "Antireflective Self-Cleaning TiO2 Coatings for Solar Energy Harvesting Applications," *Front. Mater.*, vol. 8, p. 205, Jun. 2021, doi: 10.3389/FMATS.2021.687059/BIBTEX.

[9] Y. Ma, X. Wang, Y. Jia, X. Chen, H. Han, and C. Li, "Titanium dioxide-based nanomaterials for photocatalytic fuel generations," *Chem. Rev.*, vol. 114, no. 19, pp. 9987–10043, Oct. 2014, doi: 10.1021/CR500008U/ASSET/IMAGES/MEDIUM/CR-2014-00008U_0042.GIF.

[10] H. A. Foster, I. B. Ditta, S. Varghese, and A. Steele, "Photocatalytic disinfection using titanium dioxide: spectrum and mechanism of antimicrobial activity," *Appl. Microbiol. Biotechnol.*, vol. 90, no. 6, p. 1847, Jun. 2011, doi: 10.1007/S00253-011-3213-7.

[11] C. B. Anucha, I. Altin, E. Bacaksiz, and V. N. Stathopoulos, "Titanium dioxide ($TiO_2$)-based photocatalyst materials activity enhancement for contaminants of emerging concern (CECs) degradation: In the light of modification strategies," *Chemical Engineering Journal Advances*, vol. 10, p. 100262, May 2022, doi: 10.1016/J.CEJA.2022.100262.

[12] J. Schneider *et al.*, "Understanding TiO2photocatalysis: Mechanisms and materials," Oct. 08, 2014, *American Chemical Society*. doi: 10.1021/cr5001892.

[13] K. Hashimoto, H. Irie, and A. Fujishima, "TiO 2 photocatalysis: A historical overview and future prospects," *Japanese Journal of Applied Physics, Part 1: Regular Papers and Short Notes and Review Papers*, vol. 44, no. 12, pp. 8269–8285, Dec. 2005, doi: 10.1143/JJAP.44.8269.

[14] H. N. C. Dharma *et al.*, "A Review of Titanium Dioxide (TiO2)-Based Photocatalyst for Oilfield-Produced Water Treatment," *Membranes (Basel).*, vol. 12, no. 3, p. 345, Mar. 2022, doi: 10.3390/MEMBRANES12030345.

[15] T. Klassen *et al.*, “Basic principles and application potentials of cold gas spraying,” *Materwiss. Werksttech.*, vol. 41, no. 7, pp. 575–584, Jul. 2010, doi: 10.1002/MAWE.201000645.
[16] N. T. Padmanabhan and H. John, “Titanium dioxide based self-cleaning smart surfaces: A short review,” *J. Environ. Chem. Eng.*, vol. 8, no. 5, p. 104211, Oct. 2020, doi: 10.1016/J.JECE.2020.104211.
[17] R. Z. Hamza, A. A. Gobouri, H. M. Al-Yasi, T. A. Al-Talhi, and S. M. El-Megharbel, “A New Sterilization Strategy Using TiO2 Nanotubes for Production of Free Radicals that Eliminate Viruses and Application of a Treatment Strategy to Combat Infections Caused by Emerging SARS-CoV-2 during the COVID-19 Pandemic,” *Coatings 2021, Vol. 11, Page 680*, vol. 11, no. 6, p. 680, Jun. 2021, doi: 10.3390/COATINGS11060680.
[18] T. Tatsuma *et al.*, “Inactivation and spike protein denaturation of novel coronavirus variants by CuxO/TiO2 nano-photocatalysts,” *Scientific Reports 2023 13:1*, vol. 13, no. 1, pp. 1–8, Mar. 2023, doi: 10.1038/s41598-023-30690-0.
[19] R. K. Gupta, P. Micochova, A. Chadha, T. Hesseloj, F. Fraternali, and J. J. Ramsden, “Rapid inactivation of SARS-CoV-2 by titanium dioxide surface coating,” *Wellcome Open Res.*, vol. 6, 2021, doi: 10.12688/WELLCOMEOPENRES.16577.2.
[20] M. Miyauchi, K. Sunada, and K. Hashimoto, “Antiviral effect of visible light-sensitive cuxo/tio2 photocatalyst,” *Catalysts*, vol. 10, no. 9, pp. 1–19, Sep. 2020, doi: 10.3390/CATAL10091093.
[21] S. Gurunathan *et al.*, “Antiviral potential of nanoparticles—can nanoparticles fight against coronaviruses?,” *Nanomaterials*, vol. 10, no. 9, pp. 1–29, Sep. 2020, doi: 10.3390/NANO10091645.
[22] J. Prakash, J. Cho, and Y. K. Mishra, “Photocatalytic TiO2 nanomaterials as potential antimicrobial and antiviral agents: Scope against blocking the SARS-COV-2 spread,” *Micro and Nano Engineering*, vol. 14, p. 100100, Apr. 2022, doi: 10.1016/J.MNE.2021.100100.
[23] S. Stawarz, N. Witek, W. Kucharczyk, M. Bakar, and M. Stawarz, “Thermo-protective properties of polymer composites with nano-titanium dioxide,” *International Journal of Mechanics and Materials in Design*, vol. 15, no. 3, pp. 585–599, Sep. 2019, doi: 10.1007/S10999-018-9432-7.
[24] “Difference Between Rutile & Anatase Grade Titanium Dioxide in Paints | Esaar International Pvt. Ltd.” Accessed: Aug. 20, 2025. [Online]. Available: https://www.esaar.com/2024/09/28/difference-between-rutile-anatase-grade-titanium-dioxide-in-paints/
[25] M. C. Chen, P. W. Koh, V. K. Ponnusamy, and S. L. Lee, “Titanium dioxide and other nanomaterials based antimicrobial additives in functional paints and coatings: Review,” *Prog. Org. Coat.*, vol. 163, p. 106660, Feb. 2022, doi: 10.1016/J.PORGCOAT.2021.106660.
[26] M. Schutte-Smith, E. Erasmus, R. Mogale, N. Marogoa, A. Jayiya, and H. G. Visser, “Using visible light to activate antiviral and antimicrobial properties of TiO2 nanoparticles in paints and coatings: focus on new developments for frequent-touch surfaces in hospitals,” May 01, 2023, *Springer*. doi: 10.1007/s11998-022-00733-8.
[27] F. Salvadores, M. Reli, O. M. Alfano, K. Kočí, and M. de los M. Ballari, “Efficiencies evaluation of photocatalytic paints under indoor and outdoor air conditions,” *Front. Chem.*, vol. 8, p. 551710, Oct. 2020, doi: 10.3389/FCHEM.2020.551710/BIBTEX.
[28] A. Basso, A. P. Battisti, R. de F. P. M. Moreira, and H. J. José, “Photocatalytic effect of addition of TiO2 to acrylic-based paint for passive toluene degradation,” *Environ. Technol.*, vol. 41, no. 12, pp. 1568–1579, May 2020, doi: 10.1080/09593330.2018.1542034.

[29] A. Rosset *et al.*, “Towards the development of safer by design TiO2-based photocatalytic paint: impacts and performances,” *Environ. Sci. Nano*, vol. 8, no. 3, pp. 758–772, Mar. 2021, doi: 10.1039/D0EN01232G.
[30] M. T. Islam *et al.*, “Development of photocatalytic paint based on TiO2 and photopolymer resin for the degradation of organic pollutants in water,” *Science of The Total Environment*, vol. 704, p. 135406, Feb. 2020, doi: 10.1016/J.SCITOTENV.2019.135406.
[31] A. J. Haider, Z. N. Jameel, and I. H. M. Al-Hussaini, “Review on: Titanium dioxide applications,” *Energy Procedia*, vol. 157, pp. 17–29, 2019, doi: 10.1016/j.egypro.2018.11.159.
[32] K. Li, C. Teng, S. Wang, and Q. Min, “Recent Advances in TiO2-Based Heterojunctions for Photocatalytic CO2 Reduction With Water Oxidation: A Review,” *Front. Chem.*, vol. 0, p. 88, Apr. 2021, doi: 10.3389/FCHEM.2021.637501.
[33] O. Cabrera-Rodríguez *et al.*, “Evaluation of the performance of TiO2 thin films doped with silver nanoparticles as a protective coating for metal prostheses,” *Surf. Coat. Technol.*, vol. 458, p. 129349, Apr. 2023, doi: 10.1016/J.SURFCOAT.2023.129349.
[34] A. D’Agostino *et al.*, “Antibacterial titanium dioxide coatings for CoCrMo orthopaedic implants,” *Appl. Surf. Sci.*, vol. 609, p. 155300, Jan. 2023, doi: 10.1016/J.APSUSC.2022.155300.
[35] V. Kumaravel *et al.*, “Antimicrobial TiO2 nanocomposite coatings for surfaces, dental and orthopaedic implants,” *Chemical Engineering Journal*, vol. 416, p. 129071, Jul. 2021, doi: 10.1016/J.CEJ.2021.129071.
[36] A. Agrelli *et al.*, “Peptides for Coating TiO2 Implants: An In Silico Approach,” *Int. J. Mol. Sci.*, vol. 23, no. 22, Nov. 2022, doi: 10.3390/ijms232214048.
[37] S. Challagulla, K. Tarafder, R. Ganesan, and S. Roy, “Structure sensitive photocatalytic reduction of nitroarenes over TiO2,” *Sci. Rep.*, vol. 7, no. 1, Dec. 2017, doi: 10.1038/s41598-017-08599-2.
[38] S. Wu, X. Luo, Y. Long, and B. Xu, “Exploring the Phase Transformation Mechanism of Titanium Dioxide by High Temperature in Situ Method,” in *IOP Conference Series: Material Science and Engineering*, IOP Publishing, 2019. doi: 10.1088/1757-899X/493/1/012010.
[39] L. Wei, C. Yu, Q. Zhang, H. Liu, and Y. Wang, “TiO2-based heterojunction photocatalysts for photocatalytic reduction of CO2 into solar fuels,” *J. Mater. Chem. A Mater.*, vol. 6, no. 45, pp. 22411–22436, Nov. 2018, doi: 10.1039/C8TA08879A.
[40] M. Ge *et al.*, “A review of one-dimensional TiO2 nanostructured materials for environmental and energy applications,” 2016, *Royal Society of Chemistry*. doi: 10.1039/c5ta09323f.
[41] D. R. Eddy *et al.*, “Heterophase Polymorph of TiO2 (Anatase, Rutile, Brookite, TiO2 (B)) for Efficient Photocatalyst: Fabrication and Activity,” *Nanomaterials*, vol. 13, no. 4, Feb. 2023, doi: 10.3390/NANO13040704.
[42] J. S. Barbosa *et al.*, “Ultrafast sonochemistry-based approach to coat TiO2 commercial particles for sunscreen formulation,” *Ultrason. Sonochem.*, vol. 48, pp. 340–348, Nov. 2018, doi: 10.1016/J.ULTSONCH.2018.06.015.
[43] “What is Difference Between Rutile and Anatase Grade Titanium Dioxide ($TiO_2$)? | Esaar International Pvt. Ltd.” Accessed: Aug. 20, 2025. [Online]. Available: https://www.esaar.com/2024/11/22/what-is-difference-between-rutile-and-anatase-grade-titanium-dioxide-tio%E2%82%82/

[44] C. Xu, G. P. Rangaiah, and X. S. Zhao, “Photocatalytic Degradation of Methylene Blue by Titanium Dioxide: Experimental and Modeling Study,” *Ind. Eng. Chem. Res.*, vol. 53, no. 38, pp. 14641–14649, Sep. 2014, doi: 10.1021/IE502367X.
[45] Y. Zhao *et al.*, “Classification and catalytic mechanisms of heterojunction photocatalysts and the application of titanium dioxide (TiO2)-based heterojunctions in environmental remediation,” *J. Environ. Chem. Eng.*, vol. 10, no. 3, p. 108077, Jun. 2022, doi: 10.1016/J.JECE.2022.108077.
[46] Ž. Kovačič, B. Likozar, and M. Huš, “Electronic properties of rutile and anatase TiO2 and their effect on CO2 adsorption: A comparison of first principle approaches,” *Fuel*, vol. 328, p. 125322, Nov. 2022, doi: 10.1016/J.FUEL.2022.125322.
[47] X. Liu and J. Fu, “Electronic and elastic properties of the tetragonal anatase TiO2 structure from first principle calculation,” *Optik (Stuttg).*, vol. 206, p. 164342, Mar. 2020, doi: 10.1016/J.IJLEO.2020.164342.
[48] A. Carroll *et al.*, “Effect of calcination temperature on the characteristics of TiO2 synthesized from ilmenite and its applications for photocatalysis,” *IOP Conf. Ser. Mater. Sci. Eng.*, vol. 478, no. 1, p. 012019, Feb. 2019, doi: 10.1088/1757-899X/478/1/012019.
[49] L. Jing *et al.*, “LnVO4 (Ln=La, Ce, Pr, Nd, etc.)-based photocatalysts: Synthesis, design, and applications,” Apr. 01, 2024, *Chinese Society of Metals*. doi: 10.1016/j.jmst.2023.07.064.
[50] B. Song *et al.*, “Powerful combination of g-C3N4 and LDHs for enhanced photocatalytic performance: A review of strategy, synthesis, and applications,” Oct. 01, 2019, *Elsevier B.V.* doi: 10.1016/j.cis.2019.101999.
[51] S. Rondinini, S. Ardizzone, G. Cappelletti, A. Minguzzi, and A. Vertova, “Sol-Gel Synthesis.”
[52] Z. Han *et al.*, “Biomimetic multifunctional surfaces inspired from animals,” Aug. 01, 2016, *Elsevier B.V.* doi: 10.1016/j.cis.2016.03.004.
[53] S. Moharana, B. B. Sahu, R. Nayak, and R. N. Mahaling, “Synthesis and properties of percolative metal oxide-polymer composites,” in *Renewable Polymers and Polymer-Metal Oxide Composites: Synthesis, Properties, and Applications*, Elsevier, 2022, pp. 253–282. doi: 10.1016/B978-0-323-85155-8.00001-7.
[54] B. Kaur and S. N. Bhattacharya, “7 Automotive dyes and pigments.”
[55] M. Lyu *et al.*, “Advances in modification of Bi2MoO6 and its photocatalysis: A review,” Apr. 30, 2024, *Elsevier Ltd*. doi: 10.1016/j.jallcom.2024.173759.
[56] Q. E. Zhao, W. Wen, Y. Xia, and J. M. Wu, “Titania nanowires growing from P25 nuclei: Facile synthesis and the improved photocatalytic activity,” *Journal of Physics and Chemistry of Solids*, vol. 124, pp. 192–198, Jan. 2019, doi: 10.1016/J.JPCS.2018.09.016.
[57] D. Padayachee, A. S. Mahomed, S. Singh, and H. B. Friedrich, “Effect of the TiO2 Anatase/Rutile Ratio and Interface for the Oxidative Activation of n-Octane,” *ACS Catal.*, vol. 10, no. 3, pp. 2211–2220, Feb. 2020, doi: 10.1021/acscatal.9b04004.
[58] I. S. Grover, R. C. Prajapat, S. Singh, and B. Pal, “Highly photoactive Au-TiO2 nanowires for improved photo-degradation of propiconazole fungicide under UV/sunlight irradiation,” *Solar Energy*, vol. 144, pp. 612–618, Mar. 2017, doi: 10.1016/J.SOLENER.2017.02.001.
[59] S. Impemba *et al.*, “Engineering the heterojunction between TiO2 and In2O3 for improving the solar-driven hydrogen production,” *Int. J. Hydrogen Energy*, vol. 63, pp. 896–904, Apr. 2024, doi: 10.1016/J.IJHYDENE.2024.03.162.
[60] X. Qin, L. Ji, and A. Zhu, “Construction of rutile/anatase Ohmic heterojunction of TiO2/Ti3C2 with robust built-in electric field for boosting photocatalytic organic pollutant and hydrogen

evolution," *Appl. Surf. Sci.*, vol. 652, p. 159338, Apr. 2024, doi: 10.1016/J.APSUSC.2024.159338.

[61] X. Zhu, F. Qin, L. He, Y. Jiao, and W. Feng, "Enhanced Photocatalytic Activity of Anatase/Rutile Heterojunctions by Lanthanum and Tin Co-Doping," *Int. J. Mol. Sci.*, vol. 23, no. 19, Oct. 2022, doi: 10.3390/ijms231911339.

[62] M. Mousavi and J. B. Ghasemi, "Novel visible-light-responsive Black-TiO2/CoTiO3 Z-scheme heterojunction photocatalyst with efficient photocatalytic performance for the degradation of different organic dyes and tetracycline," *J. Taiwan Inst. Chem. Eng.*, vol. 121, pp. 168–183, Apr. 2021, doi: 10.1016/J.JTICE.2021.04.009.

[63] S. P. Pitre, T. P. Yoon, and J. C. Scaiano, "Titanium dioxide visible light photocatalysis: surface association enables photocatalysis with visible light irradiation," *Chemical Communications*, vol. 53, no. 31, pp. 4335–4338, Apr. 2017, doi: 10.1039/C7CC01952A.

[64] C. Liao, Y. Li, and S. C. Tjong, "Visible-Light Active Titanium Dioxide Nanomaterials with Bactericidal Properties", doi: 10.3390/nano10010124.

[65] V. Etacheri, C. Di Valentin, J. Schneider, D. Bahnemann, and S. C. Pillai, "Visible-light activation of TiO2 photocatalysts: Advances in theory and experiments," Dec. 01, 2015, *Elsevier*. doi: 10.1016/j.jphotochemrev.2015.08.003.

[66] C. K. Prier, D. A. Rankic, and D. W. C. MacMillan, "Visible light photoredox catalysis with transition metal complexes: Applications in organic synthesis," *Chem. Rev.*, vol. 113, no. 7, pp. 5322–5363, Jul. 2013, doi: 10.1021/CR300503R.

[67] S. G. Kumar and L. G. Devi, "Review on Modified TiO2 Photocatalysis under UV/Visible Light: Selected Results and Related Mechanisms on Interfacial Charge Carrier Transfer Dynamics," *Journal of Physical Chemistry A*, vol. 115, no. 46, pp. 13211–13241, Nov. 2011, doi: 10.1021/JP204364A.

[68] F. L. Toma *et al.*, "Comparative study on the photocatalytic behaviour of titanium oxide thermal sprayed coatings from powders and suspensions," *Surf. Coat. Technol.*, vol. 203, no. 15, pp. 2150–2156, May 2009, doi: 10.1016/J.SURFCOAT.2008.10.022.

[69] K. Schmidt *et al.*, "Ti surface modification by cold spraying with TiO2 microparticles," *Surf. Coat. Technol.*, vol. 309, pp. 749–758, Jan. 2017, doi: 10.1016/J.SURFCOAT.2016.10.091.

[70] M. Petit, L. Michez, J.-M. Raimundo, T. Malinowski, and P. Dumas, "An introduction to photocatalysis through methylene blue photodegradation," *Eur. J. Phys.*, vol. 37, no. 6, 2016, doi: 10.1088/0143-0807/37/6/065808ï.

[71] H. Adamu, "Photocatalytic Remediation of Nitrate in Aqueous Environment by TiO2-based Photocatalysts-Influence of Organic Hole Scavenger on the Selectivity of Reaction Product(s)." [Online]. Available: https://www.researchgate.net/publication/354386282

[72] R. Ameta, M. S. Solanki, S. Benjamin, and S. C. Ameta, "Photocatalysis," *Advanced Oxidation Processes for Wastewater Treatment: Emerging Green Chemical Technology*, pp. 135–175, Jan. 2018, doi: 10.1016/B978-0-12-810499-6.00006-1.

[73] F. Mohamadpour and A. M. Amani, "Photocatalytic systems: reactions, mechanism, and applications," *RSC Adv.*, vol. 14, no. 29, p. 20609, Jul. 2024, doi: 10.1039/D4RA03259D.

[74] H. Wang *et al.*, "Semiconductor heterojunction photocatalysts: design, construction, and photocatalytic performances," *Chem. Soc. Rev.*, vol. 43, no. 15, pp. 5234–5244, Jul. 2014, doi: 10.1039/C4CS00126E.

[75] J. Ângelo, L. Andrade, L. M. Madeira, and A. Mendes, "An overview of photocatalysis phenomena applied to NOx abatement," *J. Environ. Manage.*, vol. 129, pp. 522–539, Nov. 2013, doi: 10.1016/j.jenvman.2013.08.006.

[76] "5.13B: Band Theory of Metals and Insulators - Chemistry LibreTexts." Accessed: Dec. 21, 2025. [Online]. Available: https://chem.libretexts.org/Courses/Northern_Michigan_University/CH_215%3A_Chemistry_of_the_Elements_Fall_2023/05%3A_Solids_and_Solid-State_Chemistry/5.13%3A_Bonding_in_Metals_and_Semicondoctors/5.13B%3A_Band_Theory_of_Metals_and_Insulators

[77] M. A. Hassaan, M. A. El-Nemr, M. R. Elkatory, S. Ragab, V. C. Niculescu, and A. El Nemr, "Principles of Photocatalysts and Their Different Applications: A Review," *Top. Curr. Chem. (Cham).*, vol. 381, no. 6, p. 31, Dec. 2023, doi: 10.1007/S41061-023-00444-7.

[78] J. M. Wu and T. W. Zhang, "Photodegradation of rhodamine B in water assisted by titania films prepared through a novel procedure," *J. Photochem. Photobiol. A Chem.*, vol. 162, no. 1, pp. 171–177, Feb. 2004, doi: 10.1016/S1010-6030(03)00345-9.

[79] K. Krumova and G. Cosa, "Chapter 1: Overview of Reactive Oxygen Species," in *Singlet Oxygen: Applications in Biosciences and Nanosciences*, S. Nonell and C. Flors, Eds., The Royal Society of Chemistry, 2016, ch. 1, pp. 1–21. doi: https://doi.org/10.1039/9781782622208-00001.

[80] M. A. Hayat, "Introduction to Autophagy: Cancer, Other Pathologies, Inflammation, Immunity, Infection, and Aging, Volume 7," in *Autophagy: Cancer, Other Pathologies, Inflammation, Immunity, Infection, and Aging*, vol. 7, Elsevier Inc., 2015, ch. 1, pp. 1–53. doi: 10.1016/B978-0-12-801043-3.00001-7.

[81] D. J. Lefer and R. Bolli, "Cardioprotection," in *Muscle: Fundamental Biology and Mechanisms of Disease*, vol. 1–2, Elsevier, 2012, ch. 28, pp. 369–388. doi: 10.1016/B978-0-12-381510-1.00028-4.

[82] J. Schneider *et al.*, "Understanding TiO2photocatalysis: Mechanisms and materials," *Chem. Rev.*, vol. 114, no. 19, pp. 9919–9986, Oct. 2014, doi: 10.1021/CR5001892.

[83] K. F. Patel, V. Tejnecký, T. Ohno, V. L. Bailey, R. L. Sleighter, and P. G. Hatcher, "Reactive oxygen species alter chemical composition and adsorptive fractionation of soil-derived organic matter," *Geoderma*, vol. 384, p. 114805, Feb. 2021, doi: 10.1016/J.GEODERMA.2020.114805.

[84] Z. Bi *et al.*, "The generation and transformation mechanisms of reactive oxygen species in the environment and their implications for pollution control processes: A review," *Environ. Res.*, vol. 260, p. 119592, Nov. 2024, doi: 10.1016/J.ENVRES.2024.119592.

[85] C. Andrés Juan, J. Manuel Pérez de la Lastra, F. J. Plou, E. Pérez-Lebeña, and S. Reinbothe, "Molecular Sciences The Chemistry of Reactive Oxygen Species (ROS) Revisited: Outlining Their Role in Biological Macromolecules (DNA, Lipids and Proteins) and Induced Pathologies," *Int. J. Mol. Sci*, vol. 22, p. 4642, 2021, doi: 10.3390/ijms.

[86] H. Bayir, "Reactive oxygen species," *Crit. Care Med.*, vol. 33, no. 12, 2005, doi: 10.1097/01.CCM.0000186787.64500.12.

[87] F. D. Utami *et al.*, "TiO2 Photocatalytic Degradation of Methylene Blue Using Simple Spray Method," *IOP Conf. Ser. Mater. Sci. Eng.*, vol. 599, no. 1, p. 012026, Aug. 2019, doi: 10.1088/1757-899X/599/1/012026.

[88] C. Hou, B. Hu, and J. Zhu, "Photocatalytic degradation of methylene blue over TiO2 pretreated with varying concentrations of NaOH," *Catalysts*, vol. 8, no. 12, Dec. 2018, doi: 10.3390/catal8120575.

[89] R. S. Dariani, A. Esmaeili, A. Mortezaali, and S. Dehghanpour, “Photocatalytic reaction and degradation of methylene blue on TiO2 nano-sized particles,” *Optik (Stuttg).*, vol. 127, no. 18, pp. 7143–7154, Sep. 2016, doi: 10.1016/J.IJLEO.2016.04.026.
[90] S. Alkaykh, A. Mbarek, and E. E. Ali-Shattle, “Photocatalytic degradation of methylene blue dye in aqueous solution by MnTiO3 nanoparticles under sunlight irradiation,” *Heliyon*, vol. 6, no. 4, p. e03663, Apr. 2020, doi: 10.1016/J.HELIYON.2020.E03663.
[91] O. Sisman, N. Poli, D. Zappa, and E. Comini, “Synthesis of nanoporous tio2 with the use of diluted hydrogen peroxide solution and its application in gas sensing,” *Coatings*, vol. 9, no. 10, Oct. 2019, doi: 10.3390/coatings9100681.
[92] J. M. Wu, “Low-temperature preparation of titania nanorods through direct oxidation of titanium with hydrogen peroxide,” *J. Cryst. Growth*, vol. 269, no. 2–4, pp. 347–355, Sep. 2004, doi: 10.1016/j.jcrysgro.2004.05.023.
[93] J.-M. Wu, S. Hayakawa, K. Tsuru, and A. Osaka, “Porous titania ®lms prepared from interactions of titanium with hydrogen peroxide solution,” *Scr. Mater.*, vol. 46, pp. 101–106, 2002, [Online]. Available: www.elsevier.com/locate/scriptamat
[94] T. Sun and M. Wang, “A comparative study on titania layers formed on Ti, Ti-6Al-4V and NiTi shape memory alloy through a low temperature oxidation process,” *Surf. Coat. Technol.*, vol. 205, no. 1, pp. 92–101, Sep. 2010, doi: 10.1016/J.SURFCOAT.2010.06.019.
[95] J. M. Wu and B. Qi, “Low-temperature growth of monolayer rutile TiO2 nanorod films,” *Journal of the American Ceramic Society*, vol. 90, no. 2, pp. 657–660, Feb. 2007, doi: 10.1111/j.1551-2916.2006.01453.x.
[96] Z. Yu, L. Zhang, and S. Watanabe, “Facile modification of TiO2 nanoparticles with H2O2 + NH4F for enhanced visible light photodegradation of rhodamine B and methylene blue,” *Mater. Today Commun.*, vol. 33, p. 104213, Dec. 2022, doi: 10.1016/J.MTCOMM.2022.104213.
[97] J.-M. Wu, S. Hayakawa, K. Tsuru, and A. Osaka, “Low-Temperature Preparation of Anatase and Rutile Layers on Titanium Substrates and Their Ability To Induce in Vitro Apatite Deposition,” *Journal of the American Ceramic Society*, vol. 87, no. 9, pp. 1635–1642, 2004.
[98] J. M. Wu, T. W. Zhang, Y. W. Zeng, S. Hayakawa, K. Tsuru, and A. Osaka, “Large-scale preparation of ordered titania nanorods with enhanced photocatalytic activity,” *Langmuir*, vol. 21, no. 15, pp. 6995–7002, May 2005, doi: 10.1021/la0500272.
[99] J. M. Wu, B. Huang, M. Wang, and A. Osaka, “Titania nanoflowers with high photocatalytic activity,” *Journal of the American Ceramic Society*, vol. 89, no. 8, pp. 2660–2663, Mar. 2006, doi: 10.1111/j.1551-2916.2006.01104.x.
[100] J. M. Wu and H. X. Xue, “Photocatalytic active titania nanowire arrays on Ti substrates,” *Journal of the American Ceramic Society*, vol. 92, no. 9, pp. 2139–2143, Sep. 2009, doi: 10.1111/j.1551-2916.2009.03153.x.
[101] A. Nazir, P. Huo, and A. T. Rasool, “Recent advances on graphitic carbon nitride-based S-scheme photocatalysts: Synthesis, environmental applications, and challenges,” *J. Organomet. Chem.*, vol. 1004, p. 122951, Jan. 2024, doi: 10.1016/J.JORGANCHEM.2023.122951.
[102] Q. Pan *et al.*, “A review on the recent development of bismuth-based catalysts for CO2 photoreduction,” *J. Mol. Struct.*, vol. 1294, p. 136404, Dec. 2023, doi: 10.1016/J.MOLSTRUC.2023.136404.
[103] Z. Hou, W. Yang, Y. Zhan, X. Zhang, and J. Zhang, “Effect of Calcination Temperature on the Microstructure, Composition and Properties of Agglomerated Nanometer CeO2-Y2O3-ZrO2

Powders for Plasma Spray–Physical Vapor Deposition (PS-PVD) and Coatings Thereof," *Nanomaterials*, vol. 14, no. 12, p. 995, Jun. 2024, doi: 10.3390/NANO14120995.

[104] A. Sienkiewicz, A. Wanag, E. Kusiak-Nejman, E. Ekiert, P. Rokicka-Konieczna, and A. W. Morawski, "Effect of calcination on the photocatalytic activity and stability of TiO2 photocatalysts modified with APTES," *J. Environ. Chem. Eng.*, vol. 9, no. 1, p. 104794, Feb. 2021, doi: 10.1016/J.JECE.2020.104794.

[105] M. G. Kim *et al.*, "Effects of Calcination Temperature on the Phase Composition, Photocatalytic Degradation, and Virucidal Activities of TiO2 Nanoparticles," *ACS Omega*, vol. 6, no. 16, pp. 10668–10678, Apr. 2021, doi: 10.1021/ACSOMEGA.1C00043.

[106] S. Phromma, T. Wutikhun, P. Kasamechonchung, T. Eksangsri, and C. Sapcharoenkun, "Effect of Calcination Temperature on Photocatalytic Activity of Synthesized TiO2 Nanoparticles via Wet Ball Milling Sol-Gel Method," *Applied Sciences 2020, Vol. 10, Page 993*, vol. 10, no. 3, p. 993, Feb. 2020, doi: 10.3390/APP10030993.

[107] J. Li *et al.*, "Dual coordination between loess and N-doped TiO2 for efficient removal and degradation of organics," *Inorg. Chem. Commun.*, vol. 155, p. 110992, Sep. 2023, doi: 10.1016/J.INOCHE.2023.110992.

[108] H. Wu, J. Ma, C. Zhang, and H. He, "Effect of TiO2 calcination temperature on the photocatalytic oxidation of gaseous NH3," *Journal of Environmental Sciences*, vol. 26, no. 3, pp. 673–682, Mar. 2014, doi: 10.1016/S1001-0742(13)60441-6.

[109] S. Yamazaki, D. Takaki, N. Nishiyama, and Y. Yamazaki, "Factors affecting photocatalytic activity of TiO2," *Current Developments in Photocatalysis and Photocatalytic Materials: New Horizons in Photocatalysis*, pp. 23–38, Jan. 2020, doi: 10.1016/B978-0-12-819000-5.00003-5.

[110] C. Xu, P. Ravi Anusuyadevi, C. Aymonier, R. Luque, and S. Marre, "Nanostructured materials for photocatalysis," *Chem. Soc. Rev.*, vol. 48, no. 14, pp. 3868–3902, Jul. 2019, doi: 10.1039/C9CS00102F.

[111] F. Qin *et al.*, "Effect of Ag Modification on the Structure and Photocatalytic Performance of TiO2/Muscovite Composites," *Molecules*, vol. 28, no. 7, p. 3187, Apr. 2023, doi: 10.3390/MOLECULES28073187/S1.

[112] K. Qi, C. Imparato, O. Almjasheva, A. Khataee, and W. Zheng, "TiO2-based photocatalysts from type-II to S-scheme heterojunction and their applications," *J. Colloid Interface Sci.*, vol. 675, pp. 150–191, Dec. 2024, doi: 10.1016/J.JCIS.2024.06.204.

[113] N. Khima *et al.*, "TiO 2 sol-gel thin films: effect of acidic and basic pH on physical characteristics," *J. Solgel Sci. Technol.*, no. 112, pp. 277–288, Jun. 2024, doi: 10.1007/s10971-024-06519-1.

[114] M. Yalcin, "The effect of pH on the physical and structural properties of TiO2 nanoparticles," *J. Cryst. Growth*, vol. 585, p. 126603, May 2022, doi: 10.1016/J.JCRYSGRO.2022.126603.

[115] M. Tsega and F. B. Dejene, "Influence of acidic pH on the formulation of TiO2 nanocrystalline powders with enhanced photoluminescence property," *Heliyon*, vol. 3, no. 2, p. e00246, Feb. 2017, doi: 10.1016/J.HELIYON.2017.E00246.

[116] R. Hazan, S. Sreekantan, and I. Mat, "Growth Behavior of TiO2 Nanotube Arrays in Different Electrolyte pH," 2018, doi: 10.30967/ijcrset.1.S1.2018.529-534.

[117] V. Etacheri, M. K. Seery, S. J. Hinder, and S. C. Pillai, "Oxygen rich titania: A dopant free, high temperature stable, and visible-light active anatase photocatalyst," *Adv. Funct. Mater.*, vol. 21, no. 19, pp. 3744–3752, Oct. 2011, doi: 10.1002/adfm.201100301.

[118] C. Kusumawardani and N. Yogyakarta, “THE CALCINATION EFFECT ON THE CRYSTALLINITY, NITROGEN CONTENT, AND PORE STRUCTURE OF NITROGEN-DOPED TITANIUM DIOXIDE,” 2022.
[119] G. J. Yang, C. J. Li, F. Han, W. Y. Li, and A. Ohmori, “Low temperature deposition and characterization of TiO 2 photocatalytic film through cold spray,” *Appl. Surf. Sci.*, vol. 254, no. 13, pp. 3979–3982, Apr. 2008, doi: 10.1016/j.apsusc.2007.12.016.
[120] A. Gibas, M. Winnicki, A. Baszczuk, and M. Jasiorski, “Influence of spraying parameters on microstructure of oxygen-rich TiO2 coatings deposited using suspension low-pressure cold spray,” *Surf. Coat. Technol.*, vol. 457, p. 129321, Mar. 2023, doi: 10.1016/J.SURFCOAT.2023.129321.
[121] N. I. Omar, S. Selvami, M. Kaisho, M. Yamada, T. Yasui, and M. Fukumoto, “Deposition of titanium dioxide coating by the cold-spray process on annealed stainless steel substrate,” *Coatings*, vol. 10, no. 10, pp. 1–13, Oct. 2020, doi: 10.3390/coatings10100991.
[122] M. A. Adaan-Nyiak and A. A. Tiamiyu, “Recent advances on bonding mechanism in cold spray process: A review of single-particle impact methods,” Jan. 14, 2023, *Springer Nature*. doi: 10.1557/s43578-022-00764-2.
[123] T. Van Steenkiste, “The role of particle temperature and velocity in cold spray coating formation,” *The Cold Spray Materials Deposition Process: Fundamentals and Applications*, pp. 127–147, 2007, doi: 10.1533/9781845693787.2.127.
[124] P. Vo *et al.*, “Cold-spray processing of titanium and titanium alloys,” *Titanium Powder Metallurgy: Science, Technology and Applications*, pp. 405–423, Jan. 2015, doi: 10.1016/B978-0-12-800054-0.00022-8.
[125] S. Yin *et al.*, “Cold spray additive manufacturing and repair: Fundamentals and applications,” *Addit. Manuf.*, vol. 21, pp. 628–650, Apr. 2018, doi: 10.1016/J.ADDMA.2018.04.017.
[126] A. Srikanth, G. Mohammed Thalib Basha, and B. Venkateshwarlu, “A Brief Review on Cold Spray Coating Process,” *Mater. Today Proc.*, vol. 22, pp. 1390–1397, Jan. 2020, doi: 10.1016/J.MATPR.2020.01.482.
[127] R. Zybała *et al.*, “Properties of Cold Sprayed Titanium and Titanium Alloy Coatings after Laser Surface Treatment,” *MDPI*, vol. 15, no. 24, Dec. 2022, doi: 10.3390/ma15249014.
[128] A. Vardelle *et al.*, “The 2016 Thermal Spray Roadmap,” *Journal of Thermal Spray Technology*, vol. 25, no. 8, pp. 1376–1440, Dec. 2016, doi: 10.1007/s11666-016-0473-x.
[129] M. Yamada, H. Isago, H. Nakano, and M. Fukumoto, “Cold spraying of TiO 2 photocatalyst coating with nitrogen process gas,” *Journal of Thermal Spray Technology*, vol. 19, no. 6, pp. 1218–1223, Dec. 2010, doi: 10.1007/s11666-010-9520-1.
[130] I. Herrmann-Geppert *et al.*, “Cold gas spraying – A promising technique for photoelectrodes: The example TiO2,” *Catal. Today*, vol. 260, pp. 140–147, Feb. 2016, doi: 10.1016/J.CATTOD.2015.06.007.
[131] J. O. Kliemann, H. Gutzmann, F. Gärtner, H. Hübner, C. Borchers, and T. Klassen, “Formation of cold-sprayed ceramic titanium dioxide layers on metal surfaces,” in *Journal of Thermal Spray Technology*, Jan. 2011, pp. 292–298. doi: 10.1007/s11666-010-9563-3.
[132] M. Gardon, A. Latorre, M. Torrell, S. Dosta, J. Fernández, and J. M. Guilemany, “Cold gas spray titanium coatings onto a biocompatible polymer,” *Mater. Lett.*, vol. 106, pp. 97–99, Apr. 2013, doi: 10.1016/J.MATLET.2013.04.115.

[133] T. S. Price, P. H. Shipway, and D. G. McCartney, “Effect of cold spray deposition of a titanium coating on fatigue behavior of a titanium alloy,” *Proceedings of the International Thermal Spray Conference*, vol. 15, no. 4, pp. 507–512, Dec. 2006, doi: 10.1361/105996306X147108.
[134] T. Hussain, D. G. McCartney, P. H. Shipway, and T. Marrocco, “Corrosion behavior of cold sprayed titanium coatings and free standing deposits,” *Journal of Thermal Spray Technology*, vol. 20, no. 1–2, pp. 260–274, Jul. 2010, doi: 10.1007/S11666-010-9540-X.
[135] W. Wong, E. Irissou, A. N. Ryabinin, J. G. Legoux, and S. Yue, “Influence of helium and nitrogen gases on the properties of cold gas dynamic sprayed pure titanium coatings,” *Journal of Thermal Spray Technology*, vol. 20, no. 1–2, pp. 213–226, Sep. 2010, doi: 10.1007/S11666-010-9568-Y.
[136] W. Li, C. Cao, and S. Yin, “Solid-state cold spraying of Ti and its alloys: A literature review,” *Prog. Mater. Sci.*, vol. 110, p. 100633, May 2020, doi: 10.1016/J.PMATSCI.2019.100633.
[137] “Cole-Parmer RH-400 Standard Heated Circulating Bath, Standard Housing, 7 L; 120 VAC from Cole-Parmer Canada.” Accessed: Jan. 28, 2025. [Online]. Available: https://www.coleparmer.ca/i/cole-parmer-rh-400-standard-heated-circulating-bath-standard-housing-7-l-120-vac/2087345
[138] S. Swapp, “Scanning Electron Microscopy (SEM).” Accessed: Feb. 05, 2023. [Online]. Available: https://serc.carleton.edu/research_education/geochemsheets/techniques/SEM.html
[139] R. Schmitt, “Scanning Electron Microscope,” *CIRP Encyclopedia of Production Engineering*, pp. 1085–1089, 2014, doi: 10.1007/978-3-642-20617-7_6595.
[140] “Scanning Electron Microscopy | Nanoscience Instruments.” Accessed: Jan. 22, 2025. [Online]. Available: https://www.nanoscience.com/techniques/scanning-electron-microscopy/
[141] “SEM Scanning Electron Microscopy - Scimed.” Accessed: Jan. 22, 2025. [Online]. Available: https://www.scimed.co.uk/education/sem-scanning-electron-microscopy/
[142] “SEM.” Accessed: Feb. 05, 2023. [Online]. Available: https://warwick.ac.uk/fac/sci/physics/current/postgraduate/regs/mpagswarwick/ex5/techniques/structural/sem3/
[143] R. F. Egerton, “Physical Principles of Electron Microscopy: An Introduction to TEM, SEM, and AEM,” Edmonton, Canada, 2005.
[144] A. Mohammed and A. Abdullah, “Scanning Electron Microscopy (SEM): A Review,” 2019. [Online]. Available: https://www.researchgate.net/publication/330168803
[145] M. Dunlap and Dr. J. E. Adaskaveg, “Introduction to the Scanning Electron Microscope,” *Facility for Advanced Instrumentation, U. C. Davis*, 1997.
[146] K. Dewitt, “X-Ray Powder Diffraction Method Development and Validation for the Identification of Counterfeit Pharmaceuticals.”
[147] A. Jesche, M. Fix, A. Kreyssig, W. R. Meier, and P. C. Canfield, “X-Ray diffraction on large single crystals using a powder diffractometer,” *Philosophical Magazine*, vol. 96, no. 20, pp. 2115–2124, Jul. 2016, doi: 10.1080/14786435.2016.1192725.
[148] A. Ali, Y. W. Chiang, and R. M. Santos, “X-ray Diffraction Techniques for Mineral Characterization: A Review for Engineers of the Fundamentals, Applications, and Research Directions,” *Minerals 2022, Vol. 12, Page 205*, vol. 12, no. 2, p. 205, Feb. 2022, doi: 10.3390/MIN12020205.

[149] C. F. Holder and R. E. Schaak, “Tutorial on Powder X-ray Diffraction for Characterizing Nanoscale Materials,” *ACS Nano*, vol. 13, no. 7, pp. 7359–7365, Jul. 2019, doi: 10.1021/ACSNANO.9B05157/ASSET/IMAGES/MEDIUM/NN-2019-051577_0009.GIF.
[150] H. A. Foner and N. Adan, “The Characterization of Papers by X-Ray Diffraction (XRD): Measurement of Cellulose Crystallinity and Determination of Mineral Composition,” *Journal of the Forensic Science Society*, vol. 23, no. 4, pp. 313–321, Oct. 1983, doi: 10.1016/S0015-7368(83)72269-3.
[151] P. B. Raja, K. R. Munusamy, V. Perumal, and M. N. M. Ibrahim, “Characterization of nanomaterial used in nanobioremediation,” *Nano-Bioremediation: Fundamentals and Applications*, pp. 57–83, Jan. 2022, doi: 10.1016/B978-0-12-823962-9.00037-4.
[152] “X-ray Diffractometer Attachment Series”.
[153] “Rigaku Ultima IV X-Ray Diffractometer – Instrument Center of FAS.” Accessed: Jan. 07, 2026. [Online]. Available: https://science.sjp.ac.lk/instrumentcenter/instruments/rigaku-ultima-iv-x-ray-diffractometer/
[154] “X-ray Powder Diffraction (XRD).” Accessed: Feb. 05, 2023. [Online]. Available: https://serc.carleton.edu/msu_nanotech/methods/XRD.html
[155] B. Dutrow and C. Clark, “X-ray Powder Diffraction (XRD),” Montana Nanotechnology Facility, Montana State University. Accessed: Feb. 06, 2023. [Online]. Available: https://serc.carleton.edu/msu_nanotech/methods/XRD.html
[156] H. Jung, S. Jeong, Y. Park, Y. Shin, and H. Jeong, “X-ray Diffraction Analysis of Damaged Layer During Polishing of Silicon Carbide,” *International Journal of Precision Engineering and Manufacturing 2022 24:1*, vol. 24, no. 1, pp. 25–32, Nov. 2022, doi: 10.1007/S12541-022-00711-5.
[157] “Ultima IV X-Ray Diffractometer,” *The Rigaku Journal*, vol. 24, no. 1, pp. 25–26, 2008.
[158] G. S. Bumbrah and R. M. Sharma, “Raman spectroscopy – Basic principle, instrumentation and selected applications for the characterization of drugs of abuse,” *Egypt. J. Forensic Sci.*, vol. 6, no. 3, pp. 209–215, Sep. 2016, doi: 10.1016/J.EJFS.2015.06.001.
[159] S. Nandi, “Raman Spectroscopy,” Sep. 2021. doi: 10.13140/RG.2.2.24191.33445.
[160] A. Orlando *et al.*, “A Comprehensive Review on Raman Spectroscopy Applications,” *Chemosensors 2021, Vol. 9, Page 262*, vol. 9, no. 9, p. 262, Sep. 2021, doi: 10.3390/CHEMOSENSORS9090262.
[161] A. Saletnik, B. Saletnik, and C. Puchalski, “Overview of Popular Techniques of Raman Spectroscopy and Their Potential in the Study of Plant Tissues,” *Molecules*, vol. 26, no. 6, p. 1537, Mar. 2021, doi: 10.3390/MOLECULES26061537.
[162] N. Gierlinger and M. Schwanninger, “The potential of Raman microscopy and Raman imaging in plant research,” *Spectroscopy*, vol. 21, no. 2, pp. 69–89, 2007, doi: 10.1155/2007/498206.
[163] C. Laboratory, “Raman Spectroscopy,” Feb. 2009.
[164] P. M. V. Raja and A. R. Barron, *Raman and Surface-Enhanced Raman Spectroscopy*. Houston, 2024.
[165] P. Rostron, S. Gaber, and D. Gaber, “Raman Spectroscopy, Review,” *International Journal of Engineering and Technical Research (IJETR)*, vol. 6, no. 1, Sep. 2016.
[166] “XploRA PLUS TM Getting There Easier! Chemical Analysis & Imaging for Daily Use.” [Online]. Available: www.horiba.com/
[167] “Microprocessor Controlled Light Curing System Instruction Manual.”
[168] J. González-Camejo, S. Aparicio, M. Pachés, L. Borrás, and A. Seco, “Comprehensive assessment of the microalgae-nitrifying bacteria competition in microalgae-based wastewater

treatment systems: Relevant factors, evaluation methods and control strategies," *Algal Res.*, vol. 61, p. 102563, Jan. 2022, doi: 10.1016/J.ALGAL.2021.102563.
[169] S. O. Diaz and A. Viplav, "OD, Absorbance & Transmittance: Key Concepts in Spectrophotometry," *Byonoy Basics*, Jul. 2024, Accessed: Jan. 23, 2025. [Online]. Available: https://byonoy.com/journal/understanding-od-absorbance-transmittance-spectrophotometry/
[170] "Agilent BioTek Synergy H1 Microplate Reader," May 2023. Accessed: Jul. 02, 2025. [Online]. Available: https://www.agilent.com/en/product/clinical-microplate-instrumentation/clinical-microplate-readers/clinical-multimode-microplate-readers/biotek-synergy-h1-multimode-reader-1623194
[171] "Agilent BioTek Synergy H1 Multi-Mode Microplate Reader Instruction Manual," Aug. 2022. [Online]. Available: www.agilent.com/lifesciences/biotek
[172] "24 Well Treated Tissue Culture Plates Technical Data Sheet." Accessed: Jun. 29, 2025. [Online]. Available: vwr.com
[173] R. A. Lane and G. Buckton, "The novel combination of dynamic vapour sorption gravimetric analysis and near infra-red spectroscopy as a hyphenated technique," *Int. J. Pharm.*, vol. 207, no. 1–2, pp. 49–56, Oct. 2000, doi: 10.1016/S0378-5173(00)00528-7.
[174] C. A. S. Hill, A. J. Norton, and G. Newman, "The water vapour sorption properties of Sitka spruce determined using a dynamic vapour sorption apparatus," *Wood Sci. Technol.*, vol. 44, no. 3, pp. 497–514, Aug. 2010, doi: 10.1007/S00226-010-0305-Y/FIGURES/13.
[175] M. Kymäläinen, L. Rautkari, and C. A. S. Hill, "Sorption behaviour of torrefied wood and charcoal determined by dynamic vapour sorption," *J. Mater. Sci.*, vol. 50, no. 23, pp. 7673–7680, Dec. 2015, doi: 10.1007/S10853-015-9332-2/FIGURES/5.
[176] M. Janz and B. F. Johannesson, "Measurement of the Moisture Storage Capacity Using Sorption Balance and Pressure Extractors," Feb. 2001. doi: 10.1106/VRU2-LNV1-ME9X-8KKX.
[177] C. L. Levoguer and D. R. Williams, "The Characterisation of Pharmaceutical Materials by Dynamic Vapour Sorption," Nov. 2024.
[178] J. G. Choi, D. D. Do, and H. D. Do, "Surface diffusion of adsorbed molecules in porous media: Monolayer, multilayer, and capillary condensation regimes," *Ind. Eng. Chem. Res.*, vol. 40, no. 19, pp. 4005–4031, Sep. 2001, doi: 10.1021/IE010195Z/ASSET/IMAGES/MEDIUM/IE010195ZE00072.GIF.
[179] S. Brunauer, P. H. Emmett, and E. Teller, "Adsorption of Gases in Multimolecular Layers," *J. Am. Chem. Soc.*, vol. 60, no. 2, pp. 309–319, Feb. 1938, doi: 10.1021/JA01269A023.
[180] "CP-Ti Grade 1 Titanium Alloy | AP&C." Accessed: Jan. 29, 2025. [Online]. Available: https://www.advancedpowders.com/powders/titanium-alloys/cp-ti-grade-1
[181] Z. Yang, J. Lu, W. Ye, C. Yu, and Y. Chang, "Preparation of Pt/TiO2 hollow nanofibers with highly visible light photocatalytic activity," *Appl. Surf. Sci.*, vol. 392, pp. 472–480, Jan. 2017, doi: 10.1016/J.APSUSC.2016.09.065.
[182] H. Ding, S. S. Dwaraknath, L. Garten, P. Ndione, D. Ginley, and K. A. Persson, "Computational Approach for Epitaxial Polymorph Stabilization through Substrate Selection," *ACS Appl. Mater. Interfaces*, vol. 8, no. 20, pp. 13086–13093, May 2016, doi: 10.1021/ACSAMI.6B01630.
[183] M. Khalfaoui, S. Knani, M. A. Hachicha, and A. Ben Lamine, "New theoretical expressions for the five adsorption type isotherms classified by BET based on statistical physics treatment," *J. Colloid Interface Sci.*, vol. 263, no. 2, pp. 350–356, Jul. 2003, doi: 10.1016/S0021-9797(03)00139-5.
[184] "2.3: BET Surface Area Analysis of Nanoparticles - Chemistry LibreTexts." Accessed: Dec. 23, 2025. [Online]. Available:

https://chem.libretexts.org/Bookshelves/Analytical_Chemistry/Physical_Methods_in_Chemistry_and_Nano_Science_(Barron)/02%3A_Physical_and_Thermal_Analysis/2.03%3A_BET_Surface_Area_Analysis_of_Nanoparticles
[185] "Adsorption Isotherm and its Types | Chemistry Learning." Accessed: Dec. 23, 2025. [Online]. Available: https://chemistrylearning.com/adsorption-isotherm/
[186] M. E. Lydon, J. P. Ritter, and J. K. Comeau, "Trace analysis of hydrogen peroxide contamination," *2015 26th Annual SEMI Advanced Semiconductor Manufacturing Conference, ASMC 2015*, pp. 228–231, Jul. 2015, doi: 10.1109/ASMC.2015.7164476.
[187] "Hydrogen Peroxide: Grades, Types & Purity Levels | Lab Alley." Accessed: Dec. 21, 2025. [Online]. Available: https://www.laballey.com/blogs/articles/hydrogen-peroxide-grades-types-purity-levels
[188] A. Naldoni *et al.*, "Photocatalysis with Reduced TiO2: From Black TiO2 to Cocatalyst-Free Hydrogen Production," *ACS Catal.*, vol. 9, no. 1, pp. 345–364, Jan. 2018, doi: 10.1021/ACSCATAL.8B04068.
[189] J. L. Gole, J. D. Stout, C. Burda, Y. Lou, and X. Chen, "Highly efficient formation of visible light tunable TiO2-xNx photocatalysts and their transformation at the nanoscale," *Journal of Physical Chemistry B*, vol. 108, no. 4, pp. 1230–1240, Jan. 2004, doi: 10.1021/JP030843N.
[190] S. A. Bakar and C. Ribeiro, "Nitrogen-doped titanium dioxide: An overview of material design and dimensionality effect over modern applications," *Journal of Photochemistry and Photobiology C: Photochemistry Reviews*, vol. 27, pp. 1–29, Jun. 2016, doi: 10.1016/J.JPHOTOCHEMREV.2016.05.001.
[191] L. L. Lai, W. Wen, and J. M. Wu, "Room-Temperature Hydrolysis of Potassium Titanyl Oxalate and Water-Assisted Crystallization for TiO2 with High Photocatalytic Activity," *ChemistrySelect*, vol. 2, no. 18, pp. 5025–5031, Jun. 2017, doi: 10.1002/slct.201700372.
[192] L. L. Lai and J. M. Wu, "A facile synthesis of hierarchical TiO2 for dye adsorption and photocatalysis," *RSC Adv.*, vol. 4, no. 68, pp. 36212–36217, 2014, doi: 10.1039/c4ra04790g.
[193] H. Ding, S. S. Dwaraknath, L. Garten, P. Ndione, D. Ginley, and K. A. Persson, "Computational Approach for Epitaxial Polymorph Stabilization through Substrate Selection," *ACS Appl. Mater. Interfaces*, vol. 8, no. 20, pp. 13086–13093, May 2016, doi: 10.1021/ACSAMI.6B01630.
[194] M. K. Horton *et al.*, "Accelerated data-driven materials science with the Materials Project," *Nat. Mater.*, 2025, doi: 10.1038/S41563-025-02272-0.
[195] K. A. Persson, B. Waldwick, P. Lazic, and G. Ceder, "Prediction of solid-aqueous equilibria: Scheme to combine first-principles calculations of solids with experimental aqueous states," *Phys. Rev. B Condens. Matter Mater. Phys.*, vol. 85, no. 23, Jun. 2012, doi: 10.1103/PHYSREVB.85.235438.
[196] M. De Jong, W. Chen, H. Geerlings, M. Asta, and K. A. Persson, "A database to enable discovery and design of piezoelectric materials," *Sci. Data*, vol. 2, Sep. 2015, doi: 10.1038/SDATA.2015.53.
[197] J. M. Munro, K. Latimer, M. K. Horton, S. Dwaraknath, and K. A. Persson, "An improved symmetry-based approach to reciprocal space path selection in band structure calculations," *NPJ Comput. Mater.*, vol. 6, no. 1, Dec. 2020, doi: 10.1038/S41524-020-00383-7.
[198] H. Zheng *et al.*, "Grain boundary properties of elemental metals," *Acta Mater.*, vol. 186, pp. 40–49, Mar. 2020, doi: 10.1016/J.ACTAMAT.2019.12.030.

[199] Y. Hinuma, G. Pizzi, Y. Kumagai, F. Oba, and I. Tanaka, "Band structure diagram paths based on crystallography," *Comput. Mater. Sci.*, vol. 128, pp. 140–184, Feb. 2017, doi: 10.1016/J.COMMATSCI.2016.10.015.
[200] I. Petousis *et al.*, "Data Descriptor: High-throughput screening of inorganic compounds for the discovery of novel dielectric and optical materials," *Sci. Data*, vol. 4, Jan. 2017, doi: 10.1038/SDATA.2016.134.
[201] A. Wang *et al.*, "A Framework for Quantifying Uncertainty in DFT Energy Corrections," May 2021, doi: 10.26434/CHEMRXIV.14593476.V1.
[202] M. De Jong *et al.*, "Charting the complete elastic properties of inorganic crystalline compounds," *Sci. Data*, vol. 2, Mar. 2015, doi: 10.1038/SDATA.2015.9.
[203] K. Latimer, S. Dwaraknath, K. Mathew, D. Winston, and K. A. Persson, "Evaluation of thermodynamic equations of state across chemistry and structure in the materials project," *NPJ Comput. Mater.*, vol. 4, no. 1, Dec. 2018, doi: 10.1038/S41524-018-0091-X.
[204] R. Tran *et al.*, "Data Descriptor: Surface energies of elemental crystals," *Sci. Data*, vol. 3, Sep. 2016, doi: 10.1038/SDATA.2016.80.
[205] R. Woods-Robinson, D. Broberg, A. Faghaninia, A. Jain, S. S. Dwaraknath, and K. A. Persson, "Assessing High-Throughput Descriptors for Prediction of Transparent Conductors," *Chemistry of Materials*, vol. 30, no. 22, pp. 8375–8389, Nov. 2018, doi: 10.1021/ACS.CHEMMATER.8B03529.
[206] A. Jain *et al.*, "Formation enthalpies by mixing GGA and GGA + U calculations," *Phys. Rev. B Condens. Matter Mater. Phys.*, vol. 84, no. 4, Jul. 2011, doi: 10.1103/PHYSREVB.84.045115.
[207] A. K. Singh *et al.*, "Electrochemical Stability of Metastable Materials," *Chemistry of Materials*, vol. 29, no. 23, pp. 10159–10167, Dec. 2017, doi: 10.1021/ACS.CHEMMATER.7B03980.
[208] M. Aykol, S. S. Dwaraknath, W. Sun, and K. A. Persson, "Thermodynamic limit for synthesis of metastable inorganic materials," *Sci. Adv.*, vol. 4, no. 4, Apr. 2018, doi: 10.1126/SCIADV.AAQ0148.
[209] A. Jain *et al.*, "Commentary: The materials project: A materials genome approach to accelerating materials innovation," *APL Mater.*, vol. 1, no. 1, 2013, doi: 10.1063/1.4812323.
[210] A. M. Patel, J. K. Nørskov, K. A. Persson, and J. H. Montoya, "Efficient Pourbaix diagrams of many-element compounds," *Physical Chemistry Chemical Physics*, vol. 21, no. 45, pp. 25323–25327, 2019, doi: 10.1039/C9CP04799A.
[211] "Materials Project: Rutile Titanium Dioxide." Accessed: Aug. 01, 2025. [Online]. Available: https://next-gen.materialsproject.org/materials/mp-2657?formula=Ti#how_to_cite
[212] L. Zoubritzky and F.-X. Coudert, "CrystalNets.jl: Identification of Crystal Topologies," *SciPost Chemistry*, vol. 1, no. 2, Jun. 2022, doi: 10.21468/SCIPOSTCHEM.1.2.005.
[213] M. K. Horton, J. H. Montoya, M. Liu, and K. A. Persson, "High-throughput prediction of the ground-state collinear magnetic order of inorganic materials using Density Functional Theory," *NPJ Comput. Mater.*, vol. 5, no. 1, Dec. 2019, doi: 10.1038/S41524-019-0199-7.
[214] J. Kim, D. Sari, Q. Chen, G. Ceder, and K. A. Persson, "Evaluating Material Design Principles for Calcium-Ion Mobility in Intercalation Cathodes," *Chemistry of Materials*, vol. 37, no. 1, pp. 507–519, Jan. 2025, doi: 10.1021/ACS.CHEMMATER.4C02927).
[215] A. Rutt, J.-X. Shen, M. Horton, J. Kim, J. Lin, and K. A. Persson, "Expanding the Material Search Space for Multivalent Cathodes," *ACS Appl. Mater. Interfaces*, vol. 14, no. 39, pp. 44367–44376, Oct. 2022, doi: 10.1021/ACSAMI.2C11733).

[216] J. Kim, D. Sari, Q. Chen, G. Ceder, and K. A. Persson, “Evaluating Material Design Principles for Calcium-Ion Mobility in Intercalation Cathodes,” *Chemistry of Materials*, vol. 37, no. 1, pp. 507–519, Jan. 2025, doi: 10.1021/ACS.CHEMMATER.4C02927.
[217] F. Ricci *et al.*, “Data descriptor: An ab initio electronic transport database for inorganic materials,” *Sci. Data*, vol. 4, Jul. 2017, doi: 10.1038/SDATA.2017.85.
[218] Q. J. Hong, S. V. Ushakov, A. van de Walle, and A. Navrotsky, “Melting temperature prediction using a graph neural network model: From ancient minerals to new materials,” *Proc. Natl. Acad. Sci. U. S. A.*, vol. 119, no. 36, Sep. 2022, doi: 10.1073/PNAS.2209630119.
[219] F. Wegner, “Inverse participation ratio in 2+? dimensions,” *Zeitschrift f□r Physik B Condensed Matter and Quanta*, vol. 36, no. 3, pp. 209–214, Sep. 1980, doi: 10.1007/BF01325284).
[220] L. Yu and A. Zunger, “Identification of Potential Photovoltaic Absorbers Based on First-Principles Spectroscopic Screening of Materials,” *Phys. Rev. Lett.*, vol. 108, no. 6, p. 068701, Feb. 2012, doi: 10.1103/PHYSREVLETT.108.068701).
[221] Y. Xiong *et al.*, “High-throughput identification of spin-photon interfaces in silicon,” *Sci. Adv.*, vol. 9, no. 40, Oct. 2023, doi: 10.1126/SCIADV.ADH8617).
[222] A. Rutt, J. X. Shen, M. Horton, J. Kim, J. Lin, and K. A. Persson, “Expanding the Material Search Space for Multivalent Cathodes,” *ACS Appl. Mater. Interfaces*, vol. 14, no. 39, pp. 44367–44376, Oct. 2022, doi: 10.1021/ACSAMI.2C11733.
[223] Á. Morales-García, R. Valero, and F. Illas, “An Empirical, yet Practical Way To Predict the Band Gap in Solids by Using Density Functional Band Structure Calculations,” *The Journal of Physical Chemistry C*, vol. 121, no. 34, pp. 18862–18866, Aug. 2017, doi: 10.1021/ACS.JPCC.7B07421).
[224] R. Woods-Robinson *et al.*, “Designing transparent conductors using forbidden optical transitions,” *Matter*, vol. 6, no. 9, pp. 3021–3039, Sep. 2023, doi: 10.1016/J.MATT.2023.06.043.
[225] D. H. Fabini, M. Koerner, and R. Seshadri, “Candidate Inorganic Photovoltaic Materials from Electronic Structure-Based Optical Absorption and Charge Transport Proxies,” *Chemistry of Materials*, vol. 31, no. 5, pp. 1561–1574, Mar. 2019, doi: 10.1021/ACS.CHEMMATER.8B04542).
[226] A. M. Ganose and A. Jain, “Robocrystallographer: Automated crystal structure text descriptions and analysis,” *MRS Commun.*, vol. 9, no. 3, pp. 874–881, Sep. 2019, doi: 10.1557/MRC.2019.94.
[227] H. Zheng *et al.*, “Grain boundary properties of elemental metals,” *Acta Mater.*, vol. 186, pp. 40–49, Mar. 2020, doi: 10.1016/J.ACTAMAT.2019.12.030.
[228] K. Latimer, S. Dwaraknath, K. Mathew, D. Winston, and K. A. Persson, “Evaluation of thermodynamic equations of state across chemistry and structure in the materials project,” *NPJ Comput. Mater.*, vol. 4, no. 1, Dec. 2018, doi: 10.1038/S41524-018-0091-X.
[229] “Materials Project: Anatase Titanium Dioxide.” Accessed: Aug. 01, 2025. [Online]. Available: https://next-gen.materialsproject.org/materials/mp-390?formula=Ti#how_to_cite
[230] M. De Jong, W. Chen, H. Geerlings, M. Asta, and K. A. Persson, “A database to enable discovery and design of piezoelectric materials,” *Sci. Data*, vol. 2, Sep. 2015, doi: 10.1038/SDATA.2015.53.
[231] M. De Jong *et al.*, “Charting the complete elastic properties of inorganic crystalline compounds,” *Sci. Data*, vol. 2, Mar. 2015, doi: 10.1038/SDATA.2015.9.
[232] L. Zoubritzky and F.-X. Coudert, “CrystalNets.jl: Identification of Crystal Topologies,” *SciPost Chemistry*, vol. 1, no. 2, Jun. 2022, doi: 10.21468/SCIPOSTCHEM.1.2.005.

[233] A. Jain *et al.*, "Formation enthalpies by mixing GGA and GGA + U calculations," *Phys. Rev. B Condens. Matter Mater. Phys.*, vol. 84, no. 4, Jul. 2011, doi: 10.1103/PHYSREVB.84.045115.
[234] M. K. Horton *et al.*, "Accelerated data-driven materials science with the Materials Project," *Nat. Mater.*, 2025, doi: 10.1038/S41563-025-02272-0.
[235] Y. Hinuma, G. Pizzi, Y. Kumagai, F. Oba, and I. Tanaka, "Band structure diagram paths based on crystallography," *Comput. Mater. Sci.*, vol. 128, pp. 140–184, Feb. 2017, doi: 10.1016/J.COMMATSCI.2016.10.015.
[236] A. K. Singh *et al.*, "Electrochemical Stability of Metastable Materials," *Chemistry of Materials*, vol. 29, no. 23, pp. 10159–10167, Dec. 2017, doi: 10.1021/ACS.CHEMMATER.7B03980.
[237] M. K. Horton, J. H. Montoya, M. Liu, and K. A. Persson, "High-throughput prediction of the ground-state collinear magnetic order of inorganic materials using Density Functional Theory," *NPJ Comput. Mater.*, vol. 5, no. 1, Dec. 2019, doi: 10.1038/S41524-019-0199-7.
[238] I. Petousis *et al.*, "Data Descriptor: High-throughput screening of inorganic compounds for the discovery of novel dielectric and optical materials," *Sci. Data*, vol. 4, Jan. 2017, doi: 10.1038/SDATA.2016.134.
[239] F. Ricci *et al.*, "Data descriptor: An ab initio electronic transport database for inorganic materials," *Sci. Data*, vol. 4, Jul. 2017, doi: 10.1038/SDATA.2017.85.
[240] J. M. Munro, K. Latimer, M. K. Horton, S. Dwaraknath, and K. A. Persson, "An improved symmetry-based approach to reciprocal space path selection in band structure calculations," *NPJ Comput. Mater.*, vol. 6, no. 1, Dec. 2020, doi: 10.1038/S41524-020-00383-7.
[241] K. A. Persson, B. Waldwick, P. Lazic, and G. Ceder, "Prediction of solid-aqueous equilibria: Scheme to combine first-principles calculations of solids with experimental aqueous states," *Phys. Rev. B Condens. Matter Mater. Phys.*, vol. 85, no. 23, Jun. 2012, doi: 10.1103/PHYSREVB.85.235438.
[242] R. Tran *et al.*, "Data Descriptor: Surface energies of elemental crystals," *Sci. Data*, vol. 3, Sep. 2016, doi: 10.1038/SDATA.2016.80.
[243] A. Wang *et al.*, "A Framework for Quantifying Uncertainty in DFT Energy Corrections," May 2021, doi: 10.26434/CHEMRXIV.14593476.V1.
[244] H. Ding, S. S. Dwaraknath, L. Garten, P. Ndione, D. Ginley, and K. A. Persson, "Computational Approach for Epitaxial Polymorph Stabilization through Substrate Selection," *ACS Appl. Mater. Interfaces*, vol. 8, no. 20, pp. 13086–13093, May 2016, doi: 10.1021/ACSAMI.6B01630.
[245] A. M. Patel, J. K. Nørskov, K. A. Persson, and J. H. Montoya, "Efficient Pourbaix diagrams of many-element compounds," *Physical Chemistry Chemical Physics*, vol. 21, no. 45, pp. 25323–25327, 2019, doi: 10.1039/C9CP04799A.
[246] M. Aykol, S. S. Dwaraknath, W. Sun, and K. A. Persson, "Thermodynamic limit for synthesis of metastable inorganic materials," *Sci. Adv.*, vol. 4, no. 4, Apr. 2018, doi: 10.1126/SCIADV.AAQ0148.
[247] I. E. Castelli *et al.*, "New light-harvesting materials using accurate and efficient bandgap calculations," *Adv. Energy Mater.*, vol. 5, no. 2, Jan. 2015, doi: 10.1002/AENM.201400915.
[248] Y. Xiong *et al.*, "High-throughput identification of spin-photon interfaces in silicon," *Sci. Adv.*, vol. 9, no. 40, Oct. 2023, doi: 10.1126/SCIADV.ADH8617).

[249] R. Woods-Robinson *et al.*, "Designing transparent conductors using forbidden optical transitions," *Matter*, vol. 6, no. 9, pp. 3021–3039, Sep. 2023, doi: 10.1016/J.MATT.2023.06.043.
[250] A. Jain *et al.*, "Commentary: The materials project: A materials genome approach to accelerating materials innovation," *APL Mater.*, vol. 1, no. 1, 2013, doi: 10.1063/1.4812323.
[251] A. Rutt, J.-X. Shen, M. Horton, J. Kim, J. Lin, and K. A. Persson, "Expanding the Material Search Space for Multivalent Cathodes," *ACS Appl. Mater. Interfaces*, vol. 14, no. 39, pp. 44367–44376, Oct. 2022, doi: 10.1021/ACSAMI.2C11733).
[252] Á. Morales-García, R. Valero, and F. Illas, "An Empirical, yet Practical Way To Predict the Band Gap in Solids by Using Density Functional Band Structure Calculations," *The Journal of Physical Chemistry C*, vol. 121, no. 34, pp. 18862–18866, Aug. 2017, doi: 10.1021/ACS.JPCC.7B07421).
[253] M. Kuisma, J. Ojanen, J. Enkovaara, and T. T. Rantala, "Kohn-Sham potential with discontinuity for band gap materials," *Phys. Rev. B Condens. Matter Mater. Phys.*, vol. 82, no. 11, Sep. 2010, doi: 10.1103/PHYSREVB.82.115106.
[254] J. Kim, D. Sari, Q. Chen, G. Ceder, and K. A. Persson, "Evaluating Material Design Principles for Calcium-Ion Mobility in Intercalation Cathodes," *Chemistry of Materials*, vol. 37, no. 1, pp. 507–519, Jan. 2025, doi: 10.1021/ACS.CHEMMATER.4C02927.
[255] Q. J. Hong, S. V. Ushakov, A. van de Walle, and A. Navrotsky, "Melting temperature prediction using a graph neural network model: From ancient minerals to new materials," *Proc. Natl. Acad. Sci. U. S. A.*, vol. 119, no. 36, Sep. 2022, doi: 10.1073/PNAS.2209630119.
[256] O. Gritsenko, R. Van Leeuwen, E. Van Lenthe, and E. J. Baerends, "Self-consistent approximation to the Kohn-Sham exchange potential," *Phys. Rev. A (Coll Park).*, vol. 51, no. 3, pp. 1944–1954, 1995, doi: 10.1103/PHYSREVA.51.1944.
[257] A. Rutt, J. X. Shen, M. Horton, J. Kim, J. Lin, and K. A. Persson, "Expanding the Material Search Space for Multivalent Cathodes," *ACS Appl. Mater. Interfaces*, vol. 14, no. 39, pp. 44367–44376, Oct. 2022, doi: 10.1021/ACSAMI.2C11733.
[258] L. Yu and A. Zunger, "Identification of Potential Photovoltaic Absorbers Based on First-Principles Spectroscopic Screening of Materials," *Phys. Rev. Lett.*, vol. 108, no. 6, p. 068701, Feb. 2012, doi: 10.1103/PHYSREVLETT.108.068701).
[259] J. Kim, D. Sari, Q. Chen, G. Ceder, and K. A. Persson, "Evaluating Material Design Principles for Calcium-Ion Mobility in Intercalation Cathodes," *Chemistry of Materials*, vol. 37, no. 1, pp. 507–519, Jan. 2025, doi: 10.1021/ACS.CHEMMATER.4C02927).
[260] E. Gerber, Y. Yao, T. A. Arias, and E. A. Kim, "Ab Initio Mismatched Interface Theory of Graphene on α-RuCl3: Doping and Magnetism," *Phys. Rev. Lett.*, vol. 124, no. 10, Mar. 2020, doi: 10.1103/PHYSREVLETT.124.106804.
[261] F. Wegner, "Inverse participation ratio in 2+? dimensions," *Zeitschrift f□r Physik B Condensed Matter and Quanta*, vol. 36, no. 3, pp. 209–214, Sep. 1980, doi: 10.1007/BF01325284).
[262] D. H. Fabini, M. Koerner, and R. Seshadri, "Candidate Inorganic Photovoltaic Materials from Electronic Structure-Based Optical Absorption and Charge Transport Proxies," *Chemistry of Materials*, vol. 31, no. 5, pp. 1561–1574, Mar. 2019, doi: 10.1021/ACS.CHEMMATER.8B04542).
[263] A. M. Ganose and A. Jain, "Robocrystallographer: Automated crystal structure text descriptions and analysis," *MRS Commun.*, vol. 9, no. 3, pp. 874–881, Sep. 2019, doi: 10.1557/MRC.2019.94.
[264] M. De Jong *et al.*, "Charting the complete elastic properties of inorganic crystalline compounds," *Sci. Data*, vol. 2, Mar. 2015, doi: 10.1038/SDATA.2015.9.

[265] H. Zheng *et al.*, "Grain boundary properties of elemental metals," *Acta Mater.*, vol. 186, pp. 40–49, Mar. 2020, doi: 10.1016/J.ACTAMAT.2019.12.030.
[266] A. Jain *et al.*, "Formation enthalpies by mixing GGA and GGA + U calculations," *Phys. Rev. B Condens. Matter Mater. Phys.*, vol. 84, no. 4, Jul. 2011, doi: 10.1103/PHYSREVB.84.045115.
[267] A. M. Patel, J. K. Nørskov, K. A. Persson, and J. H. Montoya, "Efficient Pourbaix diagrams of many-element compounds," *Physical Chemistry Chemical Physics*, vol. 21, no. 45, pp. 25323–25327, 2019, doi: 10.1039/C9CP04799A.
[268] K. A. Persson, B. Waldwick, P. Lazic, and G. Ceder, "Prediction of solid-aqueous equilibria: Scheme to combine first-principles calculations of solids with experimental aqueous states," *Phys. Rev. B Condens. Matter Mater. Phys.*, vol. 85, no. 23, Jun. 2012, doi: 10.1103/PHYSREVB.85.235438.
[269] M. Aykol, S. S. Dwaraknath, W. Sun, and K. A. Persson, "Thermodynamic limit for synthesis of metastable inorganic materials," *Sci. Adv.*, vol. 4, no. 4, Apr. 2018, doi: 10.1126/SCIADV.AAQ0148.
[270] A. K. Singh *et al.*, "Electrochemical Stability of Metastable Materials," *Chemistry of Materials*, vol. 29, no. 23, pp. 10159–10167, Dec. 2017, doi: 10.1021/ACS.CHEMMATER.7B03980.
[271] "Materials Project: Titanium." Accessed: Aug. 01, 2025. [Online]. Available: https://next-gen.materialsproject.org/materials/mp-46?formula=Ti
[272] R. Tran *et al.*, "Data Descriptor: Surface energies of elemental crystals," *Sci. Data*, vol. 3, Sep. 2016, doi: 10.1038/SDATA.2016.80.
[273] M. K. Horton, J. H. Montoya, M. Liu, and K. A. Persson, "High-throughput prediction of the ground-state collinear magnetic order of inorganic materials using Density Functional Theory," *NPJ Comput. Mater.*, vol. 5, no. 1, Dec. 2019, doi: 10.1038/S41524-019-0199-7.
[274] A. Wang *et al.*, "A Framework for Quantifying Uncertainty in DFT Energy Corrections," May 2021, doi: 10.26434/CHEMRXIV.14593476.V1.
[275] M. De Jong, W. Chen, H. Geerlings, M. Asta, and K. A. Persson, "A database to enable discovery and design of piezoelectric materials," *Sci. Data*, vol. 2, Sep. 2015, doi: 10.1038/SDATA.2015.53.
[276] K. Latimer, S. Dwaraknath, K. Mathew, D. Winston, and K. A. Persson, "Evaluation of thermodynamic equations of state across chemistry and structure in the materials project," *NPJ Comput. Mater.*, vol. 4, no. 1, Dec. 2018, doi: 10.1038/S41524-018-0091-X.
[277] I. Petousis *et al.*, "Data Descriptor: High-throughput screening of inorganic compounds for the discovery of novel dielectric and optical materials," *Sci. Data*, vol. 4, Jan. 2017, doi: 10.1038/SDATA.2016.134.
[278] A. Jain *et al.*, "Commentary: The materials project: A materials genome approach to accelerating materials innovation," *APL Mater.*, vol. 1, no. 1, 2013, doi: 10.1063/1.4812323.
[279] M. K. Horton *et al.*, "Accelerated data-driven materials science with the Materials Project," *Nat. Mater.*, 2025, doi: 10.1038/S41563-025-02272-0.
[280] J. M. Munro, K. Latimer, M. K. Horton, S. Dwaraknath, and K. A. Persson, "An improved symmetry-based approach to reciprocal space path selection in band structure calculations," *NPJ Comput. Mater.*, vol. 6, no. 1, Dec. 2020, doi: 10.1038/S41524-020-00383-7.
[281] F. Ricci *et al.*, "Data descriptor: An ab initio electronic transport database for inorganic materials," *Sci. Data*, vol. 4, Jul. 2017, doi: 10.1038/SDATA.2017.85.

[282] Q. J. Hong, S. V. Ushakov, A. van de Walle, and A. Navrotsky, “Melting temperature prediction using a graph neural network model: From ancient minerals to new materials,” *Proc. Natl. Acad. Sci. U. S. A.*, vol. 119, no. 36, Sep. 2022, doi: 10.1073/PNAS.2209630119.
[283] L. Zoubritzky and F.-X. Coudert, “CrystalNets.jl: Identification of Crystal Topologies,” *SciPost Chemistry*, vol. 1, no. 2, Jun. 2022, doi: 10.21468/SCIPOSTCHEM.1.2.005.
[284] A. M. Ganose and A. Jain, “Robocrystallographer: Automated crystal structure text descriptions and analysis,” *MRS Commun.*, vol. 9, no. 3, pp. 874–881, Sep. 2019, doi: 10.1557/MRC.2019.94.
[285] O. Frank, M. Zukalova, B. Laskova, J. Kürti, J. Koltai, and L. Kavan, “Raman spectra of titanium dioxide (anatase, rutile) with identified oxygen isotopes (16, 17, 18),” *Physical Chemistry Chemical Physics*, vol. 14, no. 42, pp. 14567–14572, Nov. 2012, doi: 10.1039/c2cp42763j.
[286] A. R. Zanatta, “A fast-reliable methodology to estimate the concentration of rutile or anatase phases of TiO,” *AIP Adv.*, vol. 7, 2017, doi: 10.1063/1.4992130.
[287] M. Sboui *et al.*, “TiO2/Ag2O immobilized on cellulose paper: A new floating system for enhanced photocatalytic and antibacterial activities,” *Environ. Res.*, vol. 198, p. 111257, Jul. 2021, doi: 10.1016/J.ENVRES.2021.111257.
[288] “4.4.2: Molecular Vibrations - Chemistry LibreTexts.” Accessed: Jul. 03, 2025. [Online]. Available: https://chem.libretexts.org/Bookshelves/Inorganic_Chemistry/Inorganic_Chemistry_(LibreTexts)/04%3A_Symmetry_and_Group_Theory/4.04%3A_Examples_and_Applications_of_Symmetry/4.4.02%3A_Molecular_Vibrations
[289] “4.3: Raman Spectroscopy - Chemistry LibreTexts.” Accessed: Jul. 03, 2025. [Online]. Available: https://chem.libretexts.org/Bookshelves/Analytical_Chemistry/Physical_Methods_in_Chemistry_and_Nano_Science_(Barron)/04%3A_Chemical_Speciation/4.03%3A_Raman_Spectroscopy
[290] V. Ćorluka, Ž. Hederić, and M. Hadžiselimović, “Moisture measurement in solid samples using Raman spectroscopy,” Jan. 2011.
[291] D. Tuschel, “Practical Group Theory and Raman Spectroscopy, Part I: Normal Vibrational Modes,” *Molecular Spectroscopy Workbench*, Edison, NJ, Feb. 2014.
[292] X. Chen and S. S. Mao, “Titanium dioxide nanomaterials: Synthesis, properties, modifications and applications,” Jul. 2007. doi: 10.1021/cr0500535.
[293] A. A. Okab, Z. H. Jabbar, B. H. Graimed, A. I. Alwared, S. H. Ammar, and M. A. Hussein, “A comprehensive review highlights the photocatalytic heterojunctions and their superiority in the photo-destruction of organic pollutants in industrial wastewater,” *Inorg. Chem. Commun.*, vol. 158, p. 111503, Dec. 2023, doi: 10.1016/J.INOCHE.2023.111503.
[294] W. Wen *et al.*, “Anatase TiO2 ultrathin nanobelts derived from room-temperature-synthesized titanates for fast and safe lithium storage,” *Sci. Rep.*, vol. 5, no. 1, Dec. 2015, doi: 10.1038/srep11804.